ADAPTIVE MESH REFINEMENT AND COARSENING FOR COMPOSITIONAL RESERVOIR SIMULATION

A Dissertation

by

KARIN GABRIELA GONZALEZ ABAD

Submitted to the Office of Graduate and Professional Studies of
Texas A&M University
in partial fulfillment of the requirements for the degree of

DOCTOR OF PHILOSOPHY

Chair of Committee,	Maria A. Barrufet
Committee Members,	Thomas A. Blasingame
	Eduardo Gildin
	Michael King
Head of Department,	Daniel Hill

December 2016

Major Subject: Petroleum Engineering

ABSTRACT

This dissertation introduces a new method to create adaptive mesh refinement and coarsening in compositional reservoir simulation. The methodology targets individual cells for refinement based on forecasted compositional fronts calculated using streamlines and the analytical convection-dispersion transport equation. Quadtree decomposition determines the optimal spatial discretization across the simulation grid using dynamic and static reservoir properties. Application of the new approach results in improved computational performance without compromising the accuracy of phase behavior.

Current dynamic gridding implementations have rigid schemes, posing two major limitations: cell refinement size is a pre-determined input value and compositional maps from the previous time step define the refinement region. This solution leads to suboptimal modeling due to time-lagging refinement and lack of grid adaptability in heterogeneous reservoirs and/or fast-moving compositional fronts. The new methodology overcomes these limitations by combining streamline and particle trajectory to forecast the injection front location and adapt grid sizes in advance.

Tracking compositional variations starts by calculating fluxes for all cells using the finite-difference solution. Next, Pollock's tracing method allows reducing the 3-dimensional model into a series of 1-dimensional streamlines, while the convection-dispersion equation forecasts future compositions, shape, and location of injection front along each streamline trajectory. Finally, quadtree decomposition analyzes the homogeneity of dynamic and/or static properties (e.g., composition, pressure, permeability, facies) to determine if a volume can be represented by a single gridblock or if it requires refinement to preserve spatial details. Grid discretization is dynamic over time, refining cells requiring high-resolution and/or coarsening those with low variation.

A mechanistic model with CO_2 injection served to evaluate the methodology. The fluid was modeled with five pseudo-components and the Peng-Robison equation of state with volume translation to improve volumetric predictions. The new approach reduced the total number of cells required to model miscible injection by continuously creating adaptive grids that represent the advancement and shape of the injection front. Results showed a reduction in computational cost between 30-63% over a static fine grid without compromising the representation of compositional mixing phenomena and production forecast.

ACKNOWLEDGMENTS

I would like to express my deepest appreciation to my committee chair, Professor Dr. Maria A. Barrufet, who have supported me throughout my graduate studies with her invaluable mentoring and immense enthusiasm. Without her guidance and persistent help, this work would not have been possible.

Thank you to the committee members, Dr. Michael King, Dr. Eduardo Gildin, and Dr. Blasingame, for their insightful and discerning comments on reservoir simulation techniques and for conveying high research standards.

In addition, my appreciations to the professors of the petroleum engineering department at Texas A&M University who have deepened my keen interest in research through classes, seminars, and discussions.

I wish to thank my family for their unconditional support and confidence throughout my studies. Most of all, my beloved husband Ernesto whose continuous support, encouragement, and advises made graduate school an extraordinary experience. Thank you.

Finally, I gratefully acknowledge BakerHughes for supporting this research under the Paula Erazo Gonzalez Fellowship.

NOMENCLATURE

A	Area perpendicular to flow direction
B_w	Water formation volume factor
c	Volume parameter
$\vec{c}_{B,k}$	Vector from the centroid of the cell B to the centroid of the kth face
C_i	Mass concentration of component i
C_{iI}	Initial molar concentration of component i
C_{iJ}	Injected molar concentration of component i
c_f	Rock compressibility
c_v	Water viscosibility
c_w	Water compressibility
$\widehat{f}_i$	Fugacity of component i in a mixture
f_v	Vapor molar fraction
g	Velocity gradient
h	Thickness
k	Permeability
K_i	Equilibrium ratio of component i (x_i^g/x_i^o)
K_ℓ	Longitudinal dispersion coefficient
k_r	Relative permeability
L	Length
M	Mobility
M_{w_i}	Molecular weight of component i
n	Grid refinement level (quadtree structure)
n	Number of moles
$\vec{n}_k$	Normal of the face
$\vec{N}$	Number of moles
N_c	Number of components

N_f	Number of connecting faces
N_i	Number moles of component i
N_p	Number of phases
N_{Pe}	Peclet number
p	Pressure
pc	Capillary pressure
p_{c_i}	Critical pressure of component i
p_{pc}	Pseudo critical pressure
p_r	Reduced pressure
p_{wf}	Bottomhole flowing pressure
q_ℓ	Molar rate ($\ell = o, g, w$)
Q	Volumetric flow rate
R	Universal gas constant
r_o	Equivalent Peaceman radius
r_w	Wellbore radius
S_ℓ	Saturation ($\ell = o, g, w$)
S	Well skin (in Peaceman well equation)
s_i	Dimensionless shift parameter of component i
t	Time
T	Temperature
T_{c_i}	Critical temperature of component i
T_G	Geometric transmissibility
T_{pc}	Pseudo critical temperature
T_r	Reduced temperature
u	Superficial velocity
v	Interstitial velocity
V_b	Bulk volume
V_{c_i}	Critical volume of component i

$\overline{V_i}$	Partial molar volume of component i
V_m	Molar volume
V_{oid}	Void
V_p	Pore volume
V_t	Total fluid volume
W_I	Well index
x	Position
x_i^ℓ	Phase molar fraction of component i
z_i	Overall molar fraction of component i
Z	Gas compressibility factor

Greek Symbols

ϵ	Convergence criteria
ζ	Viscosity parameter
κ_{ij}	Binary interaction coefficient between components i and j
μ	Viscosity
ρ_ℓ	Mass density ($\ell = o, g, w$)
$\rho_{m,\ell}$	Molar density ($\ell = o, g, w$)
ρ_{mr}	Reduced molar density
ϕ	Porosity
$\widehat{\varphi}_i$	Fugacity coefficient of component i in a mixture
Φ	Flow potential
ω_i	Acentric factor of component i

Subscripts and Superscripts

B	Block
B_{adj}	Adjacent block
g	Gas phase

h	Horizontal
i, j	Component
k	Iteration
ℓ	Phase
n	Time level
o	Oil phase
p	Particle
v	Vertical
w	Water phase
x	X-direction
y	Y-direction
z	Z-direction

Abbreviations

AMRC	Adaptive mesh mefinement and coarsening
CDE	Convective-dispersion equation
CFL	Courant–Friedrichs–Lewy
EOS	Equation of state
IMPES	Implicit-pressure and explicit-saturations
IMPESC	Implicit-pressure, explicit-saturations, and explicit-compositions
LGR	Local grid refinement
PR	Peng-Robinson
SRK	Soave-Redlich-Kwong
TPFA	Two-point flux approximation

TABLE OF CONTENTS

Page

Page

LIST OF TABLES

TABLE Page

LIST OF FIGURES

FIGURE Page

CHAPTER I
INTRODUCTION

Injection of gas or solvent in oil reservoirs is a technique that has been widely implemented to improve oil recovery (Fletcher 1953; Hall et al. 1957; Babson 1989; Jhaveri et al. 2014). Depending on the pressure, temperature, and composition of the reservoir and injected fluids, it is possible to increase recovery as a result of oil swelling, reduction of the interfacial tension between oil and gas phase, viscosity reduction due to miscibility, pressure maintenance, and/or oil displacement from the reservoir pores.

Forecasting and studying gas injection processes is usually performed through compositional reservoir simulation. The complex phase behavior created by continuous changes in fluid composition requires small spatial discretization of the reservoir model. Large grid cells may result in significant errors in the estimation of production performance and breakthrough times. Camy and Emanuel (1977) explained grid-size dependency in compositional models from two effects: numerical dispersion and non-linearity of phase equilibrium computations.

Numerical dispersion occurs as the conservation derivatives are replaced with finite-difference approximation. It results in truncation errors that lead to saturation and composition dispersion impacting forecasts of production rates and breakthrough times (Fanchi, 1983). On the other hand, the non-linearity of the flash equation may have a significant impact when normalizing compositions and pressures over several cells (Camy and Emanuel, 1977). As compositional simulators are derived assuming thermodynamic equilibrium in each grid element, regrouping cells and re-normalizing its composition may result in a different overall phase behavior response.

The use of small grid blocks reduces the impact of both numerical dispersion and non-linearity of the phase equilibrium. However, the high computational cost of solving the flash equilibrium in multi-component systems makes the use of fine grid cells impractical for reservoir field modeling.

Dynamic mesh refinement provides a solution for preserving spatial details while reducing the number of cells, thus lowering computational requirements. This technique modifies grid size based on dynamic reservoir properties, refining areas with high-compositional and velocity gradients. This is especially valuable when modeling gas injection processes where some regions exhibit drastic compositional changes (injection front) while others remain relatively constant (swept and unswept regions).

Several formulations have been proposed for using dynamic grids in reservoir simulation (Heinemann et al. 1983; Han et al. 1987; Khan et al. 1995; Hornung and Trangenstein 1997; Sammon 2003; Nilsson et al. 2005a; van Batenburg et al. 2011), but key challenges remain. Current models present rigid schemes with two main limitations: i) refinement region is estimated from previous timestep solutions; and ii) the splitting size of the cells is defined based on user-input values. This approach leads to suboptimal application due to time-lagging results and lack of refinement flexibility. In this research, an Adaptive Mesh Refinement/Coarsening (AMRC) model is proposed where these two key limitations are solved.

1.1 Objectives

The main objective of this research is to propose, develop, and test a reservoir simulation model capable of refining and coarsening the grid cells based on static and dynamic properties to improve computational performance. This is done by combining a finite difference simulator with streamlines and the convective-dispersive equation to track the gas injection front and forecast regions that need refinement. The selection of the grid-size for

the adaptive grid is performed using quadtree decomposition analysis that enables selection of cell sizes across the reservoir model as a function of any dynamic or static property, e.g. compositions, pressures, permeability, facies, etc.

To accomplish this goal, we need to develop and implement the following tasks:

- Develop a finite-difference compositional reservoir simulator capable of handling flux movement between a variable number of cell faces. This is necessary as the model needs to represent coarse cells connecting with multiple fine cells.
- Implement streamline calculation using Pollock's tracking algorithm based on the flux distribution calculated with the finite-difference model.
- Conduct analytical calculation of compositions along 1-dimensional streamlines using the convection-dispersion equation. Map and interpolate the solutions into a 3-dimensional grid.
- Program quadtree decomposition algorithm analyzing homogeneity of dynamic and static properties to determine grid-size across the model.
- Evaluate the performance of dynamic gridding compared to fixed fine-grids. Analyses consider forecast accuracy and computational time for multiple gas injection scenarios.

1.2 Description of the chapters

Chapter I defines the general problem of this research, including relevance, approach, and objectives to be accomplished.

Chapter II presents a literature review, starting with generalities of compositional reservoir modeling including mathematical formulations using finite-difference, fluid phase behavior, and analytical solutions. We then consider current dynamic grid refinement models

and quadtree grid structure and decomposition techniques to assess their applicability and limitations.

Chapter III shows the mathematical formulation of a 3D fully compositional reservoir simulator incorporating adaptive gridding. It describes the derivation of the finite-difference model with its governing and auxiliary equations developed using solved using a implicit-pressure, explicit-saturations and composition method (IMPESC). We also present the validation of the model compared to a commercial simulator.

Chapter IV presents the adaptive mesh refinement and coarsening (AMRC) algorithm developed for modeling gas injection processes. It describes the process and equations for forecasting the injection front, selecting the size of the griblocks, and transferring and updating the properties in the new adaptive grid.

Chapter V shows the typical and extreme applications of the reservoir simulator using dynamic gridding. It includes homogeneous and heterogeneous cases to analyze the computational performance and test the robustness and stability of the algorithm.

Finally, Chapter VI states the conclusions and recommendations for future research.

CHAPTER II
BACKGROUND RESEARCH

Numerical simulation is an important tool for predicting, understanding, and optimizing the performance of oilfield reservoirs. Mathematical models describe flow of oil, gas, and water through porous media providing a representation of complex physical processes. This chapter presents a literature review of modeling techniques for compositional reservoir simulators, including finite-difference formulations and analytical solutions. Different adaptive mesh refinement techniques are analyzed to identify their applicability for dynamic gridding.

2.1 Modeling compositional reservoirs

2.1.1 Finite-difference reservoir simulation

Fluid transport in porous media is governed by the conservation of mass, momentum, and energy. These constitutive equations estimate changes in pressure and saturation after perturbing the system (sources and sinks). For fluids with substantial mass transfer between phases, a set of components or pseudo-components describe the fluid behavior assuming thermodynamic equilibrium. Modeling these compositional reservoirs requires calculating the mass or molar balance for each component or pseudo-component in the system. Equilibrium relations obtained from equations of state (EOS) provide the mass interchange between phases and the fluid properties of each phase.

Along with the governing equations, auxiliary expressions (relative permeabilities, well productivity/injectivity, capillary pressure between oil and gas phase, and viscosity models) are used to reduce the number of unknown variables and define the reservoir simulation system. Depending on how equations are formulated, compositional reservoir simulation methods can be divided into two types: mass balance and volume balance. For

simplicity of this study, we assumed isothermal flow (constant temperature), no mass exchange between the water and the hydrocarbon phase, and no chemical reactions.

Mass balance type

The development of the mass balance formulation starts with a mass (or mole) conservation equation for every hydrocarbon component in the system. Combining the mass conservation with the flow equation (Darcy's Law) results in the hydraulic diffusivity for a single component i in a porous media (Eq. 2.1).

$$\nabla \cdot \left[kA \sum_{\ell=1}^{Np} \left(x_i \frac{k_r}{\mu} \cdot \nabla \Phi \right)_\ell \right] = V_b \frac{\partial}{\partial t} \left[\phi N_i \right] - q_i \tag{2.1}$$

where:

A	Area perpendicular to flow direction
k	Permeability tensor
k_r	Relative permeability of phase ℓ
N_i	Number of moles of component i per unit volume
N_p	Total number of phases
q_i	Net molar rate of component i from sources and sinks
t	Time
x_i	Molar composition of phase ℓ
V_b	Bulk volume
μ	Viscosity of phase ℓ
ϕ	Rock porosity
Φ	Potential for phase ℓ

The first approach for compositional modeling using a mass balance formulation was proposed by Fussell and Fussell (1979). The authors developed a model based on Redlich-Kwong EOS assuming constant flow coefficients (e.g. relative permeabilities, densities,

viscosities) over a time step (i.e. explicit flow coefficients), while treating all other variables as unknowns (pressure, liquid molar fraction for hydrocarbon, and phase composition). The solution was achieved iteratively using a multivariable Newton-Raphson method.

In 1980, Coats developed a fully-implicit, three-phase model using an EOS for calculating phase equilibrium and fluid properties. The implicit treatment of transmissibilities, which included rock and fluid properties as a function of pressure, removed time-step limitations associated with models using explicit transmissibilities. The implementation of a fully-implicit method allowed unconditionally stable solutions as all unknowns are solved at the same time. This admitted larger time steps, but it also required larger processing power and storage.

Nghiem et al. (1981) proposed a formulation of the pressure equation similar to a black-oil model, with a symmetric and diagonally dominant matrix. This system of equations allowed using iterative methods solved as implicit-pressure, explicit-saturations, and explicit-composition (IMPESC). Nghiem et al.'s formulation provided great computational performance over fully-implicit methods. However, the use of IMPESC solutions limited the size of time-steps by the Courant–Friedrichs–Lewy (CFL) condition (Coats, 2003b). As consequence, a maximum time step must be calculated as a necessary condition for convergence.

Several other authors have proposed variations of the mass balance formulation (Young and Stephenson 1983; Chien et al. 1985). Although the fundamental derivation remains the same, selection of independent variables and solution schemes can provide improved performance.

Volume balance type

The volume balance formulation is based on the principle that, for each gridblock, the pore space (V_p, function of pressure) must be filled entirely with the total fluid volume (V_t, function of pressure and composition). This conservation relation is expressed in Eq. 2.2, where N_i is the number of moles of component i per unit volume, N_c is the total number of components, p is the pressure, and t is the time.

$$\left(\frac{\partial V_t}{\partial p}\right)_{\vec{N}} \frac{\partial p}{\partial t} + \sum_{i=1}^{N_c} \left[\left(\frac{\partial V_t}{\partial N_i}\right)_p \left(\frac{\partial N_i}{\partial t}\right) \right] = \frac{dV_p}{dp} \frac{\partial p}{\partial t} \tag{2.2}$$

Combining Eq. 2.2 with the molar conservation equation allows linearizing the pressure solution for each gridblock into a single equation that accounts for dependencies of volume, pressure, and compositions through an equation of state. The use of auxiliary equations is used to derive the volume-balance formulation shown in Eq. 2.3.

$$V_b \sum_{i=1}^{N_c} \overline{V}_i \nabla \cdot \left[kA \sum_{\ell=1}^{Np} \left(\frac{\rho_m x_i k_r}{\mu} \cdot \nabla \Phi \right)_\ell \right] + V_b \sum_{i=1}^{N_c} \overline{V}_i q_i = \left(\frac{\partial V_p}{\partial p} - \frac{\partial V_t}{\partial p} \right)_{\vec{N}} \frac{\partial p}{\partial t} \tag{2.3}$$

where:

A	Area perpendicular to flow direction
k	Permeability tensor
k_r	Relative permeability of phase ℓ
N_c	Number of components
N_p	Total number of phases
p	Pressure
q_i	Net molar rate of component i from sources and sinks
t	Time
V	Volume (Pore -p or Bulk -b)
$\overline{V}_i$	Partial molar volume
$x_{i,\ell}$	Molar composition of component i in phase ℓ

μ Viscosity of phase ℓ

Φ Potential for phase ℓ

ρ_m Molar density of phase ℓ

Acs et al. (1985) introduced the first volume balance formulation for compositional simulation. The authors developed a direct sequential method solved with implicit-pressure, explicit-saturation and composition (IMPESC). Individual phase composition is determined from a phase equilibrium analysis using an equation of state. Decoupling the phase behavior from the flow equation allowed maintaining flexible fluid calculations while solving the pressure equation directly with great computational advantages.

Watts (1986) used Acs et al. solution scheme and solved the pressure implicitly while solving the saturation using Spillette et al. (1973) semi-implicit approach. This resulted in a more stable sequential approach.

IMPESC systems are potentially unstable and computations require small time steps for reaching convergence. This is limited by the Courant–Friedrichs–Lewy (CFL) condition arising from the explicit integration of the numerical solution. If the condition is not met, then it will result in incorrect solutions. The CFL constraint in compositional reservoir simulation is discussed by Coats 2003b and shown in Eq. 2.4. Chapter III discusses further the calculation and limitations of the CFL number for compositional reservoir simulators.

$$CFL = \max\left[\frac{F\Delta t}{V_p}\right] \tag{2.4}$$

where:

F Function of rate and reservoir properties

Δt Time-step

V_p Pore volume

Mass balance and volume balance formulations are equivalent in their results. Wong et al. (1990) demonstrated that even though the two models were develop from fundamentally different points-of-view, both formulations lead to the same system of equations constrained by the governing equations of mass and volume balance.

2.1.2 Fluid phase behavior

The number of phases coexisting in equilibrium is determined by a stability analysis. For a multi-component system with two-phases (oil/gas), equilibrium is reached when the fugacity of each component ($\widehat{f}_i$) is equal in the liquid and vapor phase (Eq. 2.5). This relation neglects the effect of capillary pressure in equilibrium, only valid for bulk fluids (conventional reservoirs).

$$\widehat{f}_i^{\,o} = \widehat{f}_i^{\,g} \tag{2.5}$$

An EOS is used to calculate the fugacity of each component in the mixture. This functional relation between state functions accurately represents the dynamics of phase behavior caused by perturbing thermodynamic properties, including pressure, volume, temperature, or composition. In the oil and gas industry, it is more common to use cubic EOS to predict fluid behavior of petroleum mixtures. These equations were derived from the theoretical basis of van der Waals (1873), who accounted for non-zero molecular volume at infinite pressure (b) and attraction and repulsion forces between molecules (a).

More recent modifications resulted in equations with better quantitative predictions. In 1972, Soave proposed a modification of Redlich and Kwong (1949)'s EOS. The authors suggested replacing the temperature dependent term a for a more general form to calculate the pressure of a system. The new expression is known as Soave-Redlich-Kwong (SRK) EOS and is shown in Eq. 2.6.

$$p = \frac{RT}{V_m - b} - \frac{a}{V_m(V_m + b)} \tag{2.6}$$

where:

p	Pressure
R	Gas constant
T	Temperature
V_m	Molar volume

In 1976, Peng and Robinson modified the attraction pressure term from the van der Waals equation to improve the prediction of liquid densities and equilibrium ratios. Eq. 2.7 shows Peng-Robinson (PR) EOS.

$$p = \frac{RT}{V_m - b} - \frac{a}{V_m(V_m + b) + b(V_m - b)} \tag{2.7}$$

Soave-Redlich-Kwong and Peng-Robinson equation of states are the most widely implemented fluid models for compositional reservoir simulation as they accurately predict vapor/liquid phase equilibrium. Firoozabadi (1988) examined the difference between the two equations and concluded that both equations predict saturation pressures with small errors, although the Peng-Robinson EOS performed better by a small margin.

Firoozabadi (1988) also reported that both SRK and PR performed weak in predicting densities of simple hydrocarbon and reservoir-fluid systems. The SRK EOS generally underpreditcts liquid densities while PR EOS both overpredicts and underpreditcs liquid densities. Firoozabadi highlighted the need of introducing an additional parameter from the translation concept developed by Peneloux et al. (1982). The volume correction is applied directly to the calculated molar volume as shown in Eq. 2.8.

$$V_m = V_m^{EOS} - c \tag{2.8}$$

where:

V_m	Measured molar volume
V_m^{EOS}	Calculated molar volume
c	Volume parameter

The volume parameter c is calculated by matching experimental measurements with volumetric predictions using an EOS. This correction is a permissible transformation that provides improved densities and molar volumes without violating material balance and/or altering the phase equilibria calculation.

2.1.3 Analytical compositional models

The convection–dispersion equation (CDE) describes the mass transfer accounting for two physical processes: diffusion and convection (advection). This is the most-commonly used model for predicting solute movement in hydrodynamic systems.

In a porous media, CDE yields the conservation of a displacing component as it is injected into a system. Eq. 2.9 shows the CDE for an isothermal transport along a one-dimensional reservoir; this equation assumes incompressible rock and fluid, ideal mixing, and single phase fully miscible. Several authors have studied applications of the CDE for modeling reservoir performance (Laumbach 1975; Fanchi 1983; Lantz 1971; Fleming and Mansoori 1987), showing a good approximation for miscible displacement in oil reservoirs.

$$\phi\frac{\partial C_i}{\partial t} + u\frac{\partial C_i}{\partial x} - \phi K_\ell \frac{\partial^2 C_i}{\partial x^2} = 0 \tag{2.9}$$

where:

C_i	Concentration of component i (M/L^3)
K_ℓ	Longitudinal dispersion coefficient
t	Time

x Position

ϕ Porosity

u Superficial velocity

Multiple analytical solutions have been developed for solving the CDE using different initial and boundary conditions (van Genuchten and Alves, 1982), allowing accurate predictions with minimum computational cost.

2.2 Streamlines in reservoir models

Streamlines are instantaneous lines that are everywhere tangential to a velocity field (Datta-Gupta and King, 2007). The use of velocity maps, that can be calculated using finite-difference, allows tracking the streamlines in a reservoir model accounting for the compressibility and heterogeneities of the system (**Fig. 2.1**).

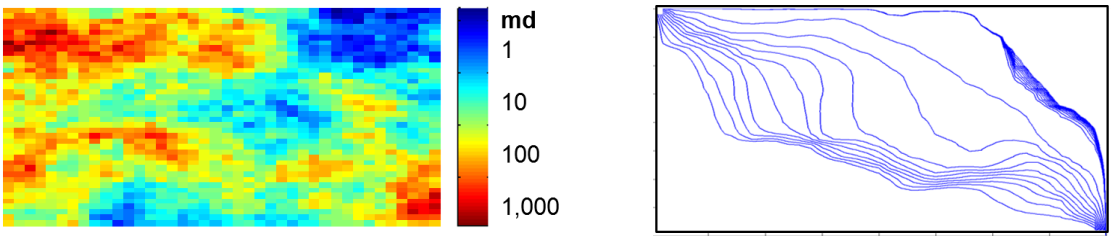

(a) Horizontal permeability distribution (b) the corresponding streamlines

Fig. 2.1—Heterogeneous reservoir with high contrasts in permeability showing flow paths (streamlines) along regions with high permeability.

The main method for tracing streamlines in 3D was proposed by Pollock in 1988. He developed a simple analytical model based on the time-of-flight concept. Using the flux distribution, the algorithm determines the exit point of a streamline and the time to exit assuming a linear approximation of the velocity field along each direction. Pollock's algorithm assumes cartesian cells; for nonorthogonal corner-point cells is it required to perform

an isoparametric transformation (Prevost et al., 2001).

Streamlines can be used for visualizing and understanding flow patterns in the reservoir. Solving the transport equation along streamlines (using numerical or analytical models) allows estimating fluid movement while providing great computational efficiency, both in memory and speed.

2.3 Adaptive mesh refinement and coarsening (AMRC)

The use of mesh refinement has been widely used in reservoir simulation to improve physical description without compromising computational performance. Refinement is done in regions with high pressure and saturation gradients, such as wells, faults, highly heterogeneous areas, and injection fronts. Mesh refinement have been improved by using adaptive or dynamic grids. This allows continuously modifying the grid spatial discretization on time to capture dynamic movements, which keeps large cells in regions without much variation and refining only those exhibiting significant changes.

2.3.1 Adaptive refinement methods

Refinement methods can be grouped into two types depending on the solution approach: nested grids and local grid refinement. Both can be extended to dynamic grid applications.

Nested grids

The first application of nested grids in fluid dynamics was proposed by Brandt in 1977 who developed a two-grid system for solving boundary-value problems. The technique uses iterative calculations between a fine and a coarse grid. First the coarse grid is used to obtain a preliminary solution, then results are interpolated and transferred to the fine grid, and finally the iteration continues in the fine grid. The process is repeated until desired

conversion is achieved.

Based on Brandt's formulation, Biterge and Ertekin (1992) proposed a black-oil model with static/dynamic gridding. The three-grid system was solved sequentially, finding a preliminary solution in the first-level grid, then transferring the boundary conditions to a finer grid, and solving the fine grid only within the boundaries of the refined model (**Fig. 2.2**). Grid was refined dynamically based on user-defined saturation thresholds.

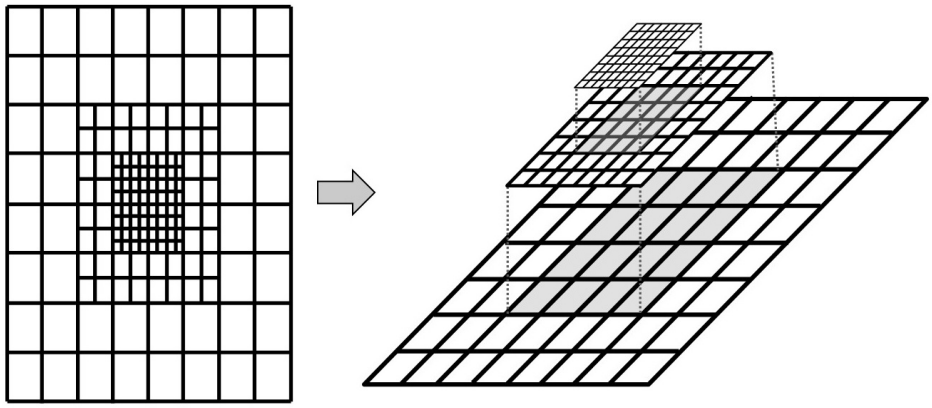

Fig. 2.2—Nested grids showing three-level refinement with selected areas raised above the coarse mesh to illustrate the overlapping regions.

Khan et al. (1995) developed an adaptive mesh refinement for a compositional simulator using 7-components micellar/polymer flood. The authors used hierarchical overlying meshes and refined dynamically based on user-specified ratio. The method was based on higher-order Godunov scheme previously implemented in reservoir simulators by Edwards and Christie (1993) and Edwards (1996).

In 2011, van Batenburg et al. developed a semi-implicit compositional simulator with an adaptive grid method that dynamically determines grid modifications. The solution is obtained first with Newton-Raphson method on a fixed grid, after which the grid is adapted.

To solve the flow equations on the updated grid, the Newton-Raphson process is continued with start values taken from interpolated or amalgamated values from the previous grid. They evaluated the model for simple 1D water-oil displacement, 1D polymer flooding, 2D in-Situ Combustion, and 3D inmiscible Water Alternating Gas (WAG) injection. The methodology proposed included a trial-and-error process to determine the property to be tracked and the threshold value that will trigger the refinement. The model allowed for de-refinement in regions with low variations of compositions to reduce the number of cells at a given time. Suicmez et al. (2011) later used van Batenburg et al.'s method for multiple contact miscible gas injection using prior time solution for selecting the refinement region. Results showed significant improvement in computational performance for miscible injection modeling.

Local grid refinements

In 1982, von Rosenberg developed a fixed local grid refinements (LGR) by dividing an original cell into four smaller elements. The coefficient matrix resulting from LGR included both fine and coarse cells simultaneously. This led to non-banded system of equations and more complex matrices compared to conventional structured grids (spared band matrix). **Fig 2.3** shows a 2D local grid refinement system with three size levels of cells.

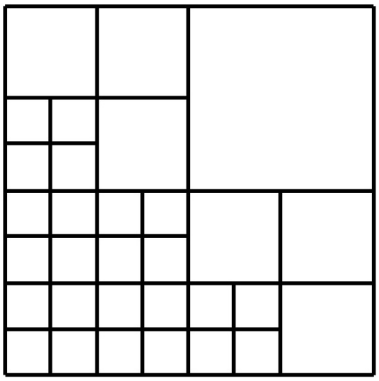

Fig. 2.3—Local Grid Refinement multi-grid system combining multiple sizes of grid cells. The system of equations is a non-banded matrix

Using von Rosenberg's technique, Heinemann et al. (1983) implemented a dynamic-LGR in a multiple application reservoir simulator solved using implicit-pressure and explicit-saturations (IMPES). Dynamic gridding resulted in new cell descriptions on time that required new systems of equations and dynamic re-numbering of cells. Grid subdivision was fixed for every cell, splitting as 2x2 or 4x4 sub-blocks. Although the method imposed severe restriction in cell subdivision and numerous inactive cells, the authors concluded that the dynamic grid refinement enabled more accurate description of the pressure and saturation relationships changing in the time and space.

Further studies on LGR were performed by Quandalle (1983) and Quandalle and Besset (1985) who presented two new schemes, a nine points scheme and a simplified five point scheme for calculating flow at composite boundaries.

Han et al. (1987) developed three-level dynamic grid refinement solved using IMPES. This method allowed a step-by-step processing of local subdivision with a three-level successive gridding. Water saturation thresholds (specified by the user) defined the dynamic conditions triggering refinement. Han et al. re-numbered cells using natural-like order resulting in regular coefficient matrices that provided simpler solution approaches.

Sammon (2003) developed one of the first applications of LGR for compositional simulation. The model uses rectangular amalgamation and proposes refinement and de-refinement to avoid keeping refined grids beyond the high-gradient regions occurred. It uses conditional directives to define refinement regions which rely on property variation across their region. The work was expanded later by Christensen et al. (2004) for the thermal modeling and evaluated for multiple case studies.

2.3.2 Quadtree structure and data decomposition

Hierarchical data structures are effective ways to represent spatial data or properties. This techniques organizes the information into tree-like structures characterized by a root value and subtrees of children. One of the most common tree structures is quadtrees, which can be used as representation of local grid refinements.

Quadtrees are based on the principle of recursive subdivision of a region into equal-size quadrants (Samet, 1989). Each node in a quadtree can be decomposed into exactly four children; this is shown in **Fig. 2.4** for a 2D representation with $2^3 \times 2^3$ dimensions, where 3 is the maximum hierarchical level. Octrees are the three-dimensional analog of the quadtree, decomposing exactly into eight children. **Fig. 2.5** shows a 3D octree representation with $2^2 \times 2^2 \times 2^2$ dimensions, where 2 is the maximum hierarchical level. For the purpose of this dissertation, we will refer as quadtrees for both 2D and 3D applications.

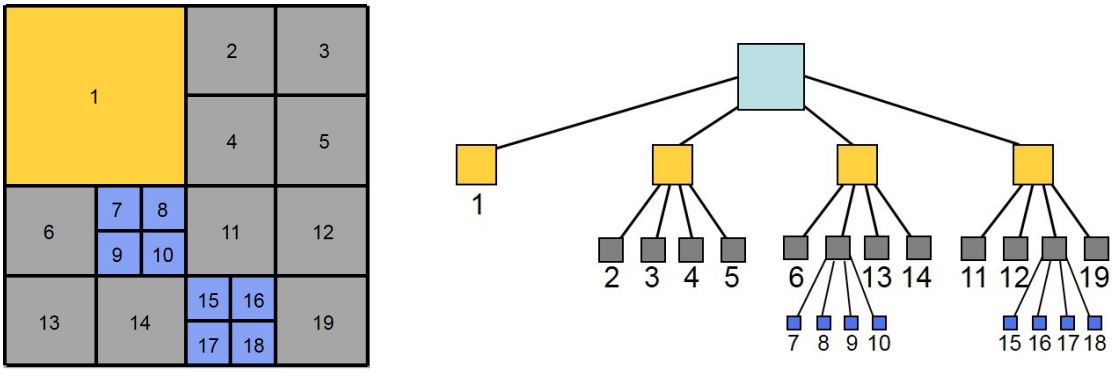

(a) 2D spatial representation in block-type system

(b) the corresponding quadtree representation

Fig. 2.4—Quadtree grid structure showing subdivision of cell A into three hierarchical levels. Nodes can be recursively decomposed into exactly four children as show in the quadtree representation.

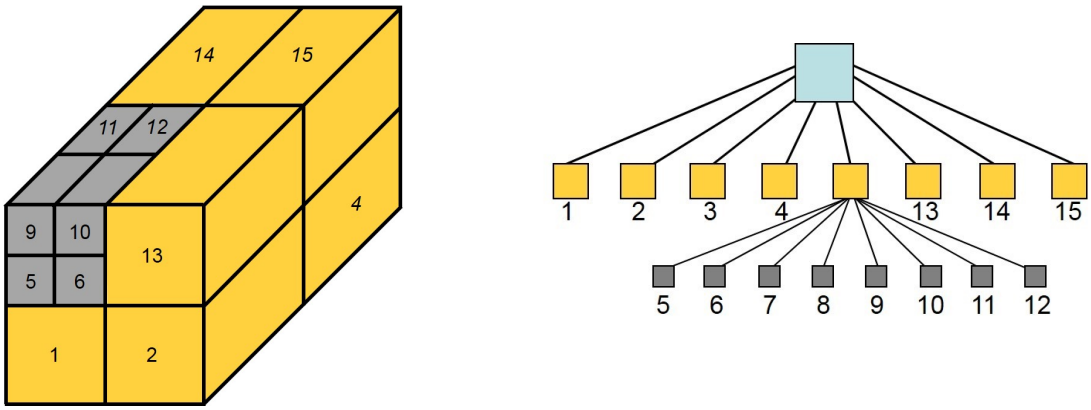

(a) 3D spatial representation in block-type system

(b) the corresponding octree representation

Fig. 2.5—Octree grid structure showing subdivision of cell A into two hierarchical levels. Nodes can be recursively decomposed into exactly eight children as show in the octree representation.

The prime motivation for the development of the quadtree is the desire to reduce the space necessary to store data by aggregating homogeneous blocks or regions (Samet, 1989). This method is often referred to as quadtree decomposition.

This analysis technique recursively subdivides a space based on a "homogeneity analysis" and provides great flexibility and speed to the partition and data storage process. Sullivan and Baker (1994) classified quadtree decomposition methods into two types depending on the construction process: top-down or bottom-down. In top-down, a judgment is first made as to whether the entire block can be represented by a single region or whether it must be divided into four sub-blocks. If the block is divided, then a decision is made for each sub-block to determine whether it needs further division, and so on. Conversely, a bottom-down construction begins with the smallest possible block and decides whether to combine it into larger blocks using a sequential analysis. **Fig.2.6** shows a comparison of these two construction methods. The decision process and homogeneity criteria will be explained in detailed in Chapter IV.

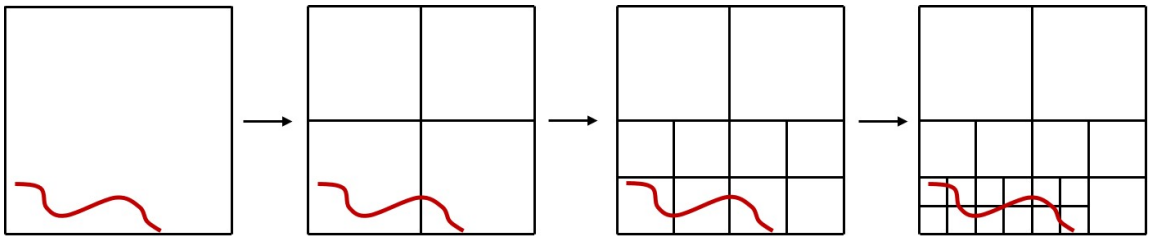

(a) Top-down, starting from coarse cells and sub-dividing as needed

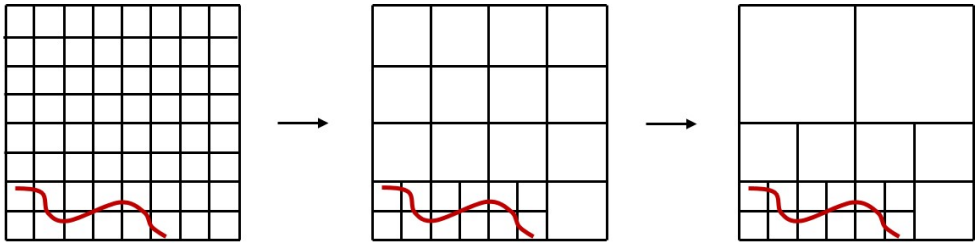

(b) Bottom-down, starting from fine cells and combining as needed

Fig. 2.6—Quadtree decomposition procedure (after Sullivan and Baker 1994).

Quadtree decomposition is often used in computer graphics for image and video compression (Sullivan and Baker 1994; Shusterman and Feder 1994; Gonzalez et al. 2003). In recent years, attention has been given to the development of hydrodynamic flow models based on adaptive quadtree grids (Liang and Borthwick 2009; Liang et al. 2007).

2.4 State of the art of adaptive refinement

The use of adaptive mesh refinement in compositional reservoir simulation has allowed reducing the computational requirements of having a fine spatial discretization across the entire reservoir model. Dynamic grids have been implemented using the two methods described in this chapter: nested systems (Biterge and Ertekin 1992; Khan et al. 1995; Nilsson et al. 2005a; Nilsson et al. 2005b) and local grid refinement (Heinemann et al. 1983; Han et al. 1987; van Batenburg et al. 2011).

Nested-system required iterative methods where information is transferred between grids. The methodology preserves the original banded coefficient matrix, providing faster solu-

tions, but it also results in interpolations of properties between coarse and fine grid. On the other hand, local grid refinement methods solved all equations simultaneously eliminating the need of basis functions for preserving mass conservation.

Adaptive methods available commercially or published in the literature present rigid schemes with two main limitations that lead to suboptimal application:

1. Refinement region is estimated from properties of previous time-step, such as saturation, compositions, gradients, etc. This time-lagging criteria results in added numerical dispersion and/or high re-gridding frequency.

2. The splitting size of the cells is defined based on user-input values, e.g. 2×2; 4×4, etc. resulting in lack of refinement flexibility.

For the development of this study the compositional reservoir simulator is derived using finite-differences following a volume balance formulation, phase equilibrium calculations with Peng-Robinson EOS, and dynamic refinement described through local grid refinement. Quadtree decomposition is implemented using a top-down approach incorporating multiple functions to evaluate the grid homogeneity.

CHAPTER III
RESERVOIR SIMULATOR

This chapter presents a brief description of the mathematical formulation of a 3D fully compositional reservoir simulator incorporating adaptive gridding. It describes the governing equations required for formulating the simulator: conservation of volume and conservation of moles. These expressions combined with auxiliary relations (well index, capillary pressure, relative permeabilities, equation of state, and viscosity model) define flow in porous media for a multi-component system. Fluid phase behavior and properties are modeled using a Peng-Robinson cubic equation of state with volume translation. Equations were discretized using finite differences and solved using a implicit-pressure, explicit-saturations and composition method (IMPESC). The algorithm was implemented in MATLAB®.

3.1 Formulation

The assumptions taken during the development of the numerical reservoir simulator are:

- Isothermal system
- Steady-state during a time step calculation
- Multi-phase (oil, gas, water) and multi-component flow represented with Darcy's law
- Instantaneous thermodynamic equilibrium between oil and gas phase
- Water immiscible in the hydrocarbon phase
- Slightly compressible rock
- No chemical reactions or adsorption

The following sub-sections describe the two governing equations needed for a compositional reservoir simulator and the auxiliary equations required for a volume-balance formulation.

3.1.1 Conservation of volume

The derivation of the reservoir simulator starts with the conservation of volume. It states that pore space is always completely filled by the total volume of the fluids. Differentiating the pore volume (V_p) as a function of pressure (p), and the total volume (V_t) as a function of pressure and number of moles (N_i), this relation results in Eq. 3.1.

$$\left(\frac{\partial V_t}{\partial p}\right)_{\vec{N}} \frac{\partial p}{\partial t} + \sum_{i=1}^{N_c} \left[\left(\frac{\partial V_t}{\partial N_i}\right)_p \left(\frac{\partial N_i}{\partial t}\right) \right] = \frac{dV_p}{dp}\frac{\partial p}{\partial t} \tag{3.1}$$

We introduce two concepts to calculate these derivatives:

- Slightly compressible rock formation. This assumption allows establishing a relation for variation of pore volume with respect to pressure (Eq. 3.1), where V_p^{ref} is the pore volume at reference pressure and c_f is the rock compressibility assumed constant.

$$\frac{dV_p}{dp} = V_p^{ref} c_f \tag{3.2}$$

- Partial molar volume ($\overline{V}_{i_B}$). Describes the change in total volume as moles of i are added to the system of block B with constant pressure, temperature, and number of moles of all components j ($N_{j\neq i}$). Appendix A shows the analytical derivation of the partial molar volume.

$$\overline{V}_{i_B} = \left(\frac{\partial V_t}{\partial N_i}\right)_{p,T,N_{j\neq i}} \tag{3.3}$$

Replacing previous concepts into Eq. 3.1 and re-arranging terms, we have:

$$\sum_{i=1}^{N_c}\left[\overline{V}_{i_B}\left(\frac{\partial N_i}{\partial t}\right)\right] = \left[V_p^{ref}c_f - \left(\frac{\partial V_t}{\partial p}\right)_{\vec{N}}\right]\frac{\partial p}{\partial t} \tag{3.4}$$

Differentiating Eq. 3.4 with respect to time (t) using backward discretization yields the following expression:

$$\sum_{i=1}^{N_c}\left[\overline{V}_{i_B}\left(\frac{N_{i_B}^{n+1} - N_{i_B}^{n}}{\Delta t}\right)\right] = \left[V_p^{ref}c_f - \left(\frac{\partial V_t}{\partial p}\right)_{\vec{N}}\right]\left(\frac{p_B^{n+1} - p_B^{n}}{\Delta t}\right) \tag{3.5}$$

where:

$\overline{V}_{i_B}$	Partial molar volume of component i in the block B
N_i	Amount of moles of component i at time levels n and $n+1$
$\vec{N}$	Total number of moles
Δt	Time difference between levels n and $n+1$
N_c	Total number of components
V_p^{ref}	Pore volume at reference pressure
c_f	Rock compressibility
V_t	Total volume
p	Pressure at time levels n and $n+1$

3.1.2 Conservation of moles

The conservation of moles describes the relationship between the inflow and outflow of moles in a control volume system in the absence of chemical reactions. For a multi-component reservoir simulator, this balance is written for every component ($i = 1, 2, ..., N_c$) accounting for the different flowing phases ($\ell = 1, 2, ..., N_p$). For the development of this work, we considered a maximum of three phases: oil, gas, and water.

Unlike structured simulators, flow leaving or entering a block B in unstructured finite-difference models can come from a variable and arbitrary number of faces. The molar balance of component i is therefore represented by Eq. 3.6.

$$\sum_{B_{adj}=1}^{N_f} \left[\sum_{\ell=1}^{N_p} q_{i,\ell_{B_{adj}}} \right] + \sum_{\ell=1}^{N_p} q_{i_{inj/prod}} = \frac{1}{\Delta t} \left(N_i^{n+1} - N_i^n \right) \tag{3.6}$$

where:

N_p	Number of phases
N_f	Number of faces connected to block B
Δt	Time difference between levels n and $n+1$
N_i	Amount of moles of component i at time levels n and $n+1$
$q_{i_{B_{adj}}}$	Molar rate of component i coming from adjacent cells
$q_{i_{inj/prod}}$	Molar rate coming from sources or sinks

The molar rate q_i can be expressed using Darcy's equation as shown in Eq. 3.7.

$$q_i = \sum_{\ell=1}^{Np} \left(Q \rho_m x_i \right)_\ell = \sum_{\ell=1}^{Np} \left(\frac{\rho_m x_i k_r k A}{\mu \Delta L} \Delta \Phi^{n+1} \right)_\ell \tag{3.7}$$

where:

Q	Volume flow rate of phase ℓ
ρ_m	Molar density of phase ℓ
x_i	Molar fraction of component i in phase ℓ
k	Absolute permeability
k_r	Relative permeability of phase ℓ
μ	Viscosity of phase ℓ
A	Area perpendicular to flow direction
ΔL	Distance between the center of the gridblock and the center of its neighboring block
$\Delta \Phi^{n+1}$	Difference of flow potentials of phase ℓ between the adjacent blocks

Calculation of flow potential and viscosity is explained in subsections 3.1.4 and 3.2.2 respectively.

From Eq. 3.7, we can define flow coefficients for every component between a block B and its adjacent blocks. Eq. 3.8 shows an example between B and B_{adj}, where ρ_m and μ are calculated using arithmetic volume-weighted average, and k_r and x_i using the upstream cell property. The geometric transmissibility T_G is calculated using harmonic average with two-point flux approximation (TPFA) method, which will be described in subsection 3.1.3.

$$a_{i_{\ell,B-B_{adj}}} = \sum_{\ell=1}^{Np} \left(\frac{\rho_m x_i k_r k A}{\mu \Delta L} \right)_\ell = \sum_{\ell=1}^{Np} \left(\frac{\rho_m x_i k_r}{\mu} \right)_\ell T_G \tag{3.8}$$

Considering all neighboring cells (N_f), the total flow for component i can be written as:

$$\sum_{\ell=1}^{Np} \Delta a_{i_\ell} \Delta \Phi_\ell^{n+1} = \sum_{B_{adj}=1}^{N_f} \left[\sum_{\ell=1}^{Np} a_{i_{\ell,B-face}} \left(\Phi_{\ell,B}^{n+1} - \Phi_{\ell,B_adj}^{n+1} \right) \right] \tag{3.9}$$

Re-writing Eq. 3.6 using the flow coefficients, we have:

$$\sum_{\ell=1}^{Np} \left(\Delta a_i \Delta \Phi^{n+1} \right)_\ell + q_{i_{inj/prod}} = \frac{1}{\Delta t} \left(N_i^{n+1} - N_i^n \right) \tag{3.10}$$

3.1.3 Discretization scheme

Two-point flux approximation (TPFA) is used to discretize flow equations between two connected cells. This is one of the simplest techniques for discretization of elliptical equations using finite-differences, and it is frequently used in the petroleum industry for reservoir simulation.

The technique approximates flux across each face assuming a linear variation of pressure within each cell. Moog (2013) explains that by imposing flux and potential continuity at

the center of the interface, we can describe a one-sided or half-transmissibility associated with a single cell (Eq. 3.11) as displayed in **Fig. 3.1**.

$$T_{G_{B,k}} = \frac{\vec{c}_{B,k} k \vec{n}_k A_k}{|\vec{c}_{B,k}|^2} \tag{3.11}$$

where:

$\vec{c}_{B,k}$	Vector from the centroid of the cell B to the centroid of the kth face
A_k	Face area
$\vec{n}_k$	Normal of the face
k	Absolute permeability

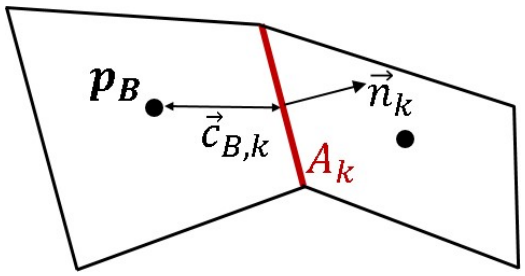

Fig. 3.1—Schematic of the calculation of half-transmissibility using two-point flux approximation.

The two half-transmissibilities are combined using harmonic average, where total transmissibility between cells 1 and 2 is calculated as shown in Eq. 3.12.

$$T_{G_{1-2}} = \frac{T_{G_1} T_{G_2}}{T_{G_1} + T_{G_2}} \tag{3.12}$$

For blocks separated by a composite interface, half-transmissibilities are calculated considering additional nodes. An example of this procedure is illustrated in **Fig. 3.2**. Flow calculations coming in and out of gridblock number 3 (highlighted in grey) is a result of flow between cell 3 and its connecting blocks, that is cells 1, 2, 4, 5, and 6. As cell 3

has a composite interface on the east side, calculation of half-transmissibilities required considering additional nodes (depicted in grey circles).

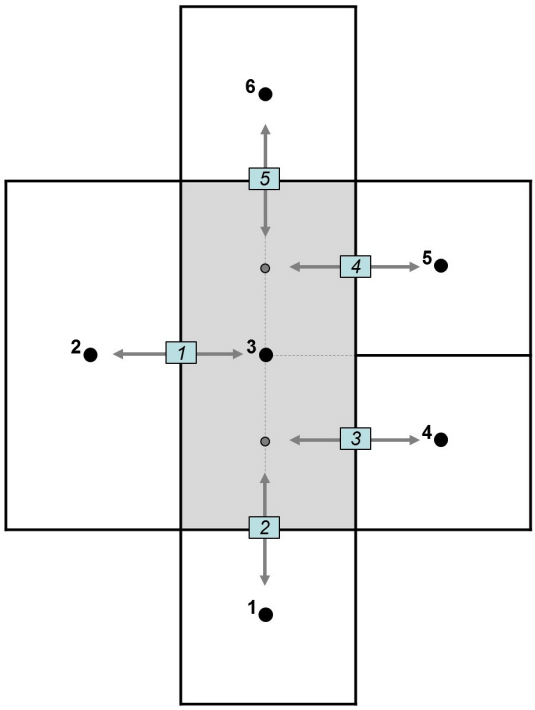

Fig. 3.2—Approximation of flow terms for composite cells with composite interfaces.

3.1.4 Auxiliary equations

In addition to the governing equations, a set of auxiliary expressions are used to define the reservoir simulation model as described in this sub-section. Equations used include Peaceman's well model, capillary pressure, and relative permeability.

Peaceman's well model

The well index is represented by Peaceman's well model (Peaceman 1978, 1983). The equation was derived to correct the bottomhole flowing pressure accounting for the difference in dimensions between the wellbore radius and the gridblock. The model introduces the concept of equivalent radius of a well, the radius at which the steady-state flowing pressure for the actual well is equal to the numerically calculated pressure for the wellblock (Peaceman, 1978). For a non-square grid with anisotropic distribution of permeabilities, the equivalent radius of a wellblock r_o is calculated with Eq. 3.13.

$$r_o = 0.28 \frac{\sqrt{\sqrt{\frac{k_y}{k_x}}\Delta x^2 + \sqrt{\frac{k_x}{k_y}}\Delta y^2}}{\sqrt[4]{\frac{k_y}{k_x}} + \sqrt[4]{\frac{k_x}{k_y}}} \tag{3.13}$$

where:

r_o	Equivalent radius of a wellblock
k_x	Absolute permeabilities in x-direction
k_y	Absolute permeabilities in y-direction
Δx	Cell thickness in x-direction
Δy	Cell thickness in y-direction

Eq. 3.13 is only valid for vertical wells. Horizontal wells require a modification to account for cell dimension and permeability on the direction in which the well is penetrated.

The production/injection molar rate of component i in phase ℓ is calculated with Eq. 3.14.

$$q_{i,\ell_{inj/prod}} = 2\pi\rho_{m\ell}x_{i,\ell}M_\ell\sqrt{k_x k_y}h\left[\ln\left(\frac{r_o}{r_w}\right) + S\right]\left(p_B - p_{wf}\right) \tag{3.14}$$

where:

S	Well skin

M	Fluid mobility
h	Thickness of the gridblock containing the well
p_B	Pressure of block B
p_{wf}	Bottomhole flowing pressure
r_o	Equivalent radius of a wellblock
r_w	Wellbore radius
$\rho_{m\ell}$	Molar density of flowing phase
$x_{i,\ell}$	Molar composition of component i in the flowing phase

Incorporating the concept of well index (W_I) that is not dependent on the fluid properties, we have:

$$W_I = 2\pi\sqrt{k_x k_y}h\left[\ln\left(\frac{r_o}{r_w}\right) + S\right] \tag{3.15}$$

We can re-write Eq. 3.14 as follow:

$$q_{i,\ell_{inj/prod}} = W_I \rho_{m\ell} x_{i,\ell} M_\ell \Big(p_B - p_{wf}\Big) \tag{3.16}$$

The difference between the block pressure and the bottomhole flowing pressure will determine if the well is injecting ($p_{wf} > p_B$) or producing ($p_B > p_{wf}$).

For production wells, the phase mobility M_ℓ is calculated using Eq. 3.17. Fluid properties (molar density and molar composition) correspond to the one calculated for the gridblock containing the well at the cell pressure.

$$M_\ell = \frac{k_{r\ell}}{\mu_\ell} \tag{3.17}$$

where:

$k_{r\ell}$	Relative permeability of phase ℓ in the gridblock containing the well
μ_ℓ	Viscosity of phase ℓ in the gridblock containing the well

For injection wells, the mobility requires to reflect the upstream conditions in the well bore (Schlumberger, 2014). This is done by defining the phase mobility using Eq. 3.18 where the mobility of the injected phase ℓ would depend on the total fluid mobility of the grid-block. Fluid properties (molar density and molar composition) are calculated by performing a flash calculation at the bottomhole flowing pressure using the injected composition. Flow of injector wells is therefore a function of the well and the gridblock condition.

$$M_\ell = \frac{k_{ro}}{\mu_o} + \frac{k_{rg}}{\mu_g} + \frac{k_{rw}}{\mu_w} \tag{3.18}$$

where:

$k_{r\ell}$	Relative permeability of phase ℓ in the gridblock containing the well
μ_ℓ	Viscosity of phase ℓ in the gridblock containing the well
k_{ro}	Relative permeability of oil in the gridblock containing the well
μ_o	Viscosity of oil in the gridblock containing the well
k_{rg}	Relative permeability of gas in the gridblock containing the well
μ_g	Viscosity of gas in the gridblock containing the well
k_{rw}	Relative permeability of water in the gridblock containing the well
μ_w	Viscosity of water in the gridblock containing the well

Capillary pressure

The capillary pressure describe the difference of pressure in the interface of two immiscible phases, a wetting and a non-wetting phase. In an oil/gas system we assume oil is the wetting phase (Eq. 3.19), and in an oil/water system, we assume water is the wetting phase (Eq. 3.20).

$$pc_{go} = p_g - p_o \tag{3.19}$$

$$pc_{ow} = p_o - p_w \tag{3.20}$$

With the capillary pressures we can describe the flow potentials between two adjacent blocks based on the oil pressure. These expressions are required for calculating Eq. 3.10.

$$\Delta\Phi_o = \Delta p_{B-B_{adj}} + \overline{\rho}_o \Delta h_{B-B_{adj}} \tag{3.21}$$

$$\Delta\Phi_g = \Delta p_{B-B_{adj}} + \overline{\rho}_g \Delta h_{B-B_{adj}} + \Delta pc_{go} \tag{3.22}$$

$$\Delta\Phi_w = \Delta p_{B-B_{adj}} + \overline{\rho}_w \Delta h_{B-B_{adj}} - \Delta pc_{ow} \tag{3.23}$$

where:

$\overline{\rho}$	Average volume-weighted mass density of the phase (oil, gas, or water)
Δh	Difference of height between blocks
$\Delta\Phi_\ell$	Difference of flow potentials of phase ℓ between adjacent blocks (ℓ =o, g, w)
Δpc_{go}	Difference in capillary pressure between blocks for gas-oil phases
Δpc_{ow}	Difference in capillary pressure between blocks for oil-water phases
$\Delta p_{B-B_{adj}}$	Difference of pressure between adjacent blocks

Relative permeabilities

In a multi-phase system, relative permeabilities describe the dimensionless effective permeability of each phase. Two-phase relative permeabilities are often measured in the laboratory and extended to three-phase flow through extrapolating techniques.

For the development of this simulator, we implemented the STONE II model (Stone, 1973). It is a modification of Stone's previous probabilistic model (Stone, 1970) with improved predictions in regions with low oil saturation. The model provides two-phase data when only two phases are flowing and interpolated data for the three-phase flow that are consistent and continuous functions of the phase saturations (Stone, 1973).

The model requires two sets of two-phase data: water-oil and gas-oil. Water and gas relative permeabilities are equal to those measured in two-phase flow, and oil relative permeability is calculated using Eq. 3.24.

$$k_{r_o} = k_{r_{ocw}} \left[\left(\frac{k_{r_{ow}}}{k_{r_{ocw}}} + k_{r_w} \right) \left(\frac{k_{r_{og}}}{k_{r_{ocw}}} + k_{r_g} \right) - k_{r_w} - k_{r_g} \right] \tag{3.24}$$

where:

k_{r_o}	Oil relative permeability for a system with oil, gas and water calculated at water saturation S_w
$k_{r_{ocw}}$	Oil relative permeability in the presence of connate water only ($S_o = 1 - S_{wc}$)
$k_{r_{ow}}$	Oil relative permeability for a system with oil and water only
$k_{r_{rw}}$	Water relative permeability at water saturation ($S_o = 1 - S_w$)
$k_{r_{og}}$	Oil relative permeability for a system with oil, gas and connate water ($S_o = 1 - S_g - S_{wc}$)
k_{r_g}	Gas relative permeability at gas saturation S_g

3.2 Fluid phase behavior

Fluid behavior is modeled using the 3-parameters cubic Peng-Robinson equation of state (EOS) developed by Peng and Robinson in 1976. This equation is used in the stability analysis to determine the number of phases existing in equilibrium at a given time. For reservoir simulation, we assume instantaneous thermodynamic equilibrium in each grid-block at any given time.

Peng-Robinson EOS (Eq. 2.7) can be expressed in its cubic form in terms of the compressibility factor Z as shown in Eq. 3.25. This expression is more commonly used for solving computational problems.

$$Z^3 - (1 - B)Z^2 + (A - 3B^2 - 2B)Z - (AB - B^2 - B^3) = 0 \tag{3.25}$$

Variables A and B are calculated using:

$$A = \frac{ap}{(RT)^2} \tag{3.26}$$

$$B = \frac{bp}{RT} \tag{3.27}$$

where:

p	Pressure
R	Gas constant
T	Absolute temperature
Z	Gas compressibility factor

Terms a and b are calculated with Eq. 3.28 and Eq. 3.29 respectively.

$$a = \sum_{i=1}^{Nc} \sum_{j}^{Nc} x_i x_j \left(1 - \kappa_{ij}\right) a_i^{0.5} a_j^{0.5} \tag{3.28}$$

$$b = \sum_{i=1}^{Nc} x_i b_i \tag{3.29}$$

where:

N_c	Number of components
κ_{ij}	Binary interaction coefficient between components i and j
x_i, x_j	Molar compositions of the phase

Parameters a_i, a_j and b_i for each component are calculated using Eq. 3.30 and Eq. 3.37. Calculation of α_i depends on the value of acentric factor ω_i. Eq. 3.32 is used for $\omega_i \leq 0.5$ while Eq. 3.33 for $\omega_i > 0.5$.

$$a_i = 0.45724\frac{R^2T_{c_i}^2}{p_{c_i}^2}\alpha_i \tag{3.30}$$

$$b_i = 0.07780\frac{RT_{c_i}}{p_{c_i}} \tag{3.31}$$

$$\alpha_i = \left[1+\left(0.037464+1.54226\omega_i-0.26992\omega_i^2\right)\left(1-\sqrt{\frac{T}{T_{c_i}}}\right)\right]^2 \tag{3.32}$$

$$\alpha_i = \left[1+\left(0.037464+1.485\omega_i-0.1644\omega_i^2+0.01667\omega_i^3\right)\left(1-\sqrt{\frac{T}{T_{c_i}}}\right)\right]^2 \tag{3.33}$$

where:

T_{c_i} Critical temperature of component i

p_{c_i} Critical pressure of component i

ω_i Acentric factor of component i

Finally, the fugacity of component i in a fluid mixture is calculated using Eq. 3.34.

$$\ln\left(\widehat{\varphi}_i^{\ell}\right) = \ln\left(\frac{\widehat{f}_i^{\ell}}{x_i p}\right) = \frac{A}{2\sqrt{2}B}\left[\frac{2\sum_{j=1}^{Nc}x_j a_i^{0.5}a_j^{0.5}\left(1-\kappa_{ij}\right)}{\alpha}-\frac{b_i}{b}\right]\ln\left(\frac{Z+2.414B}{Z-0.414B}\right) + \frac{b_i}{b}\left(Z^{\ell}-1\right)-\ln\left(Z^{\ell}-B\right) \tag{3.34}$$

where:

$\widehat{\varphi}_i^{\ell}$ Fugacity of coefficient of component i in phase ℓ

$\widehat{f}_i^{\ell}$ Fugacity of component i in phase ℓ

3.2.1 Flash equilibrium

In a multiphase system, the number of phases coexisting in equilibrium is determined by a stability analysis. The equilibrium condition for a two-phase vapor/liquid system is

given by the iso-fugacity criteria, that is when the fugacity of every component in the fluid mixture is equal in its vapor and liquid phase. This is analogous to the relation between chemical potentials reaching equilibrium when the total sum of chemical potentials is zero as the Gibbs free energy is at its minimum.

$$\widehat{f}_i^o = \widehat{f}_i^g \qquad \text{for } i = 1 \text{ to } N_c \tag{3.35}$$

The fugacity of each component can also be defined as a function of pressure (p) and fugacity coefficient ($\widehat{\varphi}_i$).

$$\widehat{f}_i^o = x_i^o \widehat{\varphi}_i^o p \tag{3.36}$$

$$\widehat{f}_i^g = x_i^g \widehat{\varphi}_i^g p \tag{3.37}$$

We define the equilibrium ratio, or K-value, for component i as its fraction in the vapor phase (x_i^g) divided by its fraction in the liquid phase (x_i^o). We can establish the equilibrium relationship in terms of K-values as follows.

$$K_i = \frac{x_i^g}{x_i^o} = \frac{\widehat{\varphi}_i^o}{\widehat{\varphi}_i^g} \tag{3.38}$$

In addition to the iso-fugacity criteria, the flash calculation is defined using two relations:

1. Material balance equation for each component, where f_v is the vapor molar fraction.

$$z_i = f_v x_i^g + (1 - f_v) x_i^o \tag{3.39}$$

2. Mole fractions of components in each phase must sum to unity.

$$\sum_{i=1}^{Nc} (x_i^g - x_i^o) = 0 \tag{3.40}$$

Combining the equilibrium ratio from Eq. 3.38 into the component material balance from Eq. 3.39, we can establish the material balance constraints in each phase (Eq. 3.41).

$$x_i^o = \frac{z_i}{1 - f_v + f_v K_i} \qquad \text{and} \qquad x_i^g = \frac{K_i z_i}{1 - f_v + f_v K_i} \tag{3.41}$$

These two equations are combined using the components' mole fraction (Eq. 3.40) for calculating a two-phase flash. This standard method was originally proposed in 1952 by Rachford and Rice (1952) and is commonly known as the Rachford-Rice equation.

$$\sum_{i=1}^{Nc} (x_i^g - x_i^o) = \sum_{i=1}^{Nc} \frac{z_i (K_i - 1)}{1 - f_v + f_v K_i} = 0 \tag{3.42}$$

The procedure for solving a liquid/vapor equilibrium was summarized by Firoozabadi (1999) in the following steps:

1. Calculate an initial estimate of the equilibrium ratio (K_i) for every component using Wilson's approximation (Wilson, 1969). It is based on the component's critical pressure (p_{c_i}), critical temperature (T_{c_i}), and acentric factor (ω_i); and the conditions of the system for pressure (p) and temperature (T).

$$\ln K_i = \ln \left(\frac{p_{c_i}}{p} \right) + 5.373 (1 + \omega_i) \left(1 - \frac{T_{c_i}}{T} \right) \tag{3.43}$$

2. Solve Rachford-Rice equation (Eq. 3.42) using Newton's method to obtain the vapor molar fraction f_v.

$$\sum_{i=1}^{Nc} (x_i^g - x_i^o) = \sum_{i=1}^{Nc} \frac{z_i (K_i - 1)}{1 - f_v + f_v K_i} = 0$$

3. Calculate molar fraction of each component in the vapor and liquid phase using Eq. 3.41.

$$x_i^o = \frac{z_i}{1 - f_v + f_v K_i} \qquad \text{and} \qquad x_i^g = \frac{K_i z_i}{1 - f_v + f_v K_i}$$

4. Calculate the fugacity coefficient of each component in the vapor and liquid phase using Eq. 3.34.

$$\begin{aligned} \ln\left(\widehat{\varphi}_i^{\ell}\right) &= \frac{A}{2\sqrt{2}B}\left[\frac{2\sum_{j=1}^{Nc} x_j a_i^{0.5} a_j^{0.5}\left(1-\kappa_{ij}\right)}{\alpha} - \frac{b_i}{b}\right]\ln\left(\frac{Z+2.414B}{Z-0.414B}\right) \\ &+\frac{b_i}{b}\left(Z^{\ell}-1\right) - \ln\left(Z^{\ell}-B\right) \end{aligned}$$

5. Update K-values for every component in the mixture from iteration k to $k+1$.

$$K_i^{k+1} = K_i^k \left(\frac{\widehat{\varphi}_i^g}{\widehat{\varphi}_i^o}\right) \tag{3.44}$$

6. Test whether convergence is achieved using $\epsilon \leq 1 \times 10^{-14}$.

$$\epsilon_i = \left|K_i^{k+1} - K_i^k\right| \tag{3.45}$$

$$\epsilon = \max\left[\epsilon_i\right] \tag{3.46}$$

7. If convergence is not satisfied, update K-values with Eq. 3.47 and repeat steps 2-7.

$$K_i^{k+1} = K_i^k \left(\frac{\widehat{f}_i^o}{\widehat{f}_i^g}\right) \tag{3.47}$$

3.2.2 Fluid properties

Once the flash equilibrium has been calculated, the information is used to determine the hydrocarbon fluid properties as shown below.

Hydrocarbon volume

From the flash equilibrium calculations we obtained the molar fractions of each hydrocarbon phase (oil and gas) and its corresponding compressibility factors. We can calculate the molar volume ($V_{m\ell}^{EOS}$) of phase ℓ using Eq. 3.48.

$$V_{m\ell}^{EOS} = \frac{Z^{\ell} RT}{p} \tag{3.48}$$

where:

$V_{m\ell}^{EOS}$	Molar volume of phase ℓ calculated with an EOS
R	Gas constant
T	Absolute temperature
p	Pressure
Z	Gas compressibility constant

Volumes calculated with Peng-Robinson EOS have shown discrepancy when compared to laboratory experiments. Therefore, it is necessary to perform a correction of volumetric properties. Correcting these systematic deviations was done using the volume translation method proposed by Peneloux et al. (1982) and described below.

For a mixture of N_c components, the phase molar volume of phase ℓ ($V_{m\ell}$) is calculated using Eq. 3.49. Peneloux et al. (1982) proposed calculating the volume correction term c using the following expression. Term b_i calculated using Eq. 3.37 previously described in this chapter.

$$V_{m\ell} = V_{m\ell}^{EOS} - c_\ell \tag{3.49}$$

$$c_\ell = \sum_{i=1}^{N_c} \left(x_i^\ell c_i^\ell\right) = \sum_{i=1}^{N_c} \left(x_i^\ell s_i b_i\right) \tag{3.50}$$

where:

N_c	Number of components
$V_{m\ell}$	Measured molar volume
V_ℓ^{EOS}	Calculated molar volume
c_ℓ	Volume parameter
c_i	Volume corrections of component i
s_i	Dimensionless shift parameter of component i
x_i^ℓ	Molar composition of component i in phase ℓ

The mass density is then calculated using Eq. 3.51.

$$\rho_\ell = \rho_{m\ell} \sum_{i=1}^{N_c} \left(x_i^\ell M_{W_i}\right) \tag{3.51}$$

where:

ρ_ℓ	Mass density of phase ℓ
$\rho_{m\ell}$	Molar density of phase ℓ
M_{W_i}	Molecular weight of component i

It is important to notice that Peneloux's volume correction does not affect the phase equilibrium calculations. Pedersen and Christensen (2006) shows that the fugacity coefficients of component i in the original and corrected equation are interrelated in through:

$$\ln \widehat{\varphi}_{i,PR} = \ln \widehat{\varphi}_{i,PR_{Pen}} + \frac{c_i p}{RT} \tag{3.52}$$

Given the equilibrium between the vapor and the liquid phase, we have the following expression where x_i^g is the mole fraction of component i in the gas phase and x_i^o is the molar fraction of component i in the oil phase.

$$\frac{x_i^g}{x_i^o} = \frac{\ln \widehat{\varphi}_{i,PR}^o}{\ln \widehat{\varphi}_{i,PR}^g} \tag{3.53}$$

The equilibrium relation using Peneloux's correction can be expressed as:

$$\frac{x_i^g}{x_i^o} = \frac{\widehat{\varphi}_{i,PR_{Pen}}^o \exp\left(\dfrac{c_i p}{RT}\right)}{\widehat{\varphi}_{i,PR_{Pen}}^g \exp\left(\dfrac{c_i p}{RT}\right)} = \frac{\widehat{\varphi}_{i,PR_{Pen}}^o}{\widehat{\varphi}_{i,PR_{Pen}}^g} \tag{3.54}$$

Water volume

The water formation volume factor molar is calculated using Eq. 3.69.

$$B_w = \frac{B_w^{ref}}{1 + X + (X^2/2)} \tag{3.55}$$

$$X = c_w(p - p^{ref}) \tag{3.56}$$

where:

B_w	Water formation volume factor
B_w^{ref}	Water formation volume factor at reference pressure
p	Pressure
p^{ref}	Reference pressure
c_w	Water compressibility

Water density (ρ_w) can be estimated from the water density at standard conditions (ρ_w^{SC}).

$$\rho_w = \frac{\rho_w^{SC}}{B_w} \tag{3.57}$$

Hydrocarbon viscosity

Using the fluid properties calculated through the phase behavior flash detailed in section 3.2, the viscosity of oil and gas is estimated using the empirical correlation proposed by Lohrenz et al. (1964). It is based on the residual viscosity concept and the theory of the corresponding states that yields Eq. 3.58.

$$\mu_\ell = \mu_\ell^* + \frac{1}{\zeta_\ell}\left[\left(0.1023 + 0.023364\rho_{mr_\ell} + 0.058533{\rho_{mr_\ell}}^2 - 0.40758{\rho_{mr_\ell}}^3 + 0.0093324{\rho_{mr_\ell}}^4\right)^4 - 0.0001\right] \tag{3.58}$$

where:

μ_ℓ	Viscosity of phase ℓ
μ_ℓ^*	Viscosity of phase ℓ at atmospheric pressure
ζ_ℓ	Viscosity parameters of phase ℓ
ρ_{mr_ℓ}	Reduced molar density

Eq. 3.59 - Eq. 3.61 shows the calculation for the phase viscosity at atmospheric pressure μ_ℓ^*, the phase viscosity parameter ζ_ℓ, and the reduced molar volume ρ_{mr_ℓ}.

$$\mu_\ell^* = \frac{\sum x_i^\ell \mu_i^* \sqrt{M_{w_i}}}{\sum x_i^\ell \sqrt{M_{w_i}}} \tag{3.59}$$

$$\zeta_\ell = \frac{T_{pc_\ell}^{1/6}}{M_{w_\ell}^{1/2} p_{pc_\ell}^{2/3}} \tag{3.60}$$

$$\rho_{mr_\ell} = \frac{\rho_\ell \sum_{i=1}^{Nc} x_i^\ell V_{c_i}}{M_{w_\ell}} \tag{3.61}$$

where:

x_i^ℓ	Molar composition of phase ℓ
M_{w_i}	Molecular weight of component i
M_{w_ℓ}	Molecular weight of phase ℓ at atmospheric pressure

V_{c_i} Critical volume for component i

ρ_ℓ Mass Density of phase ℓ

μ_i^* Viscosity of component i at low pressure

Phase properties T_{pc_ℓ} (critical temperature), p_{pc_ℓ} (critical pressure), and $M_{w\ell}$ (molecular weight) are calculated using a simple mixing rule. The viscosity of component i in the ℓ phase at low pressure (μ_i^*) is calculated with Eq. 3.65 depending on the reduced temperature and viscosity parameter for the component.

$$T_{pc_\ell} = \sum_{i=1}^{Nc} x_i^\ell T_{c_i} \tag{3.62}$$

$$p_{pc_\ell} = \sum_{i=1}^{Nc} x_i^\ell p_{c_i} \tag{3.63}$$

$$M_{w_\ell} = \sum_{i=1}^{Nc} x_i^\ell M_{w_i} \tag{3.64}$$

$$\mu_i^* = \begin{cases} \dfrac{0.00034\left(T_{r_i}\right)^{0.94}}{\zeta_i}, & \text{if } T_{r_i} \leq 1.5 \\ \dfrac{0.0001776\left(4.58T_{r_i} - 1.67\right)^{5/8}}{\zeta_i}, & \text{if } T_{r_i} > 1.5 \end{cases} \tag{3.65}$$

where:

T_{pc_ℓ} Pseudo critical temperature of phase ℓ

T_{c_i} Critical temperature of component i

p_{c_i} Critical pressure of component i

p_{pc_ℓ} Pseudo critical pressure of phase ℓ

The reduced temperature of component i (T_{r_i}) is calculated using Eq. 3.66 and the viscosity parameter of component i (ζ_i) is calculated with Eq. 3.67.

$$T_{r_i} = \frac{T}{T_{c_i}} \tag{3.66}$$

$$\zeta_{r_i} = \frac{T_{c_i}^{1/6}}{M_{w_i}^{1/2} p_{c_i}^{2/3}} \tag{3.67}$$

Viscosity of water

The viscosity of water is calculated using Eq. 3.68 (Schlumberger, 2014).

$$\mu_w = \frac{\mu_w^{ref}}{1 + Y + (Y^2/2)} \tag{3.68}$$

$$Y = -c_v(p - p^{ref}) \tag{3.69}$$

where:

μ_w	Water viscosity
μ_w^{ref}	Water viscosity at reference pressure
p	Pressure
p^{ref}	Reference pressure
c_v	Water viscosibility

3.3 Numerical approach

To satisfy simultaneously the volume and the molar balance constraints, we combine Eq. 3.5 and Eq. 3.10.

$$\sum_{i=1}^{N_c} \left[\overline{V}_{i_B} \sum_{\ell=1}^{Np} \left(\Delta a_i \Delta \Phi^{n+1} \right)_\ell + q_{i_{inj/prod}} \right] = \frac{1}{\Delta t} \left[V_p^{ref} c_f - \left(\frac{\partial V_t}{\partial p} \right)_{T,\vec{N}} \right] \left(p_B^{n+1} - p_B^n \right) \tag{3.70}$$

For simplicity, we use the term V_{oid_B} and re-write the combined balance equation. The derivation of the V_{oid} term is described in Appendix B.

$$\sum_{i=1}^{N_c}\left[\overline{V}_{i_B}\sum_{\ell=1}^{Np}\left(\Delta a_i \Delta\Phi^{n+1}\right)_\ell + q_{i_{inj/prod}}\right] = \frac{1}{\Delta t}V_{oid_B}\left(p_B^{n+1}-p_B^n\right) \tag{3.71}$$

The volume balance formulation uses an IMPESC approach, lagging in densities, capillary pressure differentials, flow coefficients, partial molar volume, and Void term. Incorporating the well flow rate (Eq. 3.76) and the difference of potentials (Eq. 3.21 - 3.22), we can represent flow between block B and adjacent B_{adj} as:

$$\begin{aligned}
\frac{1}{\Delta t}V_{oid_B}{}^n\left(p_B^{n+1}-p_B^n\right) &= \sum_{i=1}^{N_c}\left\{\overline{V}^n_{i_B\ell}\left[(a_{i_\ell}W_I)^n\left(p_B^{n+1}-p_{wf}^{n+1}\right)\right.\right. \\
&+ \Delta a^n_{io,B-B_{adj}}\Delta p^{n+1}_{B-B_{adj}} + \Delta a^n_{io,B-B_{adj}}\overline{\rho}^n_o\Delta h_{B-B_{adj}} \\
&+ \Delta a^n_{ig,B-B_{adj}}\Delta p^{n+1}_{B-B_{adj}} + \Delta a^n_{ig,B-B_{adj}}\overline{\rho}^n_g\Delta h_{B-B_{adj}} \\
&+ \Delta a^n_{iw,B-B_{adj}}\Delta p^{n+1}_{B-B_{adj}} + \Delta a^n_{iw,B-B_{adj}}\overline{\rho}^n_w\Delta h_{B-B_{adj}} \\
&\left.\left. + \Delta a^n_{ig,B-B_{adj}}\Delta pc^n_{go,B-B_{adj}} - \Delta a^n_{iw,B-B_{adj}}\Delta pc^n_{ow,B-B_{adj}}\right]\right\}
\end{aligned} \tag{3.72}$$

Re-arranging the previous equation for all unknown from time level $n+1$ on the left hand size and known variables on the right hand size of the equation, we have Eq. 3.73 describing the general finite-difference equation for a compositional simulator. There would as many equations as number of grid blocks in the model.

$$A^n\underline{p}^{n+1} = b^n \tag{3.73}$$

where:

$$
\begin{aligned}
A^n &= \sum_{B_{adj}=1}^{N_f}\left[\sum_{i=1}^{N_c}\left(\overline{V}_{i_B}^n\sum_{\ell=1}^{Np}\Delta a_{i\ell,B-B_{adj}}^n\right)\right]+\sum_{i=1}^{N_c}\left(\overline{V}_{i_B}^n\sum_{\ell=1}^{Np}a_{i_\ell}WI\right]-\frac{1}{\Delta t}V_{oid_B}^n \\
b^n &= -\frac{1}{\Delta t}V_{oid_B}^n p_B^n+\sum_{i=1}^{N_c}\left(\overline{V}_{i_B}^n\sum_{\ell=1}^{Np}a_{i_\ell}WI\right)p_{wf}-\sum_{i=1}^{N_c}\left[\overline{V}_{i_B}^n\sum_{\ell=1}^{Np}(\Delta a_{i\ell}^n\overline{\rho}_\ell^n\Delta h)\right] \\
&\quad -\sum_{i=1}^{N_c}\left(\overline{V}_{i_B}^n\Delta a_{ig}^n\Delta pc_{go}^n\right)+\sum_{i=1}^{N_c}\left(\overline{V}_{i_B}^n\Delta a_{iw}^n\Delta pc_{ow}^n\right)
\end{aligned}
$$

3.3.1 Time-stepping

The overall time step is solved using IMPESC method, previously developed by Acs et al. (1985), where the system of equations is solved similar to a black-oil model with pressures solved implicitly and compositions and molar densities solved explicitly. This involves evaluating A and b at the previous iteration k to solve the pressure for the next timestep p^{n+1}. Because we are lagging some variables ($\overline{\rho}_\ell$, $\Delta pc_{v\ell}$, $\Delta a_{i\ell}$, $\overline{V}_{i\ell}$, V_{oid}) in the development of our equations that depend on the pressure solution, we performed a sequential procedure to correct for this approximation, where A and b are updated in each iteration and the process is repeated until the convergence criteria is reached.

Because the IMPESC formulation treats inter-block flow rates implicitly in pressure and explicitly in saturations and compositions, the solution is conditionally stable only when Eq. 3.74 is met for every component i in every gridblock B. Physically, it means that no fluid particle can travel farther than a gridblock in a single time-step.

$$
CFL_{i_B}=\frac{F_{i_B}\Delta t}{V_{p_B}}<1 \tag{3.74}
$$

For this study, we used the CFL definition as proposed by Coats (2003a,b) and shown in Eq. 3.74, where F_B is a function of rate and reservoir properties and is described in Eq. 3.75. Q_o and Q_g are the sum of all oil outflow rates from a block to its neighbors at reservoir conditions. This equation is calculated for each component in every gridblock.

$$F_{i_B} = \left(\frac{Q_o \rho_{m_o} x_i^o + Q_g \rho_{m_g} x_i^g}{S_o \rho_{m_o} x_i^o + S_g \rho_{m_g} x_i^g} \right)_B \tag{3.75}$$

The maximum time step for stable solutions will be constrained by the CFL number of each component in every cell ($\max [CFL_{i_B}]$), allowing for a maximum CFL of 1.

3.3.2 IMPESC procedure

The steps for IMPESC are summarized below, where k is the iteration number and n is the result from the previous time step. This procedure is repeated in every time calculation.

1. For $k = 0$ and Δt set $p^k = p^n$
2. Perform a flash calculation and determine fluid properties at p^k
3. Calculate relative permeabilities (function of saturations) and viscosities at p^k
4. Calculate flow coefficients, partial molar volumes ($\overline{V}_i$), and Void term at p^k
5. Solve p^{k+1} from Eq. 3.73

$$A^k \underline{p}^{k+1} = b^k$$

6. Solve $q_{i_{inj/prod}}^{k+1}$ from Eq. 3.76 using p^{k+1}

$$q_{i_{inj/prod}}^{k+1} = \sum_{\ell=1}^{Np} \left[a_{i_\ell} W_I \left(p_B - p_{wf} \right) \right]$$

7. Calculate the total moles using Eq. 3.10

$$N_i^{k+1} = N_i^n + \sum_{\ell=1}^{Np} \left(\Delta a_i \Delta\Phi^{n+1}\right)_\ell + q_{i_{inj/prod}}^{k+1}$$

8. Calculate the new fluid composition for every gridblock using Eq. 3.76.

$$z_i^{k+1} = \frac{N_i^{k+1}}{\sum_{i=1}^{Nc} N_i^{k+1}} \tag{3.76}$$

9. Calculate the CFL_i number for every component in a cell using equations 3.74 and 3.75.

$$CFL_{i_B} = \frac{F_{i_B}\Delta t}{V_{p_B}}$$

$$F_{i_B} = \left(\frac{Q_o\rho_{m_o}x_i^o + Q_g\rho_{m_g}x_i^g}{S_o\rho_{m_o}x_i^o + S_g\rho_{m_g}x_i^g}\right)_B$$

10. Calculate the convergence criteria for every gridblock B using ϵ_i as displayed in Eq. 3.77.

$$\epsilon_B = \left|\frac{p_B^{k+1} - p_B^k}{p_B^k}\right| \tag{3.77}$$

11. Test if convergence criteria are achieved with ϵ, CFL, and if the iteration number k is less than maximum allowed.

$$CFL = \max\left[CFL_B\right] \leq 1 \tag{3.78}$$

$$\epsilon = \max\left[\epsilon_B\right] \leq 1x10^{-3} \tag{3.79}$$

12. If the criteria is met, then $p^n = p^{k+1}$ and Δt is incremented using Eq. 3.81 if permitted by the CFL constraint.

$$\Delta t = \Delta t + \frac{\Delta t}{2} \tag{3.80}$$

13. If the criteria is not met but the $k < k_{max}$, then update variables for $k = k + 1$. Repeat steps 2 to 11 until convergence criterion are satisfied.

$$\begin{aligned} p^k &= p^{k+1} \\ N_i^k &= N_i^{k+1} \\ z_i^k &= z_i^{k+1} \\ q_{i_{inj/prod}}^k &= q_{i_{inj/prod}}^{k+1} \end{aligned}$$

14. If the criteria is not met and we reached the maximum number of iterations allowed ($k < k_{max}$), reduce the time step using Eq. 3.81 and repeat the procedure from step 1 using the information at n level. A minimum delta time is defined by the user (e.g. 1×10^{-5} days), after which Δt is not further reduced and the simulation is terminated.

$$\Delta t = 0.5\Delta t \tag{3.81}$$

Fig. 3.3 shows a simplified flowchart describing the calculations using the IMPESC approach.

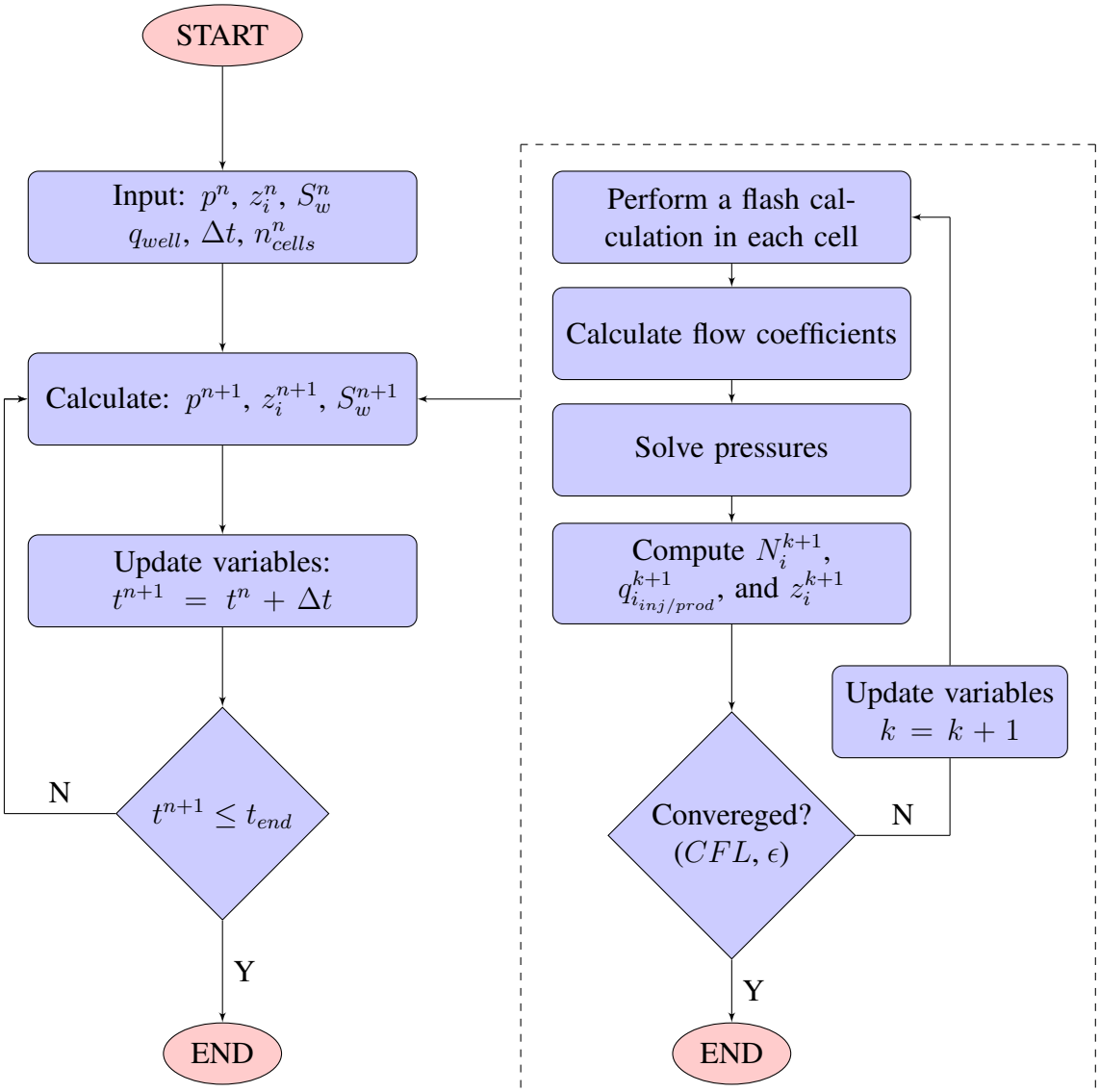

Fig. 3.3—General flowchart for computing the sequential solution using implicit-pressure and explicit in saturations and compositions.

3.3.3 Performance improvement

To increase the computational efficiency of the algorithm, the following features were included to reduce the total CPU time.

Parallel processing

Using MATLAB's built-in function for parallel processing, the nested loop calculating the thermodynamic properties was programmed to use multiple cores. The flash equilibrium calculation is performed for every cell as a function of known properties from the previous iteration. The independence between each cell allows dividing the model into smaller pieces (a defined number of gridcells) to carry out simultaneous calculations.

Restart

The restart option creates a new simulation run based on results from an existing case. The model is initialized using the variables stored during the original simulation, and continues the computations as requested in the new input data. With this feature we can change the well scheduling data, maximum time step, maximum number of iterations, etc.

3.4 Comparative case study

The finite-difference simulator developed in this study using an IMPESC approach was compared with the commercial simulator ECLIPSE (Schlumberger, 2014) with a fully-implicit solution. We used a simple homogeneous model of 17.3 acre area representing an inverted five-spot pattern with a thickness of 90 ft. The model is spatially discretized with 675 cells ($15 \times 15 \times 3$), where each cell has a dimension of 50 feet in the x-direction, 67 feet in the y-direction, and 33.33 feet in the z-direction. **Fig. 3.4** shows a representation of the simulation model.

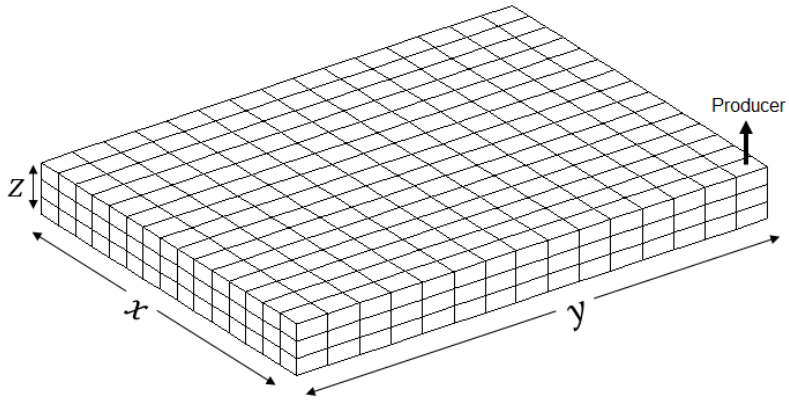

Fig. 3.4—3D reservoir simulation grid with 675 cells (nx=15, ny=15, and nz=3) used to validate the developed compositional reservoir simulator.

A production well is located in the corner of the model, producing with constraints of maximum gas production (800 MSCF/day) or minimum bottomhole flowing pressure (4,000 psia) for 250 days. This simple mechanistic model allows covering the two basic production controls throughout the simulation: maximum rate and minimum bottom-hole flowing pressure.

3.4.1 Fluid characterization

The fluid represents a 28.1 °API oil. The laboratory analysis of the sample was obtained from the GeoMark RFDbase data base (www.rfdbase.com). It corresponds to the offshore Gemini field in the Golf of Mexico, block "Mississippi Canyon 291".

The characterization and preparation of the fluid sample for simulation was performed in a previous study by Nguyen (2009) who evaluated different CO_2 injection strategies for the reservoir. The oil was initially characterized in the laboratory with 12 pseudo-components, and grouped into five by Nguyen in order to reduce the calculation time in the simulator. The final grouping and composition is shown in **Table 3.23**.

Table 3.23—Original and group fluid composition with 12 and 5 components

ORIGINAL		GROUPED	
Component	z_i **(fraction)**	**Component**	z_i **(fraction)**
CO_2	0.0006	CO_2	0.0006
N_2	0.0020	$N_2 + C_1$	0.6002
C_1	0.5982		
C_2	0.0233	$C_2 - C_4$	0.0654
C_3	0.0222		
iC_4	0.0048		
nC_4	0.0151		
iC_5	0.0072	$C_5 - C_6$	0.0403
nC_5	0.0100		
C_6	0.0231		
C_{7+}	0.2935	C_{7+}	0.2935

A calibration process was performed by Nguyen using the differential liberation and constant composition expansion tests showing a good match of the fluid properties before and after grouping, including the following experiments: oil density, liquid and vapor viscosity, oil relative volumes, gas-oil ratio, and gas compressibility factor. The final set of

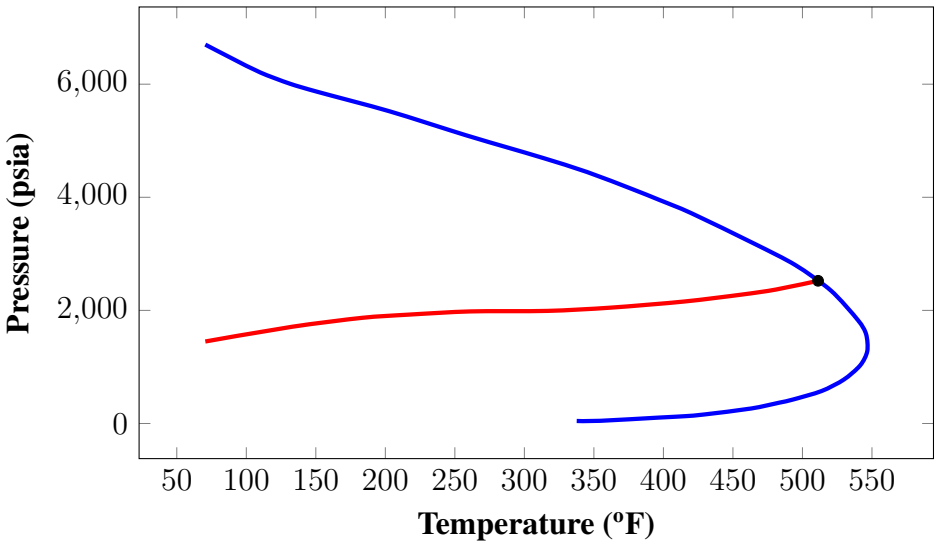

Fig. 3.5—Predicted saturation envelope of the volatile oil used for this study grouped into 5-component. It shows that at reservoir temperature of 200 °F, the fluid has a bubble point pressure of 5,558 psia.

properties used to characterize the oil are listed in **Table 3.24** while **Fig. 3.2** shows the fluid phase behavior. The comparison study was performed at 200 °F. At this temperature, the bubble point pressure is 5,558 psia.

Water was characterized with a formation volume factor of 1.029 RB/STB at a reference pressure of 5,750 psia, and a compressibility of $3\times10^{-6}\ psi^{-1}$.

Table 3.24—Fluid properties with 5 pseudo-components

Component	$\mathbf{M}_w$	$\mathbf{p}_c$ **(psia)**	$\mathbf{T}_c$ **(° F)**	$\mathbf{Z}_c$	**Acentric Factor**	**Volume shift**
CO_2	44.01	1071.3	88.5	0.5379	0.2869	-0.0131
$N_2 + C_1$	16.09	667.8	-117.4	0.1916	0.013	-0.1443
$C_2 - C_4$	43.37	578.5	132.3	0.2650	0.0257	-0.1382
$C_5 - C_6$	78.94	510.1	605.1	0.2321	0.1916	-0.0587
C_{7+}	265.35	357.9	630.0	0.5134	0.8913	-0.8630

Table 3.25—Binary interaction coefficients

Component	CO_2	$N_2 + C_1$	$C_2 - C_4$	$C_5 - C_6$	C_{7+}
CO_2	0				
$N_2 + C_1$	0.1	0			
$C_2 - C_4$	0	0	0		
$C_5 - C_6$	0	0.018	0	0	
C_{7+}	0	0.041	0	0	0

3.4.2 Rock properties and initial conditions

The reservoir is at constant depth of 12,540 feet having homogeneous properties throughout the model, with porosity of 0.2, horizontal permeability of 60 mD, and vertical to horizontal permeability ratio of 0.1. The reservoir was initialized with a pressure of 8,868 psia and temperature of 200 °F. At this conditions, the reservoir fluid exits in as single liquid phase. The synthetic reservoir has an initial water saturation of 0.4.

A full summary of the rock properties is shown in **Table 3.26**.

Table 3.26—Rock properties used in the comparative case study

Property	**Value**
Pressure, psia	8,868
Temperature, °F	200
Water saturation, fraction	0.4
Top depth, ft	12,540
Porosity, fraction	0.2
Horizontal permeability, mD	60
Permeability ratio (k_v/k_h)	0.1
Reference pressure, psia	5,868
Rock compressibility, 1/psia	4×10^{-6}

3.4.3 Saturation functions

Three-phase relative permeabilities are calculated using STONE II model as described in section 3.1.4. The input requires two-phase relative permeabilities for oil-water (**Fig. 3.7**) and oil-gas (**Fig. 3.6**). Oil-water system assumes gas saturation is zero, while oil-gas system measurements are taken at connate water saturation ($S_{wc} = 0.16$).

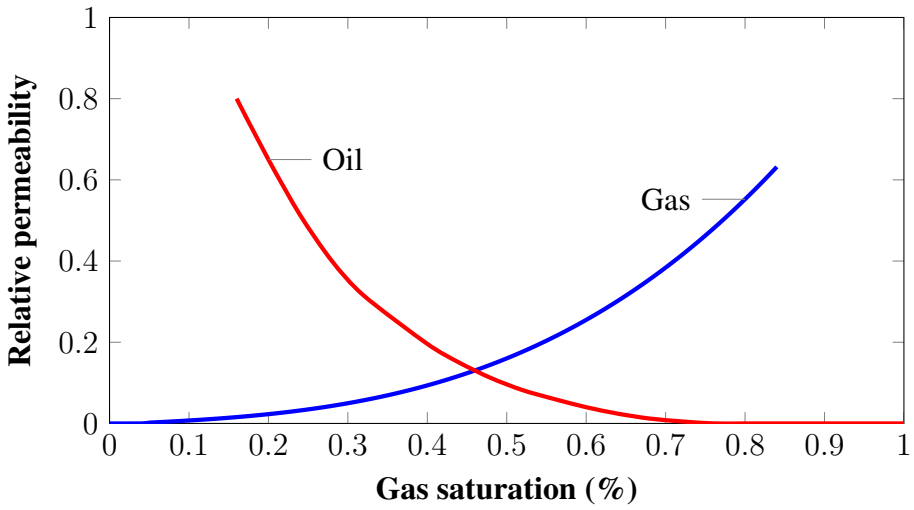

Fig. 3.6—Relative permeability curves for oil and gas which determines the relative flow when both phases are present.

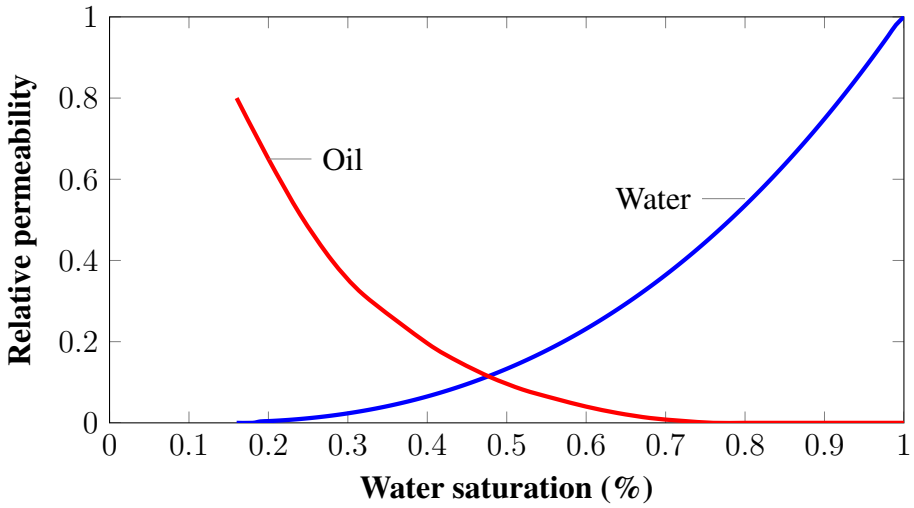

Fig. 3.7—Relative permeability curves for oil and water which determines the relative flow when both phases are present.

3.4.4 Comparison results

Results comparing production response from the simulator developed and a commercial reservoir simulator Eclipse are displayed in **Figs 3.8-3.14**, showing a good match between the two simulators.

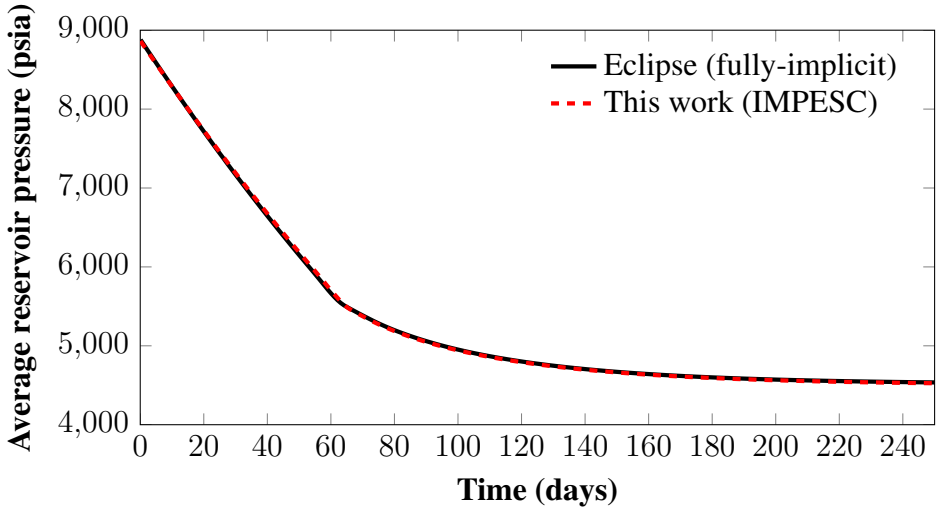

Fig. 3.8—Average reservoir pressure (hydrocarbon-volume weighted) showing a good agreement between the developed simulator and Eclipse.

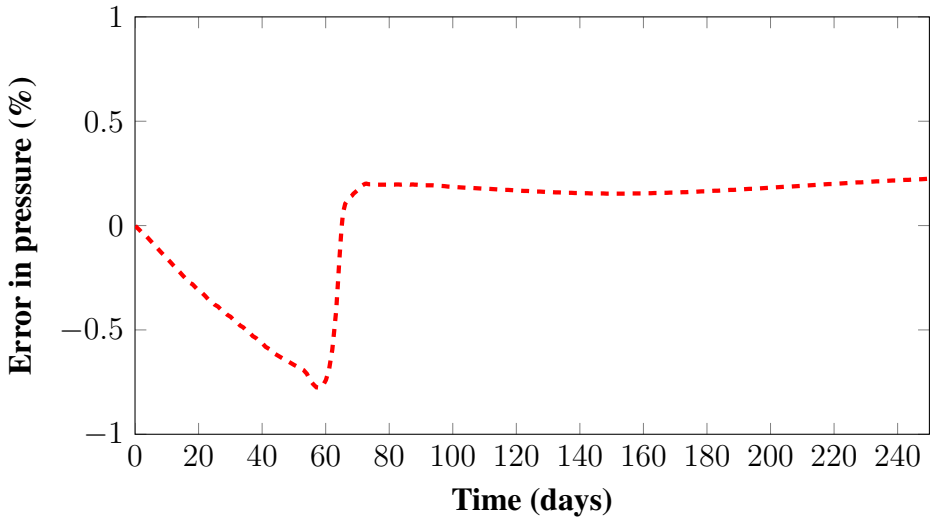

Fig. 3.9—Difference in average reservoir pressure between our IMPESC simulator and Eclipse showing average difference of 0.23%

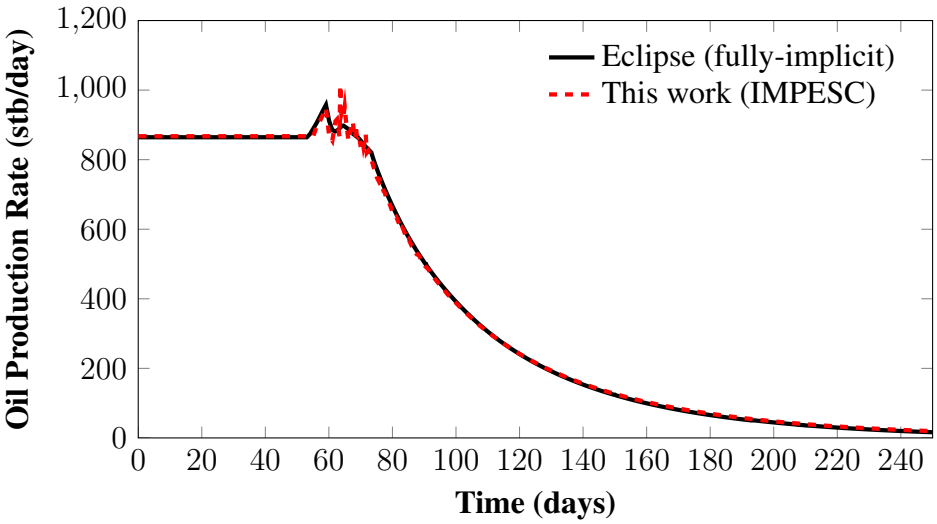

Fig. 3.10—Oil production rate showing a good agreement between the newly developed simulator and Eclipse.

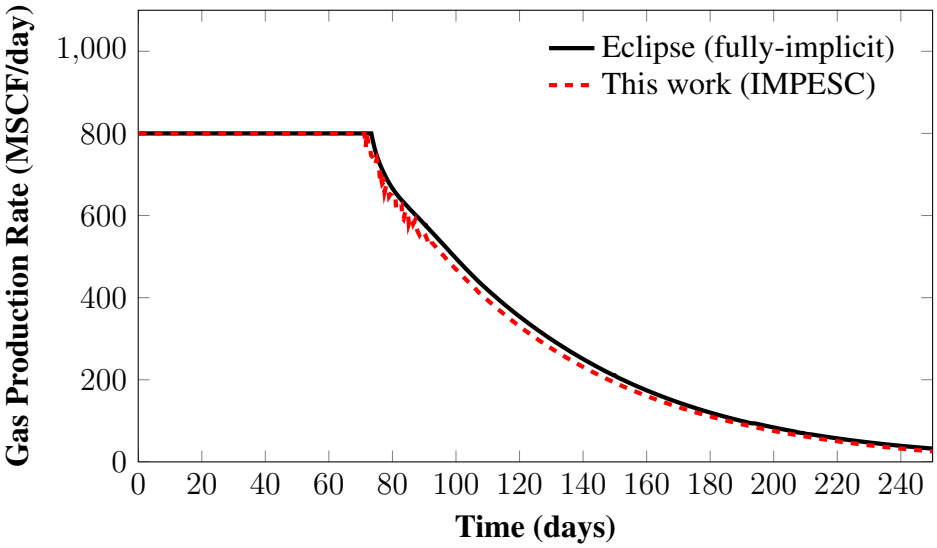

Fig. 3.11—Gas production rate showing a good agreement between the newly developed simulator and Eclipse. Reservoir production is initially controlled by maximum rate and switched to bottom-hole flowing control at 70 days.

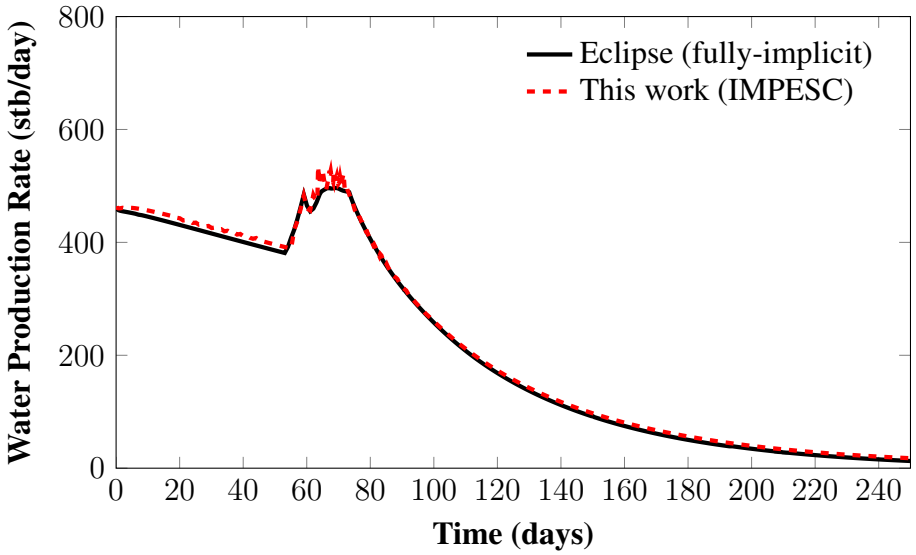

Fig. 3.12—Water production rate comparing showing a good agreement between the newly developed simulator and Eclipse.

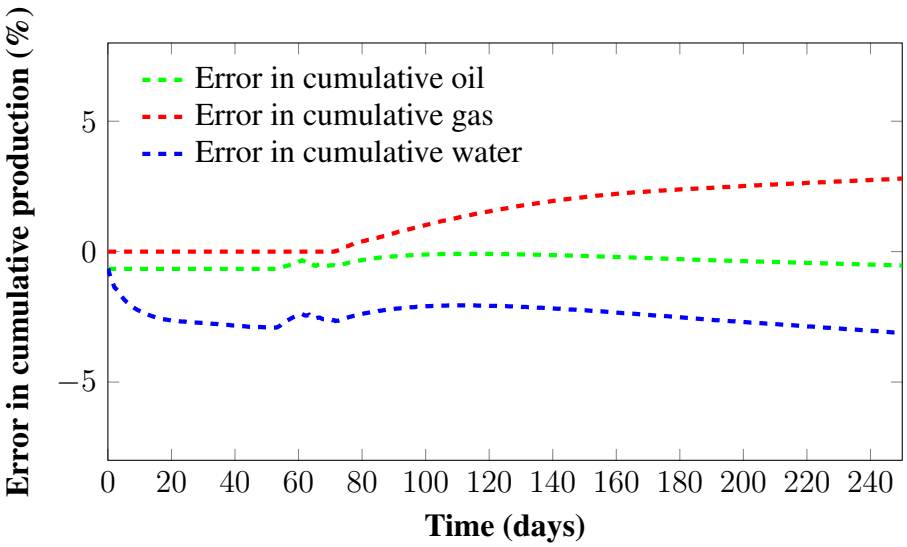

Fig. 3.13—Difference in cumulative production between our IMPESC simulator and Eclipse showing average difference of 0.4% for cumulative oil, 1.2% for cumulative gas, and 2.5% for cumulative water.

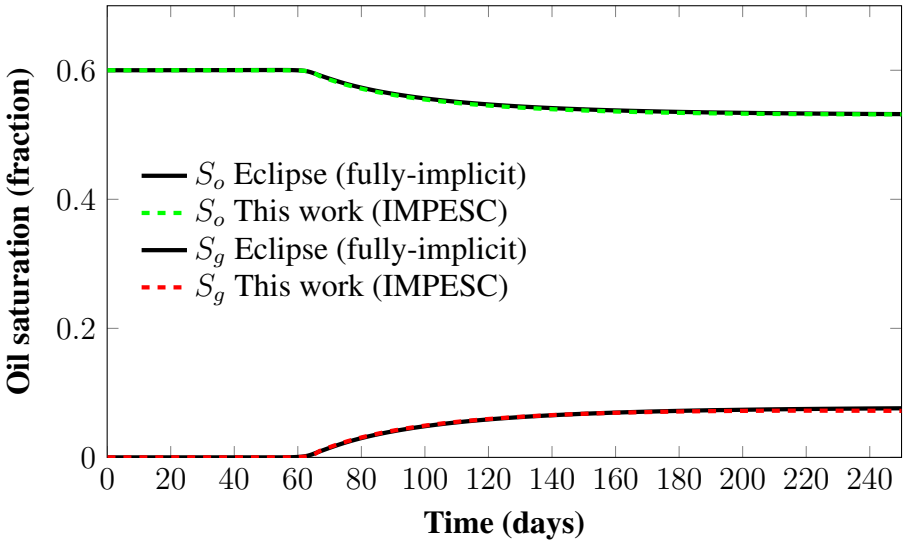

Fig. 3.14—Average volume-weighted oil and gas saturation showing a good agreement between the newly developed simulator and Eclipse.

CHAPTER IV
ADAPTIVE MESH REFINEMENT ALGORITHM

This chapter presents the adaptive mesh refinement and coarsening (AMRC) algorithm developed for modeling gas injection processes. It describes the major steps of the procedure: 1) fine-grid calculation; 2) forecast of injection front by combining streamline and the solute transport equation to identify regions with high compositional gradient; 3) selection of gridblock spatial discretization through analysis of homogeneity with quadtree decomposition; and 4) update of new grid and transfer of dynamic reservoir properties.

4.1 Overall process

The dynamic gridding technique proposed in this work performs *a priori* grid discretization by predicting the movement of the injection front and then selecting grid sizes based on forecasted compositions. **Fig. 4.1** shows the general workflow for dynamically refining and coarsening the simulation grid. First, we follow the procedure of a conventional reservoir simulation, starting with the input data, initializing the variables, and performing flow calculation. Before moving to the next time step (t^{n+1}), we evaluate if there is a need to update the grid to properly capture the flow movement.

The process for creating an adaptive grid can be viewed in four major steps:

1. Transfer the dynamic properties to a fine grid and perform a single time-step calculation.

2. Forecast movement and compositions of the injection front using streamlines and the analytical solution of the solute transport equation.

3. Select grid refinement levels in each region automatically, using quadtree decomposition to evaluate spatial homogeneity of forecasted compositions.

4. Update the simulation grid and transfer the dynamic properties.

The succeeding time-steps use this new adaptive grid to perform the flow calculations, until it is necessary to create a new grid.

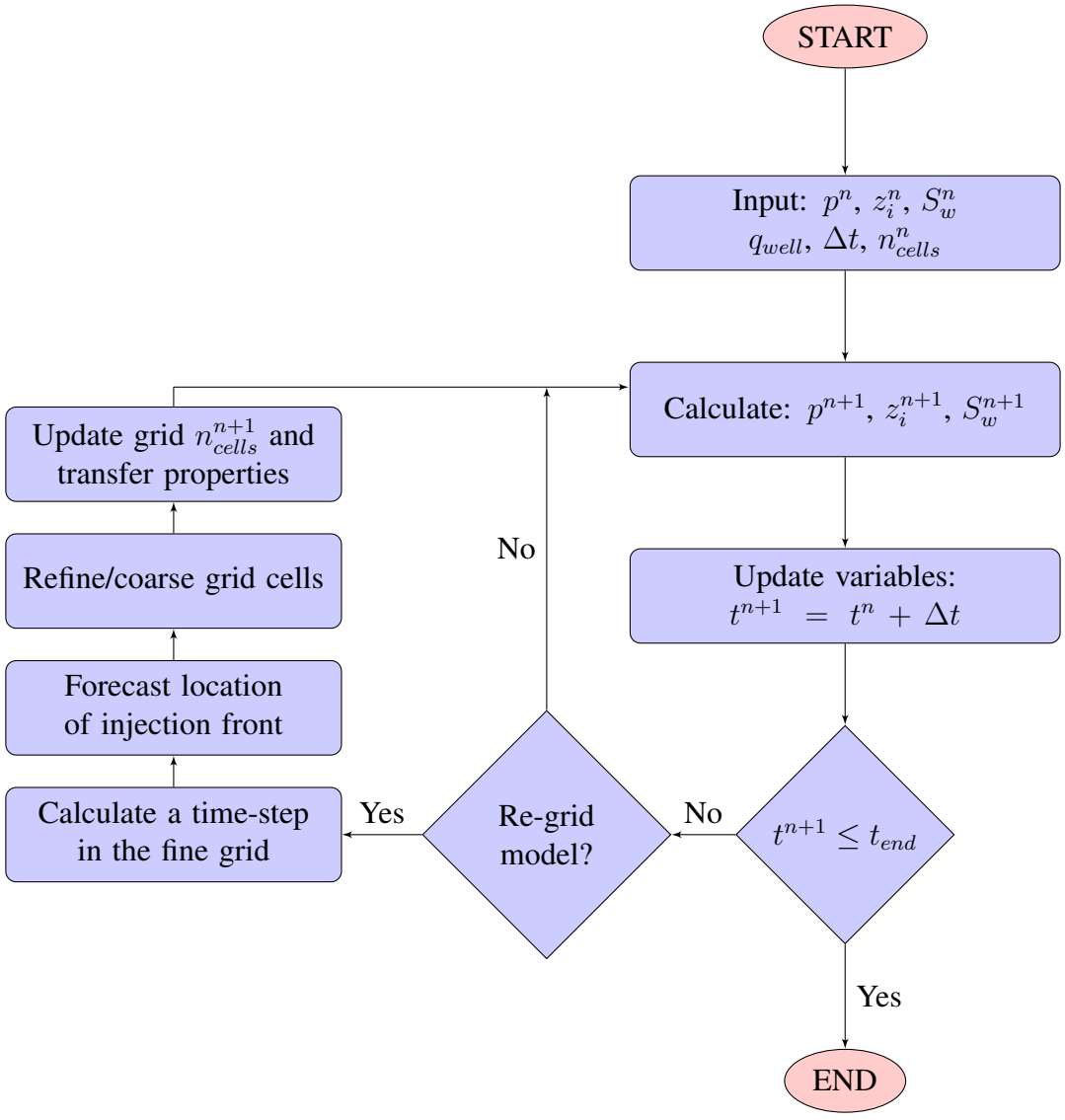

Fig. 4.1—General flowchart for adaptive mesh refinement and coarsening. After a time step converges, AMRC determines whether there is need to create a new grid. The location of the injection front is then forecasted to determine new grid cell sizes (refined or coarsened). Finally, reservoir properties are transferred to the new grid, improving spatial representation of future calculations.

The following sections describe the process for forecasting compositions (section 4.2), refining and/or coarsening the simulation grid (section 4.3), and updating the grid structure (section 4.4). The process for transferring the dynamic properties from the adaptive to the fine grid (required to complete step 1) will be described in section 4.4.2. The frequency of re-meshing, which depends on the dynamic conditions of the reservoir, will be described in section 4.5.

4.2 Forecast of injection front

Forecasting movement and shapes of compositional fronts starts with the finite-difference solution obtained using a fine grid model, from which flux distribution is calculated for all cells following the procedure detailed in Chapter III. Subsequently, fluxes and particle trajectory calculations allow reducing the 3-dimensional model into a series of 1-dimensional streamlines across the entire reservoir model; the user defines the number of streamlines to be calculated. The result is a series of curves tangential to the velocity field, representing an instantaneous "snapshot" of the pressure field at a given time and defining fluid trajectories from injector to producer. Finally, implementing the analytical solution to the convection-dispersive equation (CDE) along each streamline allows estimating the compositional distributions across the reservoir. This procedure forecasts the location, width, and shape of the injection front for future calculations.

4.2.1 Tracking of streamlines

Tracking particle trajectory from the injector well to the producer follows the semianalytical algorithm proposed by Pollock (1988). This technique generates pathlines and time-of-flight (or time-of-travel) using velocities obtained from finite-difference calculations. The main assumption of this model is that each directional velocity varies linearly within a cell in its own coordinate direction. The main advantage of this linear interpolation is the ability to integrate the three principal velocity components to obtain analytical

expressions that describe the flow trajectory. The result is a continuous velocity vector along each individual grid cell that satisfy the conservation of mass equation everywhere within the cell (Pollock, 1988).

For a single gridcell, the total interstitial velocity is calculated by dividing the volumetric flow rate across the face by its cross-sectional area and the cell porosity. Linear interpolation is used to express the interstitial velocity along any position on the x-direction, as shown in Eq. 4.1 and Eq. 4.2. For illustration purposes, **Fig. 4.2** shows a simple 2D schematic of the analytical calculations in a single gridblock.

$$v_x = v_{x,0} + g_x(x - x_0) \tag{4.1}$$

$$g_x = \frac{v_{x,\Delta x} - v_{x,0}}{\Delta x} \tag{4.2}$$

where:

g_x	Interstitial velocity gradient in the x-direction
v_x	Interstitial velocity the x-direction
$v_{x,0}$	Interstitial velocity at $x = x_0$
$v_{x,\Delta x}$	Interstitial velocity at $x = \Delta x$
x	Position in the x-direction
x_0	Origin in the x-direction
Δx	Cell dimension in the x-direction

The rate of change of velocity of a particle p as it moves through a three-dimensional cell is defined using Eq. 4.3.

$$\left(\frac{dv_x}{dt}\right)_p = \left(\frac{dv_x}{dx}\right)\left(\frac{dx}{dt}\right)_p \tag{4.3}$$

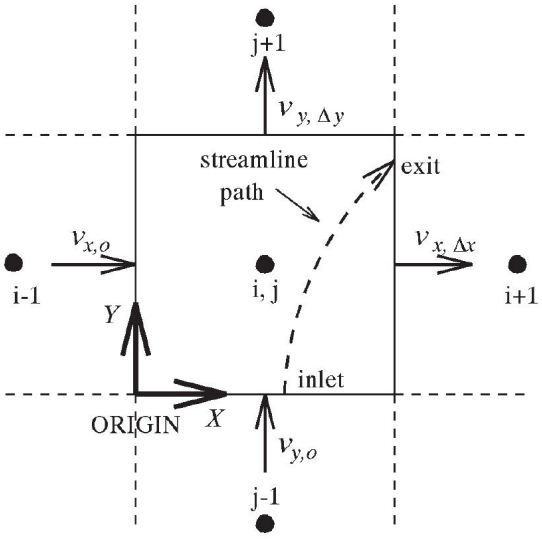

Fig. 4.2—Streamline representation in 2D showing the analytical calculation from entry point to exit (from Batycky et al. 1997)

By definition we have:

$$\left(\frac{dx}{dt}\right)_p = v_{x_p} \tag{4.4}$$

And by differentiating the interstitial velocity v_x (Eq. 4.1) with respect to x we obtain:

$$\frac{dv_x}{dx} = g_x \tag{4.5}$$

Substituting Eq. 4.4 and Eq. 4.5 into Eq. 4.3 yields

$$\left(\frac{dv_x}{dt}\right)_p = g_x v_{x_p} \tag{4.6}$$

Finally, by integrating Eq. 4.6 and incorporating the definition of particle velocity (v_{x_p}) from Eq. 4.4, we can obtain the time required for a particle to reach the exit face along the x-direction.

$$\Delta t_x = \frac{1}{g_x} \ln \left[\frac{v_{x,0} + g_x(x_e - x_0)}{v_{x,0} + g_x(x_i - x_0)}\right] \tag{4.7}$$

where:

x_e Exit particle position

x_i Inlet particle position

An analogous derivation is performed for y- and z-direction:

$$\Delta t_y = \frac{1}{g_y} \ln \left[\frac{v_{y0} + g_y(y_e - y_0)}{v_{y0} + g_y(y_i - y_0)} \right] \tag{4.8}$$

$$\Delta t_z = \frac{1}{g_z} \ln \left[\frac{v_{z0} + g_z(z_e - z_0)}{v_{z0} + g_z(z_i - z_0)} \right] \tag{4.9}$$

Equations 4.7-4.9 determine the time required for a particle to exit the cell in each of the three-dimensions. The correct exit face would be the one requiring the minimum value of Δt as shown in Eq. 4.10. For example, if Δt_x is the less than Δt_y and Δt_z, then the particle will leave the cell across face x_2.

$$\Delta t_m = \min \left[\Delta t_x, \Delta t_y, \Delta t_z \right] \tag{4.10}$$

Using the minimum time, we can calculate the exact location of the streamlines using the following expressions.

$$x_e = \frac{1}{g_x} \left[v_{xi} \exp \left(g_x \Delta t_m \right) - v_{x0} \right] + x_0 \tag{4.11}$$

$$y_e = \frac{1}{g_y} \left[v_{yi} \exp \left(g_y \Delta t_m \right) - v_{y0} \right] + y_0 \tag{4.12}$$

$$z_e = \frac{1}{g_z} \left[v_{zi} \exp \left(g_z \Delta t_m \right) - v_{z0} \right] + z_0 \tag{4.13}$$

The procedure outlined here is for tracing streamlines in a single cell. Tracking the entire trajectory is a sequential process. We start in the cell containing the injector well and we

move cell-by-cell in the simulation grid following the equations described previously. The calculations ends when the streamline reaches a producer well or a stagnation region as shown in **Fig. 4.3**. To cover the entire reservoir model, we trace several streamlines from different initial points in the cell containing the well. The number of streamlines is defined by the user and will depend on the flow characteristics of the model.

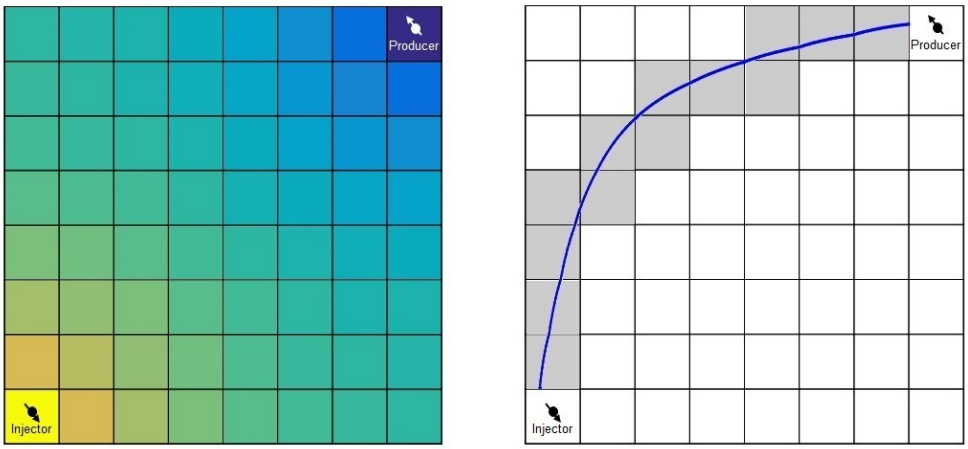

(a) Pressure distribution (b) the corresponding streamlines

Fig. 4.3—Sequential process for tracing the streamline trajectory from injector to producer wells.

For this work, when two hydrocarbon phases are expected, two sets of streamlines are calculated corresponding to each of the flowing phases (oil and gas). The flux between cells B and B_{adj} is calculated using the following expressions.

$$Q_{o,B-B_{adj}} = \frac{k_{ro}^{ups} T_G}{\overline{\mu}_o} \left(\Phi_{o,B} - \Phi_{o,B_{adj}}\right) \tag{4.14}$$

$$Q_{g,B-B_{adj}} = \frac{k_{rg}^{ups} T_G}{\overline{\mu}_g} \left(\Phi_{g,B} - \Phi_{g,B_{adj}}\right) \tag{4.15}$$

where:

k_r^{ups}	Upstream relative permeability of oil (o) or gas (g) phase
$Q_{B-B_{adj}}$	Volumetric rate of oil (o) or gas (g) phase between cells B and B_{adj}
T_G	Geometric transmissibility between cells B and B_{adj} (Eq. 3.11)
$\overline{\mu}$	Average viscosity of oil (o) or gas (g) phase
Φ	Flow potentials of oil (o) or gas (g) phase

Phase streamlines do not necessarily follow the trajectory of the total flux. Kumar et al. (2009) explained that streamlines based on total flux may fail in capturing the reservoir dynamics, including flow of a dominant phase, appearance and disappearance of phases, and movement of injected components. This is particularly important in cases with gas injection in reservoir below the bubble point pressure, where the injected component is transported in both the liquid and vapor phase at different rates.

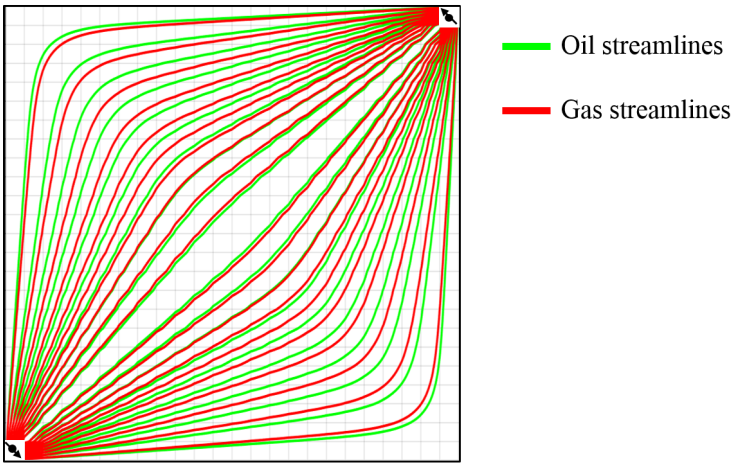

Fig. 4.4—Streamlines for the oil and gas phase showing different trajectory.

The steps to trace a single streamline for a specific phase can be summarized as follow:

1. Compute the phase velocities from the flux distribution obtained using the finite-difference model.

2. Begin tracing the streamline in the face of a cell containing the injector well.

3. Calculate the time-of-flight in each direction using Eq. 4.7-4.9.

4. Estimate the exit face of a particle by selecting the minimum time-of-flight Δt_m (Eq. 4.10).

5. Using Δt_m, determine the streamline coordinates using Eq. 4.11-4.13.

6. With the exit face, locate the new cell to be traced, e.g. if the particle exits the face in the y-direction, then it will enter cell $[i, j+1, k]$.

7. Repeat steps until the particle reaches a sink.

4.2.2 Analytical forecast of compositions

The convection-dispersion equation (CDE) for a 1-dimensional system enables forecasting the compositional distribution along each streamline (spanning the entire reservoir model) in future time steps. This equation describes the concentration of a displacing component as a function of distance and time and provides valuable information on the position, width, and shape of the injection front at different times.

The analytical derivation to the CDE starts with the conservation of a displacing component for an isothermal miscible displacement process in a homogeneous permeable medium. Lake (1989) describes the equation using its dimensionless form assuming incompressible rock and fluid and ideal mixing.

$$K_\ell \frac{\partial^2 C_i}{\partial x^2} - v\frac{\partial C_i}{\partial x} - \frac{\partial C_i}{\partial t} = 0 \tag{4.16}$$

where:

C_i Mass concentration of component i

K_ℓ Longitudinal dispersion coefficient

t	Time
x	Length
v	Interstitial velocity ($v = u/\phi$)
ϕ	Porosity

In dimensionless terms, Eq. 4.16 becomes:

$$\frac{1}{N_{P_e}}\frac{\partial^2 C_{D_i}}{\partial x_D^2} - \frac{\partial C_{D_i}}{\partial x_D} - \frac{\partial C_{D_i}}{\partial t_D} = 0 \tag{4.17}$$

Using the following dimensionless variables:

$$C_{D_i} = \frac{C_i - C_{iI}}{C_{iJ} - C_{iI}} \tag{4.18}$$

$$X_D = \frac{x}{L} \tag{4.19}$$

$$t_D = \int_0^t \frac{u}{\phi L} dt \tag{4.20}$$

where:

C_{D_i}	Dimensionless concentration
C_{iI}	Initial mass composition
C_{iJ}	Injected mass composition
L	Total length
ϕ	Porosity

In this form, we also incorporate the Peclet number (N_{Pe}), representing the ratio of convective to dispersive transport shown in Eq. 4.21. The dispersivity coefficient K_ℓ is a property of the media and its estimation is described later in this chapter.

$$N_{Pe} = \frac{\text{convection}}{\text{dispersion}} = \frac{uL}{\phi K_\ell} \tag{4.21}$$

Defining the system using the following initial and boundary conditions.

Boundary conditions

$$C_{D_i}(x_D = \infty, t_D) = 0, \quad t_D \geq 0 \tag{4.22}$$

$$C_{D_i}(x_D = -\infty, t_D) = 1, \quad t_D \geq 0 \tag{4.23}$$

Initial condition

$$C_{D_i}(x_D, 0) = 0, \quad x_D \geq 0 \tag{4.24}$$

The final analytical solution is derived by Ogata and Banks (1961) using the Laplace transform. Eq. 4.25 shows the final solution in its dimensionless form. This equation can provide fast and accurate forecast describing the movement of a component in a miscible at time.

$$C_{D_i} = \frac{1}{2}\operatorname{erfc}\left(\frac{x_D - t_D}{2\sqrt{\frac{t_D}{N_{Pe}}}}\right) + \left[\frac{e^{x_D N_{Pe}}}{2}\operatorname{erfc}\left(\frac{x_D + t_D}{2\sqrt{\frac{t_D}{N_{Pe}}}}\right)\right] \tag{4.25}$$

Eq. 4.25 is solved in a sequential process following a similar approach as the one used for tracing streamlines. We begin the process by computing the relative time-of-flight of each cell considering the forecast time. Starting in the injector well, we compute the distribution of compositions in the corresponding cell using the injected mass concentration (C_{iJ}) and the initial cell concentration (C_{iI}). Using the CDE, we then determine the concentration that will be exiting that cell, and subsequently, entering the next one. The "exit" concentration will be the entry point for calculating the CDE in the succeeding cell. The process is repeated cell-by-cell until the concentration along the entire streamline has been calcu-

lated. For a desired time t, the methodology forecasts the compositional variation along each streamline as shown in **Fig. 4.5**.

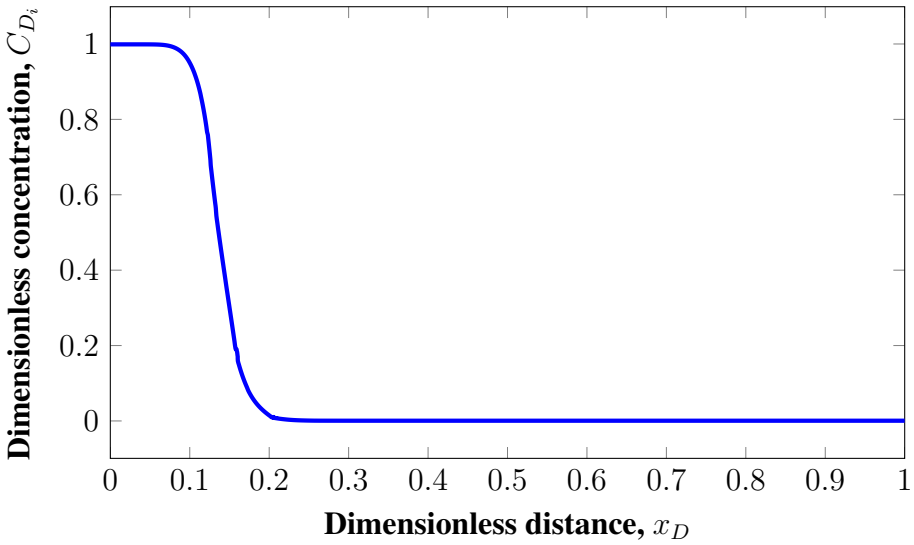

Fig. 4.5—Distribution of composition along one streamline using the convection-dispersion equation allowing to identify three different regions: swept ($C_{Di} \simeq 1$), mixed front ($0 < C_{Di} < 1$), and unswept ($C_{Di} \simeq 0$).

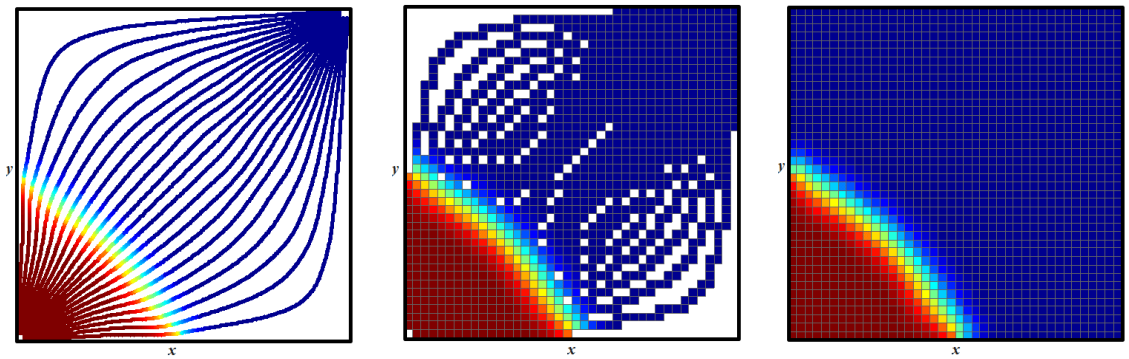

(a) Compositions forecast using the CDE

(b) Mapping compositions to a 3D grid system

(c) Interpolation to fill properties of the reservoir model

Fig. 4.6—Procedure for combining streamlines and the solute transport equation to predict movement of the injection front at a specific time.

Calculation of compositions is performed for every streamline in the model, as shown in **Fig. 4.6-a**. Then, the forecasted 1D compositions are mapped into the 3D grid system (**Fig. 4.6-b**) and interpolated between plotted regions to properly cover the entire reservoir model (**Fig. 4.6-c**). This solution is used to determine the level of grid refinement required for the upcoming time-step calculations.

4.2.3 Calibration of dispersivity coefficient

The dispersivity coefficient is a property of the media and defines the shape and width of the injection front. When advection dominates the transport process, we have a sharp front described with high Peclet numbers. On the other hand, low Peclet numbers produce spread fronts (**Fig 4.7**).

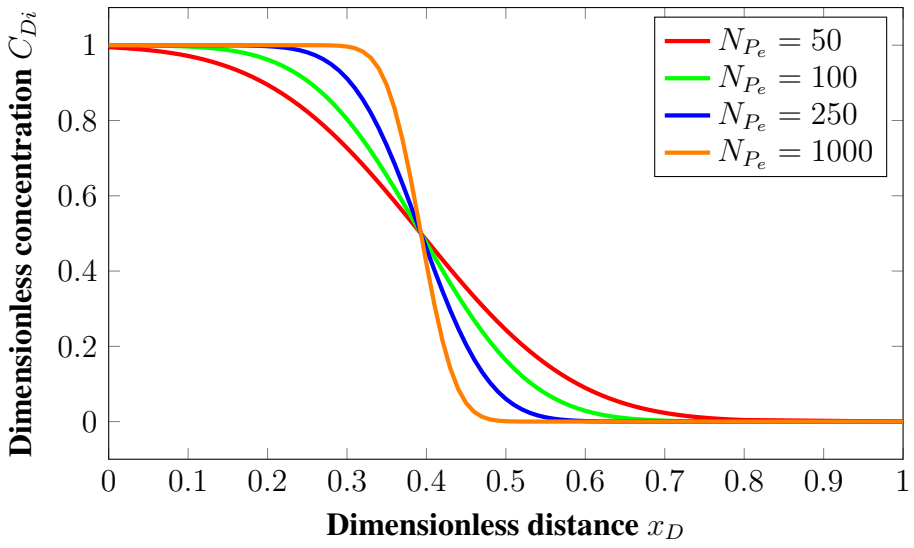

Fig. 4.7—Effect of Peclet number (N_{P_e}) in the forecast of injection fronts, showing sharp fronts with large N_{P_e} and spread fronts with low N_{P_e}.

To calculate the value of dispersivity (K_ℓ) that represents the finite-difference flow, we perform the following calibration process.

1. Set a calibration period $\Delta t = t_2 - t_1$ at the start of the simulation, where the length of Δt is defined by the user.

2. At t_1, perform a finite-difference calculation to estimate the pressure and flux distribution in the system. These values are stored for future use as FD_1.

3. Calculate the trajectory of streamlines using the finite-difference solution obtained at t_1 (FD_1).

4. Using the finite-difference solution FD_1 and an initial guess value for K_l, we forecast the distribution of compositions along the streamline for time t_2. The forecasted compositions are stored for future comparisons as SL_1.

5. Continue the finite-difference calculations until reaching target time t_2. This may involve multiple time steps as required by the convergence criteria and CFL limit.

6. At t_2, perform a finite-difference calculation to estimate the pressure and flux distribution (FD_2).

7. Map along the initial streamlines the compositions obtained using the finite difference solution at time t_2 (FD_2); values are stored as SL_2.

8. Calculate the difference between the compositions of the two sets of streamlines (SL_1 and SL_2) using the minimum mean square error.

$$Error = \sum \left[(SL_1 - SL_2)^2 \right] \tag{4.26}$$

9. Minimize the error by evaluating the dispersivity parameter K_l when calculating the compositions in SL_1 (Step 4). Minimization of the error is done using the Golden Section Search algorithm (Gerald and Wheatley, 1984).

4.3 Select grid refinement

Quadtree spatial discretization is the basis for selecting the size of grid-blocks in the model. Quadtree is a tree-like data structure that allows organizing information using a root value and subtrees of children. Each parent cell can be recursively subdivided into four (in 2D), or eight (in 3D), children as shown in Fig 2.4 and Fig 2.5. The prime motivation for using quadtrees is the ability to reduce space required to store data by aggregating homogeneous blocks through quadtree decomposition (Samet, 1989). This method provides great flexibility and speed to the partition and data storage process with promising applications in adaptive mesh refinement algorithms.

4.3.1 Quadtree decomposition

Quadtree decomposition determines the final level of refinement in each simulation region by evaluating dynamic and static properties of the reservoir (e.g., composition, pressure, permeability, facies). This analysis technique recursively subdivides a space based on a "homogeneity analyses." For this implementation, we use a top-down construction as described in Chapter II, where we first evaluates whether a single block can represent a region or if dividing it into sub-blocks or children is needed.

Although there is no technical limit on the number of children that a cell can be split, for practical applications the user specifies the maximum level of refinement that will be allowed in the model (n^{max}). This is an important consideration for IMPESC solutions, as the time-step is limited by the volumetric flow passing through a cell, therefore, the use of very small cell would restrict the model to very small time-steps.

The algorithm depicted in **Fig. 4.8** begins by evaluating the use of the coarsest cell dimension allowed in the model ($2^n \times 2^n \times 2^n$ with $n = n^{max}$ as the maximum level of refinement).

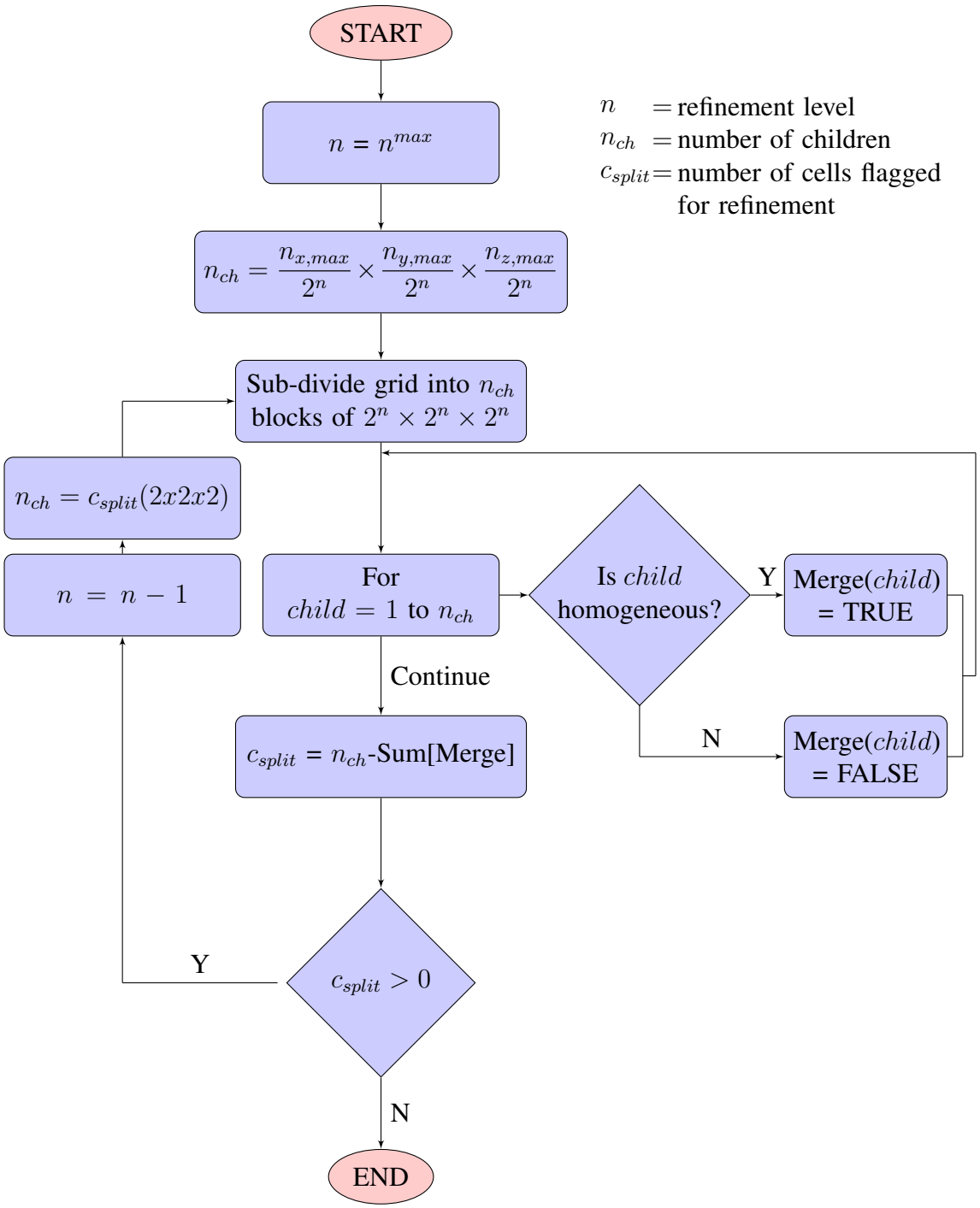

Fig. 4.8—Flowchart for quadtree decomposition showing the sequential calculation of a top-down approach.

For each proposed child or sub cell, it extracts all its dynamic and static properties and tests their values for homogeneity using a combination of one or more coarsening functions. If the proposed child cell meets the homogeneity test, then it assigns logical functions "TRUE" specifying that the cell will not require further splitting; consequently, merging the child. If it fails the test, then it assigns "FALSE" to split the cell. All cells classified as "FALSE" will repeat the homogeneity analysis for subsequent refinement levels (with $n^{new} = n^{old} - 1$) until the cell does not require further splitting. In addition, cells containing production or injection wells are discretized using fine blocks for better representation of high velocity regions.

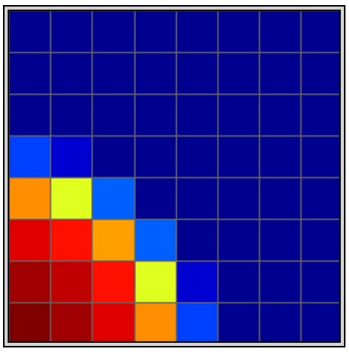

(a) Step 1: Fine resolution image (8×8)

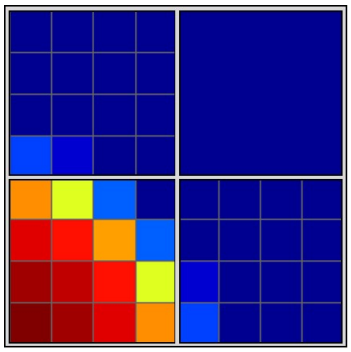

(b) Step 2: Analyses for cells 4×4

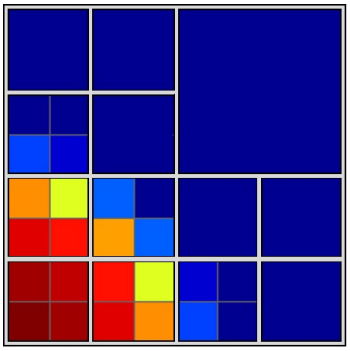

(c) Step 3: Analyses for cells 2×2

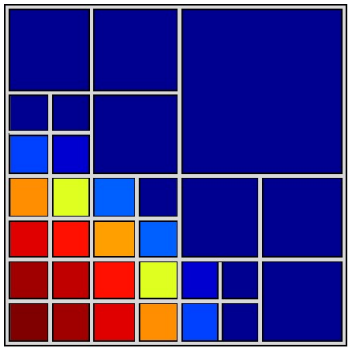

(d) Step 4: Final adaptive mesh refinement grid

Fig. 4.9—Quadtree decomposition process for a top-down construction with 3-levels, showing the reduction in number of cells from 64 to 31 while preserving spatial details.

To illustrate the proposed methodology, **Fig. 4.9** shows an example of quadtree decomposition of a 2D grid with front-like properties. Initially, the fine grid (sub-figure Step 1) has 64 cells arranged in an 8×8 structure ($2^n \times 2^n$, where $n = 3$). Following a top-down construction, the first step is evaluating whether the grid can be represented by sub-cells (child) merging 4×4 cells (sub-figure Step 2); all sub cells passing the homogeneity test are merged; in this case, only the top-right corner. Cells failing the test are evaluated to be represented by children merging 2×2 cells (sub-figure Step 3); if the homogeneity test passes, cells would be merged. We repeat the process until the grid reaches the finest level of refinement (sub-figure Step 4).

4.3.2 Coarsening functions

Selection of the coarsening functions is a problem-specific analyses based on the process characteristics and the reservoir description. Using quadtree decomposition, we have the flexibility to combine multiple static and dynamic properties to represent the dominant flow mechanisms.

This works presents two simple homogeneity functions based on the fluid molar composition (z_i) and the permeability distribution (k). The homogeneity test determines if there is sufficient variations on these properties when evaluating each sub-grid or child. Large variation suggests a discontinuity of the property (e.g. an injection front) that would require fine spatial discretization.

The homogeneity tolerance is a critical factor to obtain accuracy and computational gains when using adaptive mesh refinement models. Tight criteria would result in very fine grids that may not provide significant computational improvement. On the other hand, loose criteria can affect the accuracy of the solution. Current applications of adaptive gridding take a holistic approach for selecting homogeneity tolerances. We suggest performing sensi-

tivity analysis to select a threshold value that can effectively represent the process under study.

Although we only discuss the coarsening functions used in this study (composition and permeability), similar applications are readily extendable for other type of property analyses and statistical parameters (e.g. variance, standard deviation).

Compositions

Injection of gas into the reservoir results in continuous changes in the compositional distribution across the model. Tracking composition of the injected fluid in the displacing and displaced phase is key to select a grid resolution that reduces numerical dispersion.

$$z_i^{max} - z_i^{min} < \text{tolerance}_z \tag{4.27}$$

Permeability

For highly heterogeneous reservoirs, the use of quadtree decomposition and homogeneity analysis allows reducing the size of the model by merging cells based on the static properties of the reservoir, such as the permeability, rock facies, presence of fractures, etc. The use of unstructured grid geometry provides the flexibility to reduce the number of cells while preserving key geologic features, like channels, sealing layers, and fractures.

The local grid refinement based on the static properties can be done as a pre-processing step or dynamically in the simulation run. In this research, we evaluated the use of the following test for restricting merging cells based on their value of horizontal permeability.

$$k_h^{min} > k_h^{max} \times \text{tolerance}_k \tag{4.28}$$

4.4 Create new grid

The result of the quadtree decomposition is a set of logical functions describing the spatial discretization of the simulation model. The fundamental unstructured nature of adaptive gridding requires monitoring parent-children relationships while defining new faces and connections in the simulator. Creating a new grid involves re-ordering the cell in the model and transferring the dynamic and static properties. Every time a new grid is created, we destroy previous adaptive grids to reduce data storage that can compromise computational performance.

4.4.1 Cell re-ordering

Because of the dynamic nature of adaptive grids, the cell re-ordering process has to be repeated every time a new adaptive grid is created. Indices for each cell in the model are assigned following the same top-down approach used in the quadtree decomposition. We first number the coarsest cells using a natural-like order. We then move to the next level of refinement and continue numbering cells. We continue the process for all every refinement levels until all cells have been numbered. The final grid is a smaller model that requires fewer cells to solve the problem, thus providing an improved computational performance.

The unstructured discretization of the simulation model results in a more complicated system compared to a conventional structured grid. In a conventional grid, each cell has a fixed number of connecting faces (six for a 3-dimensional model). This results in a coefficient matrix that also has a fixed number of elements in a sparse and banded structure as it is shown in **Fig. 4.10**. On the other hand, in an adaptive grid, a cell may be connected to a variable number of faces depending on the level of refinement of each cell. This leads to a more complicated system of equations and a more complicated matrix structure that contain scatter elements as shown in **Fig. 4.11**.

The order in which cells are numbered has a significant impact in the computational performance of the algorithm. The more regular the matrix is, the easiest it is to solve it. Further studies are required to understand the impact of the cell ordering scheme to improve further the computational performance of the adaptive method.

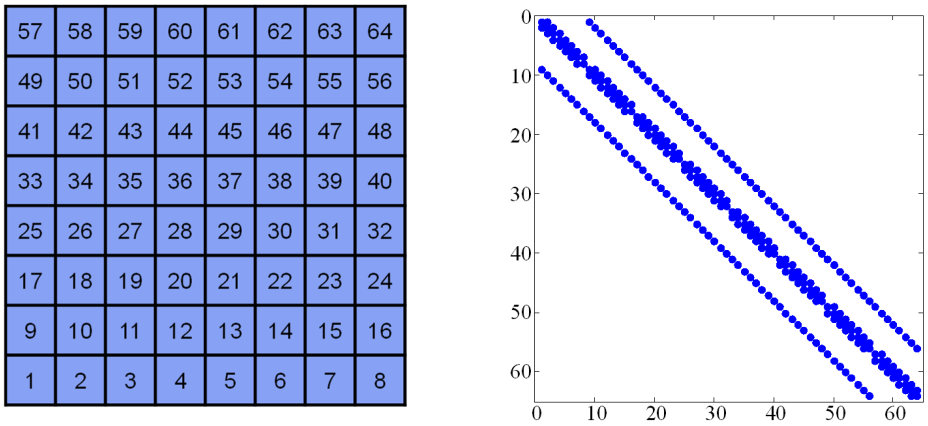

(a) Structured grid (64×64) (b) Corresponding coefficient matrix

Fig. 4.10—Sparsity of structured grid showing a banded coefficient matrix.

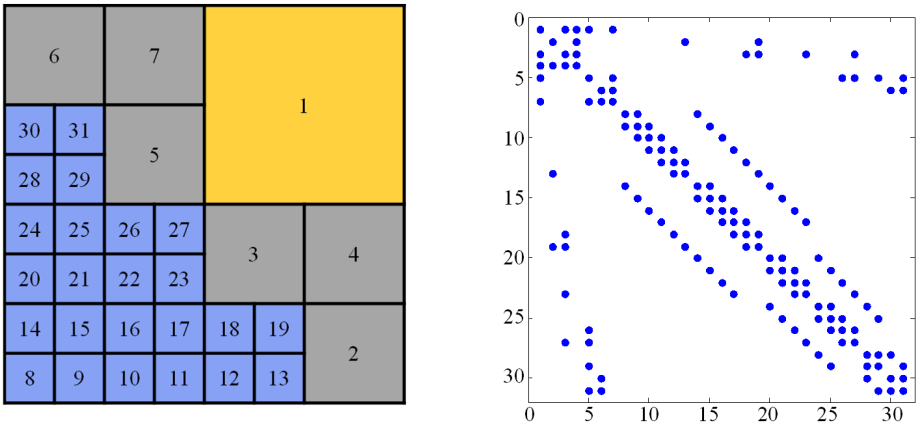

(a) Adaptive grid (31×31) (b) Corresponding coefficient matrix

Fig. 4.11—Sparsity of adaptive unstructured grid showing a non-banded coefficient matrix.

4.4.2 Transfer of properties

While creating a new adaptive grid, it is necessary to transfer the static and dynamic properties in two different occasions:

- From adaptive grid to fine grid. This information is used to calculate the flux distribution for a single time-step prior to forecasting the compositional front.
- From fine grid to adaptive grid. Once the new grid has been created and numbered, the fine-grid solution is transferred to the new adaptive grid to continue the simulation run.

Due the explicit nature of the flow calculations, we only need to transfer two dynamic properties: pressure and number of moles. Once the dynamic properties are calculated for the new grid, a flash calculation would determine the phase behavior and fluid properties for every cell.

Dynamic properties: from adaptive to fine

The flow solution obtained in the adaptive grid is transferred to a fine-grid. The number of moles in an coarse cell is distributed in the fine model using a pore volume-weighted average. For a single fine cell (Eq. 4.29).

$$n_i^{fine} = \frac{n_i^{coarse} V_p^{fine}}{V_p^{coarse}} \tag{4.29}$$

where:

n_i Number of moles of component i

V_p Pore volume

On the other hand, pressures in the fine cell take the value of their corresponding coarse parent cell as shown in **Fig.4.12**.

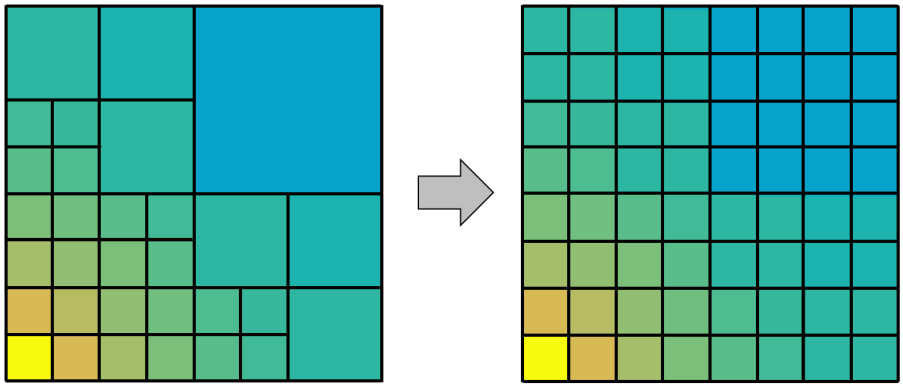

Fig. 4.12—Transfer of pressure from an adaptive grid to a fine grid.

Dynamic properties: from fine to adaptive

When the new adaptive grid is created, the fine-level solution obtained with finite difference is transferred to the adaptive grid. Moles of each component are transferred to the coarse cell by simply adding the moles of the fine cells that it encompasses (Eq. 4.30).

$$n_i^{coarse} = \sum_{i=1}^{N} \left(n_i^{fine} \right) \tag{4.30}$$

Pressures of the coarse are calculated using a pore volume weighted-average calculated using Eq. 4.31 and illustrated in **Fig.4.13**.

$$\overline{p}^{coarse} = \frac{\sum_{i=1}^{N} \left(p V_p^{fine} \right)}{\sum_{i=1}^{N} \left(V_p^{fine} \right)} \tag{4.31}$$

where:

p Pressure

V_p Pore volume

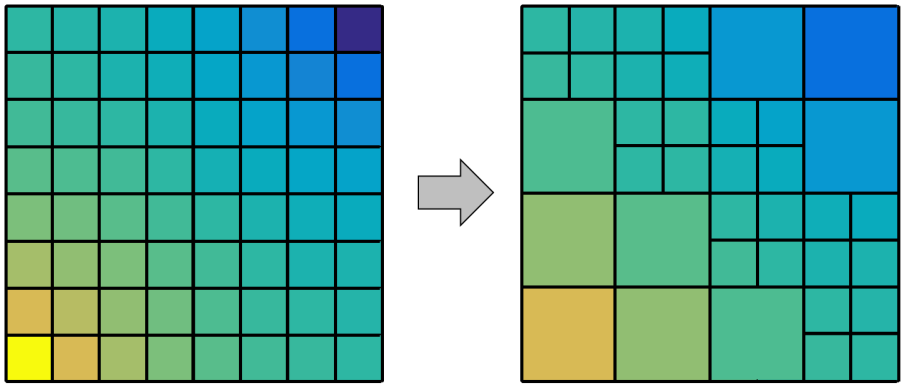

Fig. 4.13—Transfer of pressure from a fine grid to an adaptive grid.

Static properties

Static properties are only required to be transferred from the fine grid to the adaptive one. For volumetric properties, such as the porosity, the effective value of a coarse cell is simply the pore volume weighted average as shown in Eq. 4.32.

$$\phi^{coarse} = \frac{\sum_{i=1}^{N} \left(\phi^{fine} V_b^{fine} \right)}{\sum_{i=1}^{N} \left(V_b^{fine} \right)} \tag{4.32}$$

where:

ϕ Porosity

V_p Pore volume

For intrinsic properties, such as the permeability, transferring from a fine cell into a coarse one presents significant challenges. There are many techniques that have been developed to represent the flow of a fine grid using coarser cells (King and Mansfield 1999, Durlofsky 2003). For this work, we have implemented a simple upscaling technique to estimate the vertical and horizontal permeability of a coarse cell. Permeabilities are calculated with arithmetic average for the horizontal direction and harmonic average for the vertical

direction as shown in Eq. 4.33 and Eq. 4.34 respectively. It is important to consider that the calculation of average permeabilities in this work require further investigation in order to improve upscaling techniques.

$$k_h^{coarse} = \frac{\sum_{i=1}^{N} (k_{h_i} h_i)}{\sum_{i=1}^{N} (h_i)} \tag{4.33}$$

$$k_v^{coarse} = \frac{\sum_{i=1}^{N} \left(h^{fine}\right)}{\sum_{i=1}^{N} \left(\frac{h^{fine}}{k_v^{fine}}\right)} \tag{4.34}$$

where:

- k_h Horizontal permeability
- k_v Vertical permeability
- h Cell height

4.5 Re-gridding frequency

One key factor to consider is the computational expense associated with updating the grid. Creating an adaptive grid in each time step has proved to be impractical, and it provides only limited computational advantages over using a static fine grid model. Using the streamline time-of-flight concept along with the CDE enables us to calculate the time it would take the injection front to move a specified distance. To implement this procedure, the user defines the maximum movement of the injection front allowed before requiring a new grid. This approach reduces the computational requirement related to continuously updating the simulation grid while accounting for changes in flow velocity throughout the simulation run.

CHAPTER V
RESULTS AND ANALYSIS OF SIMULATION CASES

This chapter presents the study of multiple simulation cases aimed to evaluate the performance of the new adaptive mesh refinement algorithm. The analyses include different models undergoing continuous CO_2 injection in a quarter of a 5-spot pattern. First, 2-dimensional models assess the feasibility of the dynamic technique by considering homogeneous and heterogeneous reservoirs producing above the bubble point pressure. Then, 3-dimensional models test the versatility of the methodology by examining complex production scenarios, including the injection of CO_2 in reservoirs with pressures below the bubble point.

For all cases, a fine grid model (best representation of simulation forecast) served as base of comparison against the adaptive mesh refinement and coarsening algorithm. The accuracy of the solution is evaluated using oil production, gas injection, and average reservoir pressure at the breakthrough time. The computational performance is assessed by comparing the time required to run an adaptive model with reference to a static fine one.

Results show improved computational performance using adaptive grids while having similar forecasts for production and pressure compared to fine models. The studies were carried out in a personal computer with Intel Xeon with 10 CPU processor @ 3.70 GHz, 3701 Mhz, 32 GB memory, and Windows 7 64-bits PC. The running time was calculated using a high-resolution counter that records the tick counts before and after executing the program and the tick frequency (ticks/sec).

5.1 2D simulations

The performance of the adaptive mesh refinement method is first explored by evaluating the algorithm using 2-dimensional models for a homogeneous and a heterogeneous reservoir. Both cases simulate the injection of CO_2 in an inverted 5-spot well configuration, commonly used for enhanced oil recovery processes. Due the symmetric features of the injection arrangement, we only modeled 1/4$^{\text{th}}$ of the pattern. We used the fluid properties listed in Table 3.24 (Chapter III, section 3.4) that represent a 28.1 °API oil described with five pseudo-components. The in-situ fluid has a miscibility pressure of 5,558 psia at 200 °F when injecting CO_2 into the system, as determined numerically using a first-contact miscibility experiment.

5.1.1 Homogeneous model

The homogeneous reservoir model represents a 5-spot pattern with an areal extension of 60 acres. Only 15 acres are modeled, corresponding to a 1/4$^{\text{th}}$ of the pattern as displayed in the grey area of **Fig. 5.1**.

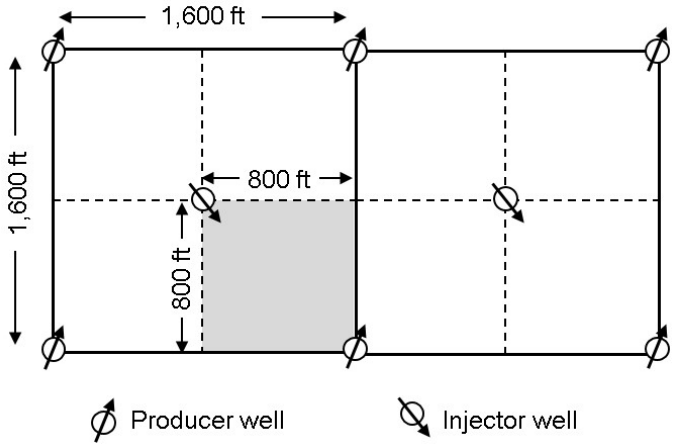

Fig. 5.1—5-spot injection pattern showing in grey the area selected for modeling in the 2D homogeneous model.

The 2D fine grid has a maximum of 6,400 cells ($n_{x,max}$=80, $n_{y,max}$=80, and $n_{z,max}$=1) as shown in **Fig. 5.2**, where each gridcell measures 10 ft by 10 ft by 70 ft. Cells can be grouped using three hierarchical levels in the horizontal direction ($2^3 \times 2^3 = 8 \times 8$) for a maximum cell dimension of 80 ft by 80 ft by 70 ft. **Fig. 5.2** summarizes the grid input parameters.

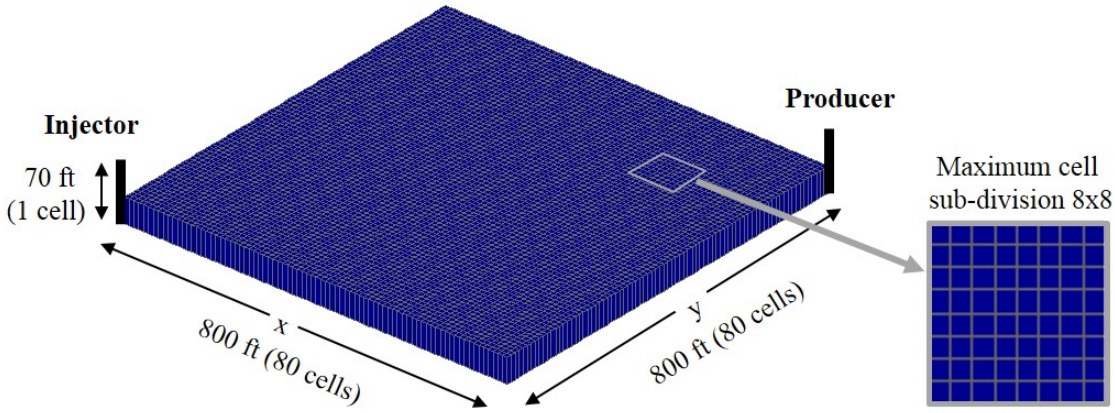

Fig. 5.2—2D model used to evaluate the homogeneous reservoir with an areal extension of 15 acres and thickness of 70 ft. Fine cells can be grouped into coarser cells up to a maximum of $8 \times 8 \times 1$.

Table 5.1—Input grid parameters used in the 2D homogeneous model

Property	**Value**
Length, ft	800
Width, ft	800
Thickness, ft	70
Grid size in x-direction (finest), ft	10
Grid size in y-direction (finest), ft	10
Grid size in x-direction (coarsest), ft	80
Grid size in y-direction (coarsest), ft	80

Reservoir properties

The structure of the reservoir has a constant depth of 12,540 feet. Initial pressure is 6,500 psia, constant reservoir temperature is 200 °F, and no in-situ water. The rock has a porosity of 20% and isotropic horizontal permeability of 120 mD. **Table 5.2** shows a summary of the reservoir properties used to evaluate the homogeneous model.

Table 5.2—Rock properties and initial conditions used in the 2D homogeneous simulation model

Property	**Value**
Pressure, psia	6,500
Temperature, °F	200
Top depth, ft	12,540
Porosity, fraction	0.2
Horizontal permeability, mD	120
Reference pressure, psia	5,868
Rock compressibility, 1/psia	4×10^{-6}

Operating conditions

The simulation model has two active wells, a producer and an injector, located in opposite corners of the arrangement as shown in Fig. 5.2. Both wells have a wellbore radius of 0.3 feet and no skin. The producer well was set at a constant bottomhole flowing pressure of 6,000 psia, maintaining the system above the minimum miscibility pressure. The injector well injects CO_2 at constant bottomhole flowing pressure of 7,000 psia. **Table 5.3** lists the operating conditions used in the model.

Table 5.3—Operating conditions used in the 2D homogeneous model

Property	**Value**
Producer bottomhole flowing pressure, psia	6,000
Injector bottomhole flowing pressure, psia	7,000

Triggering conditions

The homogeneity criteria tracks compositional variations of CO_2 in the model, set to a maximum of 1% difference in CO_2 composition among children cells. The re-gridding frequency was set for a maximum of 60 ft of advancement of the front (length of three grid blocks).

$$z_{CO_2}^{max} - z_{CO_2}^{min} < 0.01 \tag{5.1}$$

Performance comparison

Figs. 5.3 and **5.4** show the distribution of CO_2 composition and pressure in the reservoir at different times (30, 150, 350, 600, 800, and 1,500 days). During the adaptive mesh refinement process, cells were dynamically discretized to capture the location of the gas injection front. This resulted in fine cells along the injection front but coarser cells in regions far from the front. This example shows the potential of the adaptive technique as 26 grid realizations allowed reducing the total number of cells from 6,400 to models ranging from 292 to 2,608 depending on the location of the front. Reduction in the number of cells in the model results in the adaptive model running 1.4 times faster compared to the fine grid. This represents a 30% improvement in the CPU time compared to the fine model as calculated using Eq. 5.2. **Table 5.4** presents a summary of the CPU ratio and reduction percentage for the 2D homogeneous case.

$$\%\text{CPU}_{reduction} = 100\left(\frac{\text{CPU}_{fine} - \text{CPU}_{adaptive}}{\text{CPU}_{fine}}\right) \tag{5.2}$$

Table 5.4—Comparison of computational performance for the homogeneous 2D model

Grid	**Number of cells**	**CPU execution ratio (fine/ adaptive)**	**% CPU reduction**
Fine	6,400	–	–
Adaptive	292-2,608	1.41	30

Figs. 5.5 and **5.6** show the results of oil production and gas injection rate. Three cases are displayed in the figures: 1) fine grid ($80 \times 80 \times 1$ with 6,400 cells), coarse grid ($40 \times 40 \times \times 1$ with 1,600 cells), and an adaptive grid (variable number of cells ranging from 292 to 2,608). Results show a 3.02% difference in cumulative oil production between the fine and the adaptive grid after 1,500 days of production and injection modeling (breakthrough time). On the other hand, using a coarser grid ($40 \times 40 \times \times 1$) resulted in 9.01% difference in the cumulative oil production. Similarly, cumulative gas injection showed 3.048% difference using the adaptive grid while the coarse grid showed 10.97% error.

The produced gas-oil (GOR) also shows a good match between the fine and the adaptive model (**Fig. 5.7**). On the contrary, the GOR in the coarse model begins deviating from the fine model at approximately 1,000 days. This is evidence of an early breakthrough, a consequence of the higher injection rates observed in Fig. 5.6. A similar response is observed in the average reservoir pressure (**Fig. 5.8**). The adaptive model shows a similar behavior compared to the fine grid, while the coarse model deviates after the CO_2 breakthrough. **Table 5.5** summaries the production and pressure errors as compared to the fine solution at breakthrough time (1,500 days).

Table 5.5—Errors at breakthrough time (1,500 days) of the adaptive and coarse grid compared to the fine model in a homogeneous 2D model

Grid	**% Error in cumulative oil production (STB)**	**% Error in cumulative gas injection (Mscf)**	**% Error in pressure (psia)**
Coarse	9.01	10.97	0.0534
Adaptive	3.02	3.048	0.0075

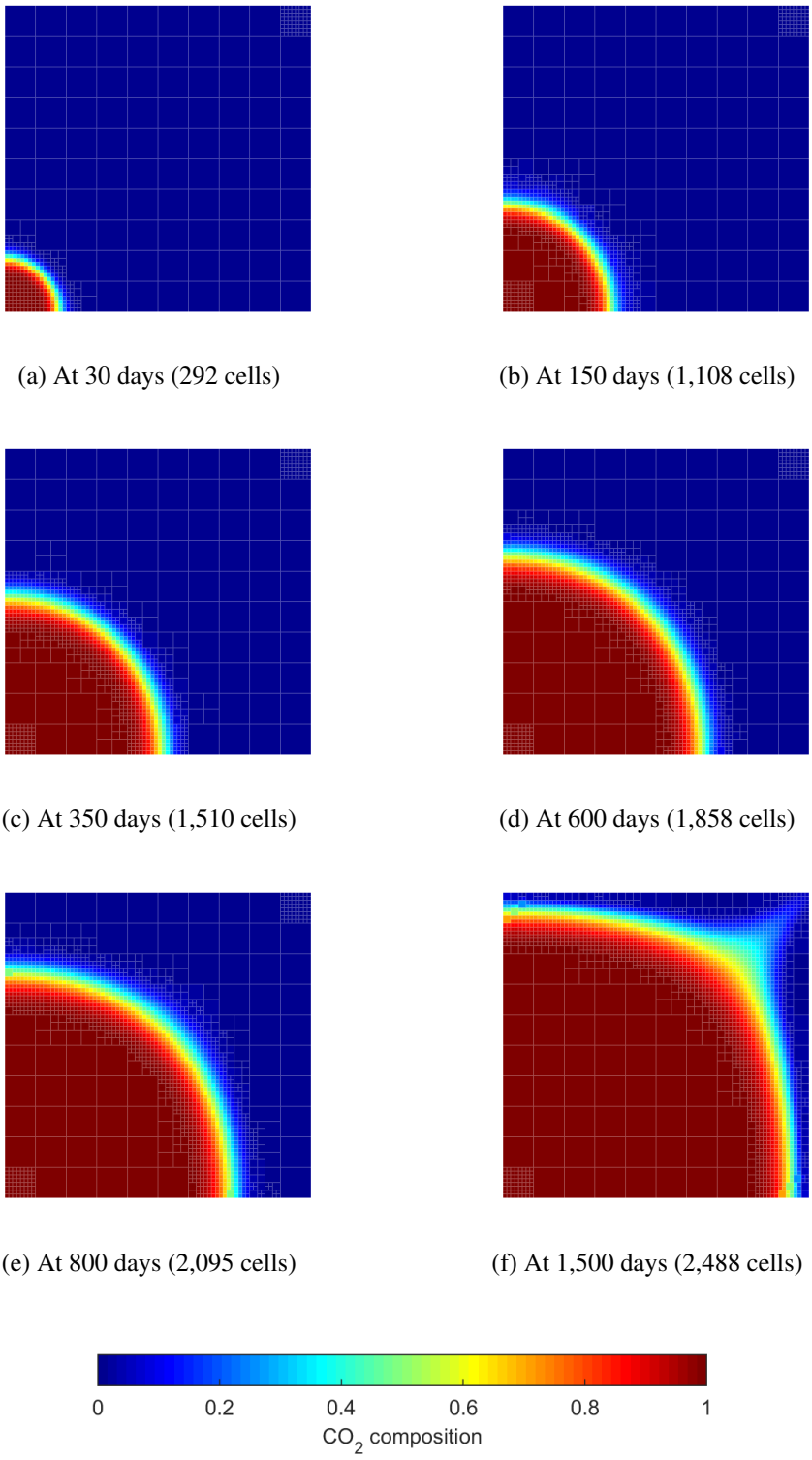

(a) At 30 days (292 cells)

(b) At 150 days (1,108 cells)

(c) At 350 days (1,510 cells)

(d) At 600 days (1,858 cells)

(e) At 800 days (2,095 cells)

(f) At 1,500 days (2,488 cells)

Fig. 5.3—Top-view of composition distribution at 30, 150, 350, 600, 800, and 1,500 days of simulation using an adaptive grid in the 2D homogeneous model.

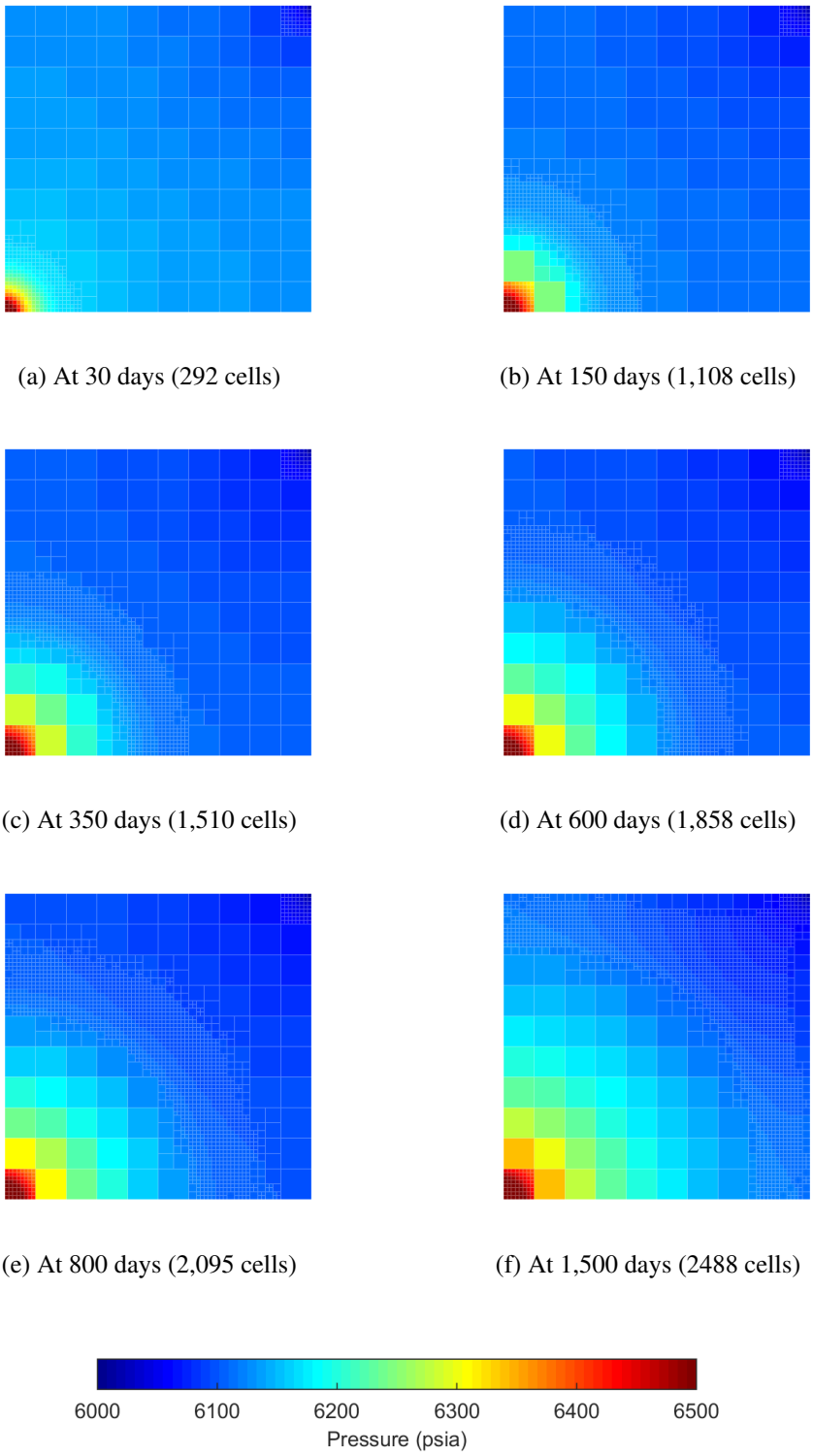

(a) At 30 days (292 cells)

(b) At 150 days (1,108 cells)

(c) At 350 days (1,510 cells)

(d) At 600 days (1,858 cells)

(e) At 800 days (2,095 cells)

(f) At 1,500 days (2488 cells)

Fig. 5.4—Top-view of reservoir pressure distribution at 30, 150, 350, 600, 800, and 1,500 days of simulation using an adaptive grid in the 2D homogeneous model.

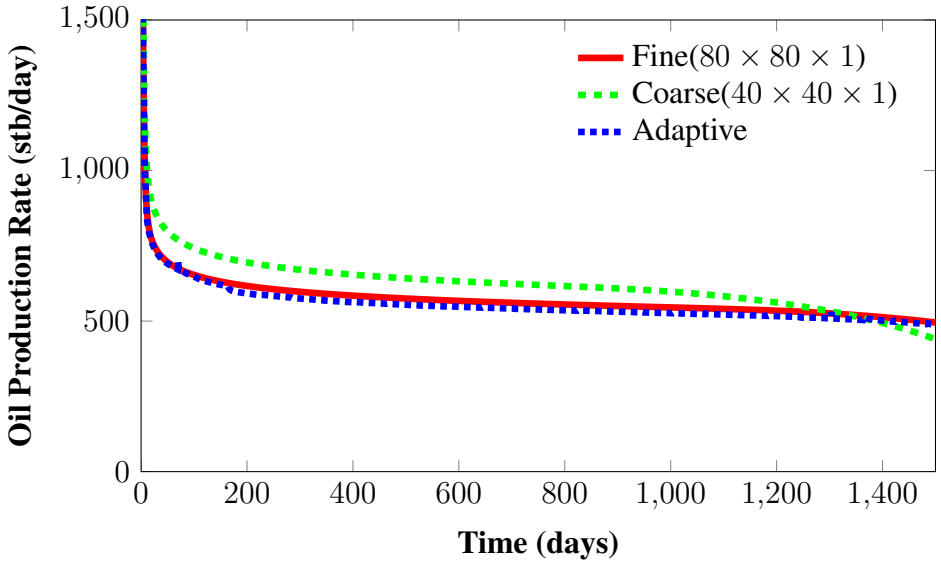

Fig. 5.5—Oil production rate after 1,500 days for a 2D homogeneous reservoir modeled using three grid descriptions: fine ($80 \times 80 \times 1$), coarse ($40 \times 40 \times 1$), and adaptive.

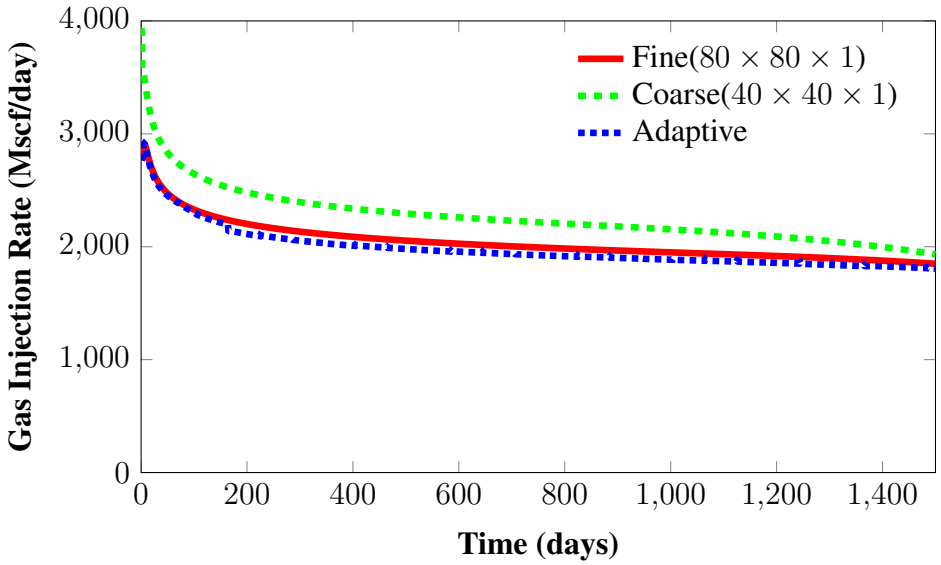

Fig. 5.6—Gas injection rate after 1,500 days for a 2D homogeneous reservoir modeled using three grid descriptions: fine ($80 \times 80 \times 1$), coarse ($40 \times 40 \times 1$), and adaptive.

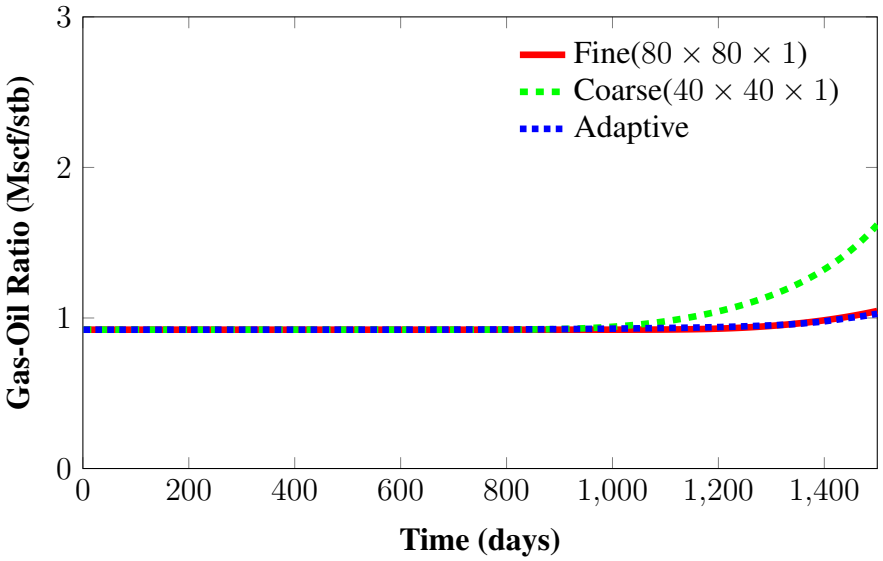

Fig. 5.7—Produced gas-oil ratio after 1,500 days for a 2D homogeneous reservoir modeled using three grid descriptions: fine (80 × 80 × 1), coarse (40 × 40 × 1), and adaptive.

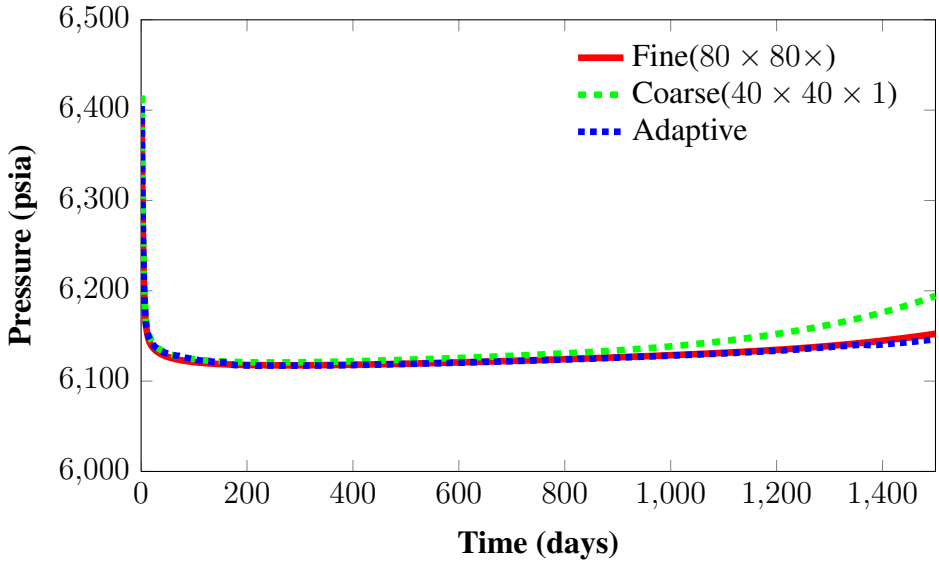

Fig. 5.8—Average reservoir pressure after 1,500 days for a 2D homogeneous reservoir modeled using three grid descriptions: fine (80 × 80 × 1), coarse (40 × 40 × 1), and adaptive.

5.1.2 Heterogeneous reservoir

The heterogeneous reservoir model is represented by layer 17 of the Tenth SPE Comparative Solution Project (Christie and Blunt, 2001). The original objective of the benchmark study was to compare performance and upscaling techniques from different simulators. For this work, the reservoir properties of the case study are used to evaluate the effect of heterogeneities in the application of adaptive mesh refinement using quadtree decomposition.

The geological description of the comparative study is based on the Brent Group sequence in the North Sea. The selected layer 17 represents the Tarbert formation, a complex environment characterized by a prograding near shore deposition showing large variations in the distribution of porosity and permeability.

The simulation model is a 1/4$^{\text{th}}$ of a 5-spot pattern with 7.35 acres as shown in **Fig. 5.9**. It is discretized using a maximum of 1,600 cells ($n_{x,max}$=40, $n_{y,max}$=40, and $n_{z,max}$=1), where each gridcell measures 20 ft by 10 ft by 50 ft. Coarsening of cells is done with a maximum merging of $4 \times 4 \times 1$ fine cells (**Fig. 5.9**). **Table. 5.6** summarizes the grid input parameters.

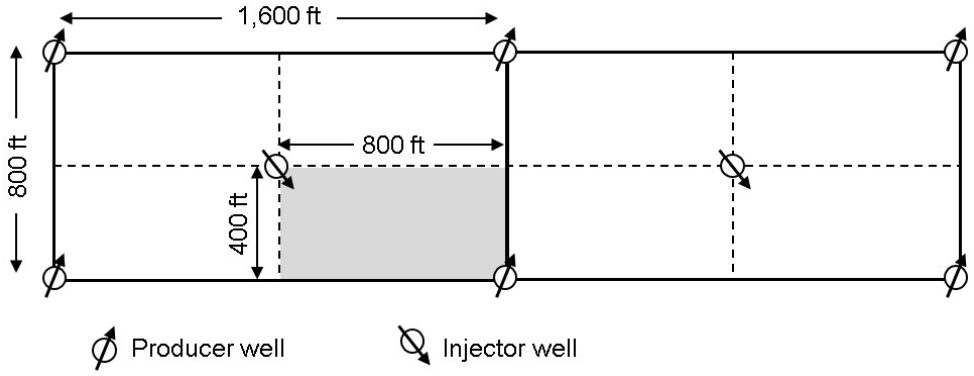

Fig. 5.9—5-spot injection pattern showing in grey the area selected for modeling in the 2D heterogeneous model.

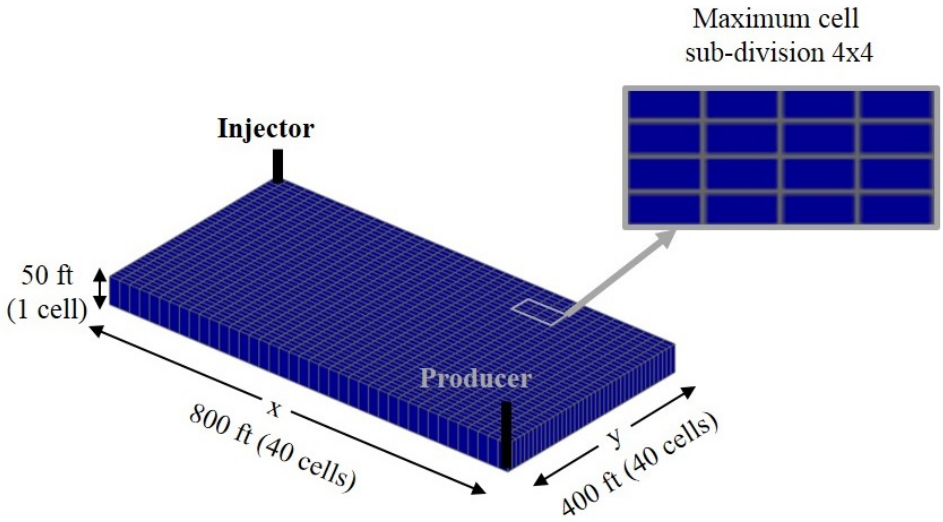

Fig. 5.10—2D model used to evaluate the heterogeneous reservoir with an areal extension of 7.35 acres and thickness of 50 ft. Fine cells can be grouped into coarser cells up to a maximum of $4 \times 4 \times 1$.

Table 5.6—Input grid parameters used in the 2D heterogeneous model

Property	**Value**
Length, ft	800
Width, ft	400
Thickness, ft	50
Grid size in x-direction (finest), ft	20
Grid size in y-direction (finest), ft	10
Grid size in x-direction (coarsest), ft	80
Grid size in y-direction (coarsest), ft	40

Reservoir properties

Similar to the homogeneous case, the structure has a constant depth of 12,540 feet. It has an initial pressure of 7,000 psia, initial temperature of 200 °F and no in-situ water. The selected reservoir sector has an average (geometric) horizontal permeability of 81.22 mD, ranging from 0.57 to 8,392 mD; and an average porosity of 25.3%. **Fig. 5.11** shows the porosity and permeability distribution while **Table 5.7** summarizes average rock and initial conditions.

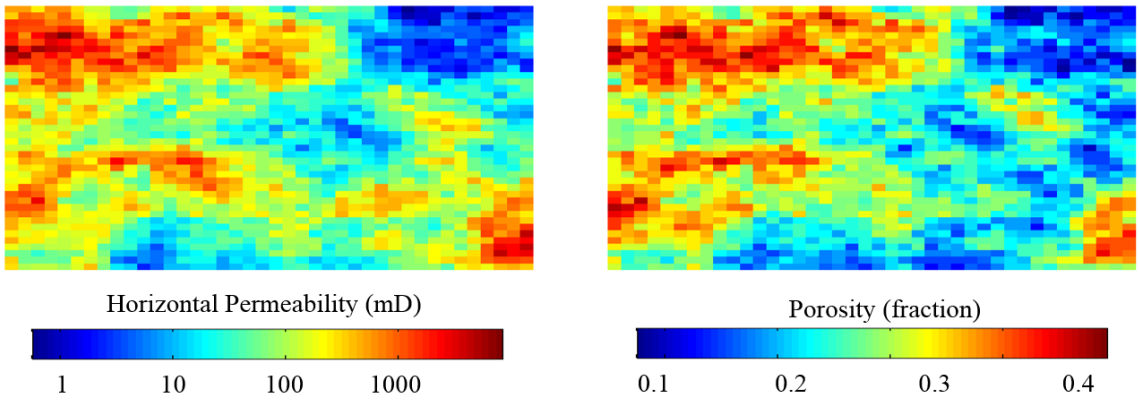

Fig. 5.11—Rock properties for layer 17 (used in this study) of the SPE Tenth Comparative Solution Project.

Table 5.7—Rock properties and initial conditions used in the 2D heterogeneous model (SPE Tenth Comparative Solution Project)

Property	**Value**
Pressure, psia	7,000
Temperature, °F	200
Top depth, ft	12,540
Porosity, fraction	0.253
Horizontal permeability, mD	81.22
Reference pressure, psia	5,868
Rock compressibility, 1/psia	4×10^{-6}

Operating conditions

Production and injection wells have the same specifications as those used in the homogeneous case, with wellbore radius of 0.3 feet and no skin. They are located in opposite side of the simulation model as shown in Fig. 5.9. Wells are controlled by fixed bototmhole flowing pressure, with 5,500 psia for the producer and 7,500 psia for the injector.

Table 5.8—Operating conditions used in the 2D heterogeneous model

Property	**Value**
Producer bottomhole flowing pressure, psia	5,500
Injector bottomhole flowing pressure, psia	7,500

Triggering criteria

In addition to the homogeneity criteria used in the homogeneous model, this case also incorporated a constraint to limit coarsening of cells that have high contrast in permeability. The re-gridding frequency was set for a maximum of 30 ft of advancement of the front (length of three grid blocks in the y-direction).

$$z_{CO_2}^{max} - z_{CO_2}^{min} < 0.01 \tag{5.3}$$

$$k_h^{min} > k_h^{max} \times 0.3 \tag{5.4}$$

Performance comparison

Unlike the homogeneous reservoir, where the injection front shows a smooth displacement, in highly heterogeneous systems the injection front is not symmetrical and follows the path of least resistance as illustrated by the streamlines in **Fig. 5.12**. Flow trajectory in heterogeneous reservoirs may be exhibit significant changes along the simulation run depending on fluid compressibility and operating conditions.

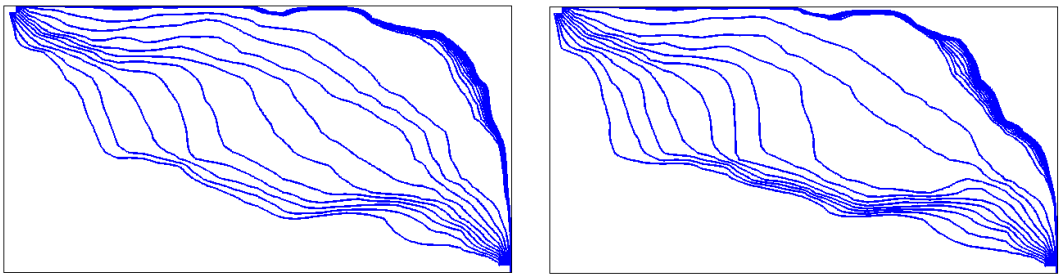

(a) At 500 days (b) At 1,500 days

Fig. 5.12—Streamlines at 500 and 1,500 days of simulation for the heterogeneous case study showing changes in the flow trajectory along the simulation run.

Figs. 5.13 and **5.14** show the advancement of the displacing fluid using adaptive mesh refinement at six different times (300, 500, 700, 1,000, 1,200, and 1,500 days). The dynamic algorithm adapts to the forecasted location and shape of the compositional front, account-

ing also for permeability contrast between cells, thus reducing dispersion and inaccurate reservoir behavior predictions. The simulation using the adaptive method resulted in 23 different grids realizations, varying from 967 to 1,258 cells. Reduction in the number of cells compared to the static fine grid (constant 1,600 cells) yielded a 30% improvement in the CPU time compared to the fine model as listed in **Table 5.9**.

Table 5.9—Comparison of computational performance for the heterogeneous 2D model

Grid	**Number of cells**	**CPU execution ratio (fine/ adaptive)**	**% CPU reduction**
Fine	1,600	–	–
Adaptive	967-1,258	1.42	29.7

Figs. 5.15 to **5.18** show oil production rate, gas injection rate, pressure forecast and produced gas-oil ratio. Four cases are displayed in the figures: fine grid ($40 \times 40 \times 1$ with 1,600 cells), adaptive using composition criteria, adaptive using composition and permeability criteria, and adaptive using only permeability as criteria. Results show that incorporating permeability resulted in less than 0.72% difference in cumulative oil production between the fine and the adaptive grid at the breakthrough time (1,400 days) while using only the compositional criteria resulted in a difference of 11.25%. Pressure response did not show a significant variation prior to the breakthrough when it began to deviate due the early breakthrough. Errors are summarized in **Table 5.10**.

Table 5.10—Errors at breakthrough time (1,400 days) of the adaptive and coarse grid compared to the fine model in in the 2D heterogeneous model

Grid	**% Error in cumulative oil production (STB)**	**% Error in cumulative gas injection (Mscf)**	**% Error in pressure (psia)**
Adaptive (comp)	11.25	11.91	0.33
Adaptive (comp + perm)	0.72	0.70	0.07

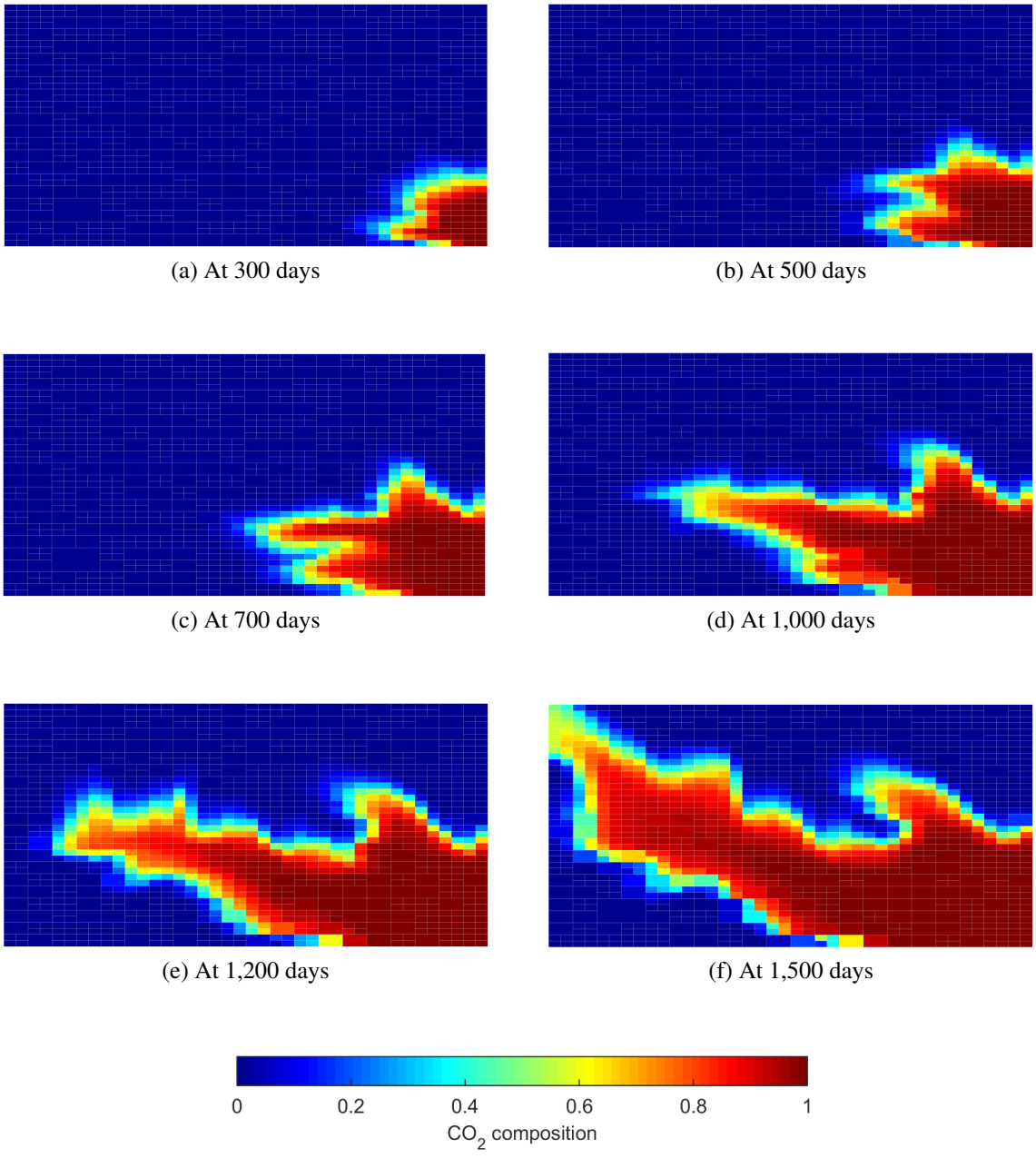

(a) At 300 days

(b) At 500 days

(c) At 700 days

(d) At 1,000 days

(e) At 1,200 days

(f) At 1,500 days

Fig. 5.13—Top-view of composition distribution at 300, 500, 700, 1,000, 1,200, and 1,500 days of simulation using an adaptive grid in the 2D heterogeneous model.

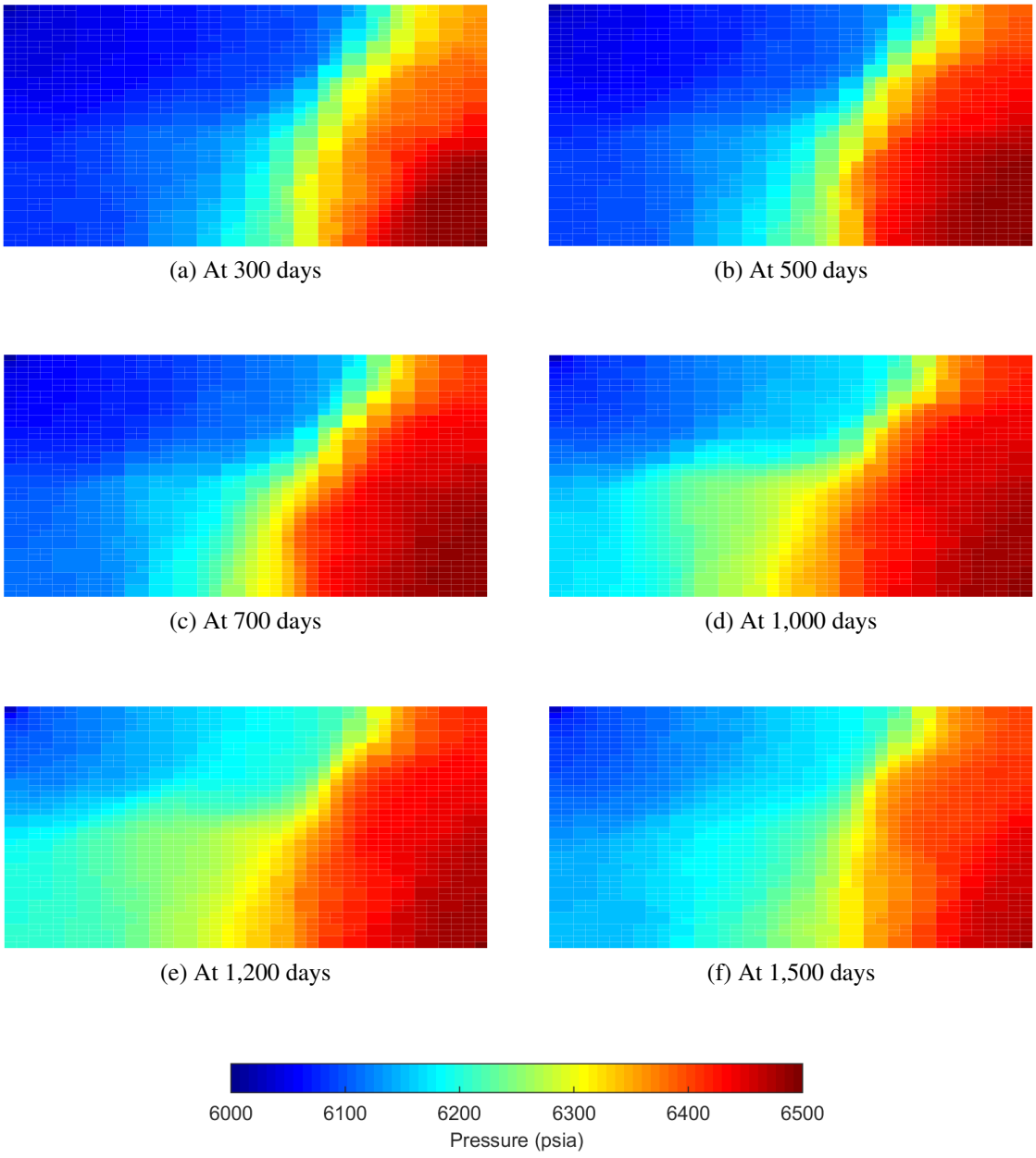

(a) At 300 days

(b) At 500 days

(c) At 700 days

(d) At 1,000 days

(e) At 1,200 days

(f) At 1,500 days

Fig. 5.14—Top-view of pressure distribution at 300, 500, 700, 1,000, 1,200, and 1,500 days of simulation using an adaptive grid in the 2D heterogeneous model.

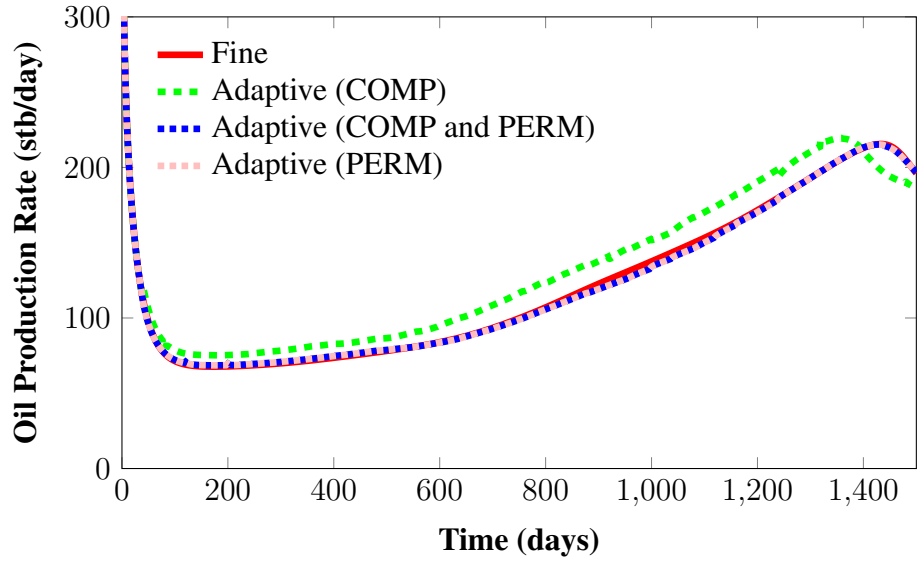

Fig. 5.15—Oil production rate after 1,500 days for the SPE 10 Case Study using three grid descriptions: fine ($40 \times 40 \times 1$), adaptive using composition criteria, and adaptive using composition and permeability criteria.

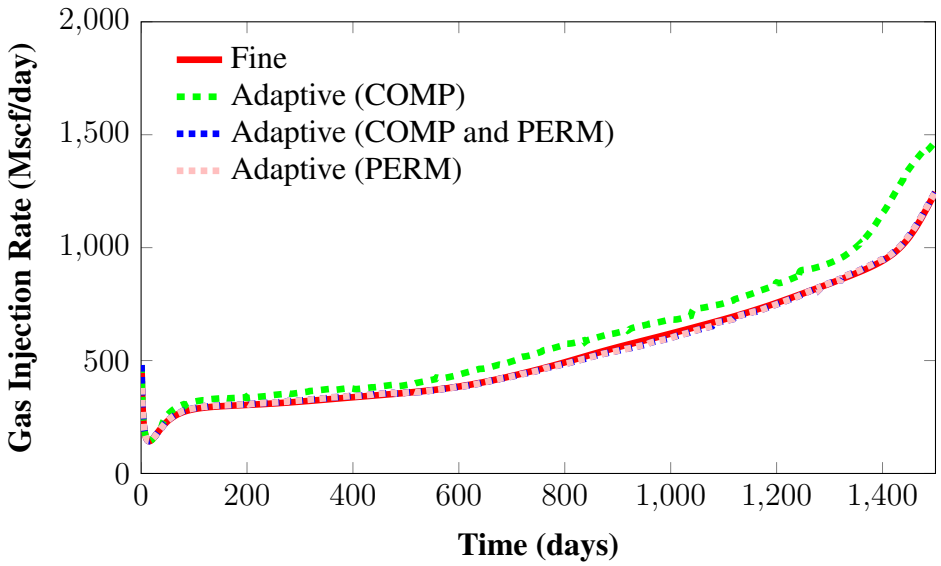

Fig. 5.16—Gas injection rate after 1,500 days for the SPE 10 Case Study using three grid descriptions: fine ($40 \times 40 \times 1$), adaptive using composition criteria, and adaptive using composition and permeability criteria.

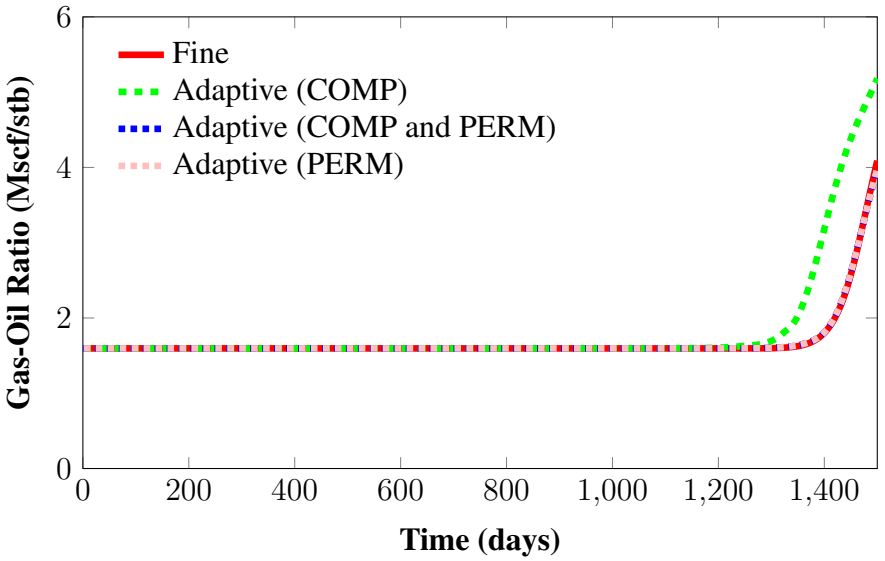

Fig. 5.17—Produced gas-oil ratio after 1,500 days for the SPE 10 Case Study using three grid descriptions: fine ($40 \times 40 \times 1$), adaptive using composition criteria, and adaptive using composition and permeability criteria.

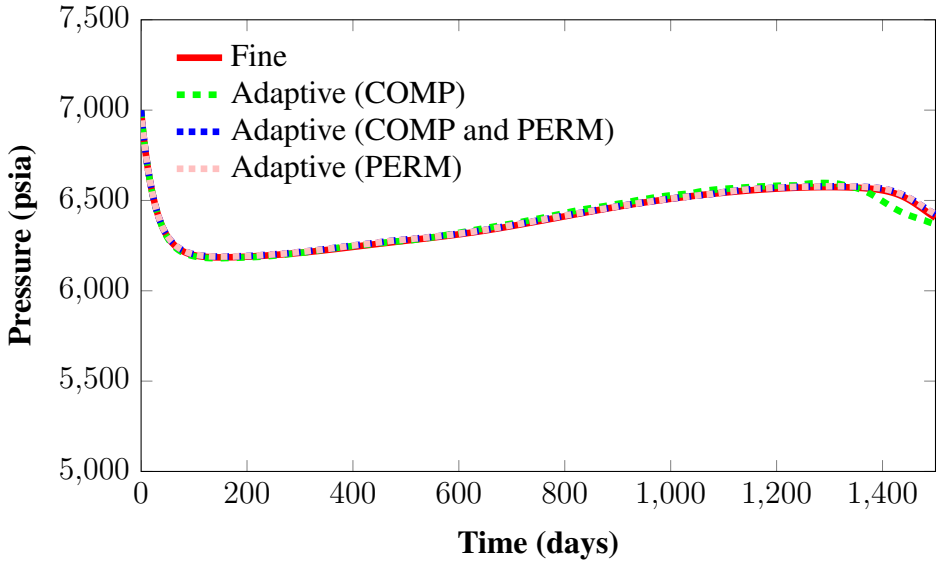

Fig. 5.18—Average reservoir pressure (volume-weighted) after 1,500 days for the SPE 10 Case Study using three grid descriptions: fine ($40 \times 40 \times 1$), adaptive using composition criteria, and adaptive using composition and permeability criteria.

5.2 3D simulations

The flexibility of the adaptive mesh refinement algorithm is evaluated in 3-dimensions by assessing the behavior of a homogeneous reservoir under different operating conditions. All cases represent the 1/4$^{\text{th}}$ of a 5-spot pattern described in section 5.1.1 and illustrated in Fig. 5.1. The reservoir has a porosity of 20%, isotropic horizontal permeability of 120 mD, and vertical to horizontal permeability ratio of 0.1. **Table 5.11** shows a summary of the reservoir properties used to evaluate the 3D models.

Table 5.11—Rock properties and initial conditions used in the 3D homogeneous simulation model

Property	**Value**
Temperature, °F	200
Top depth, ft	12,540
Porosity, fraction	0.2
Horizontal permeability, mD	120
Permeability ratio (k_v/k_h)	0.1
Reference pressure, psia	5,868
Rock compressibility, 1/psia	4×10^{-6}

Triggering conditions

The homogeneity criteria was defined based on the compositional variation of CO_2 in the model, allowing for a maximum variation of 1% in the sub-cells analyses.

$$z_{CO_2}^{max} - z_{CO_2}^{min} < 0.01 \tag{5.5}$$

The time frequency to create a new adaptive grid was set to allow for a maximum displacement of the injection front corresponding to the distance of three gridblocks. For cases with two phases (oil and gas) flowing simultaneously, the evaluation of the displacement front is done in each phase independently, considering the most rapid phase for limiting the re-gridding frequency.

Cases evaluated and operating conditions

Three difference production scenarios were evaluated using the 3D models to test the algorithm using more complex reservoir conditions. We examined the following cases:

1. Reservoir pressure above miscibility.
2. Reservoir pressure below miscibility.
    - Reservoir initialized in single-phase with the producer's bottomhole flowing pressure below the bubble point.
    - Reservoir initialized in two-phases.

First, we explored the methodology in a homogeneous model producing and injecting above the bubble point and the minimum miscibility pressure. For this case, the reservoir conditions will remain in single-phase throughout the entire simulation run.

We then evaluated the performance of the adaptive technique when modeling reservoirs producing below the bubble point pressure. The two cases analyzed present unique challenges to the methodology. In the first case, the reservoir is initialized in a single-phase but falls below the saturation point as production begins in the model. Tracing the flow trajectory then starts in the injector well in a single-phase region, but eventually reaches a two-phase region as it reaches the producer well. The second case is initialized in two-phases, resulting in transport of CO_2 in both the liquid and gas phase.

All the reservoir models evaluated had two active wells, a producer and an injector, located in opposite corners of the model. Both wells have a radius of 0.3 feet and no skin. The specific production constraints for each case are listed in the following sub-sections.

5.2.1 Single-phase homogeneous model

The reservoir is represented by a 3D model with a maximum of 12,800 cells ($n_{x,max}$=40, $n_{y,max}$=40, and $n_{z,max}$=8), where each gridcell measures 20 ft by 20 ft by 8.75 ft. Cells can be grouped using two hierarchical levels for a maximum cell dimension of 80 ft by 80 ft by 35 ft (**Fig. 5.19**). **Table 5.12** summarizes the grid input parameters.

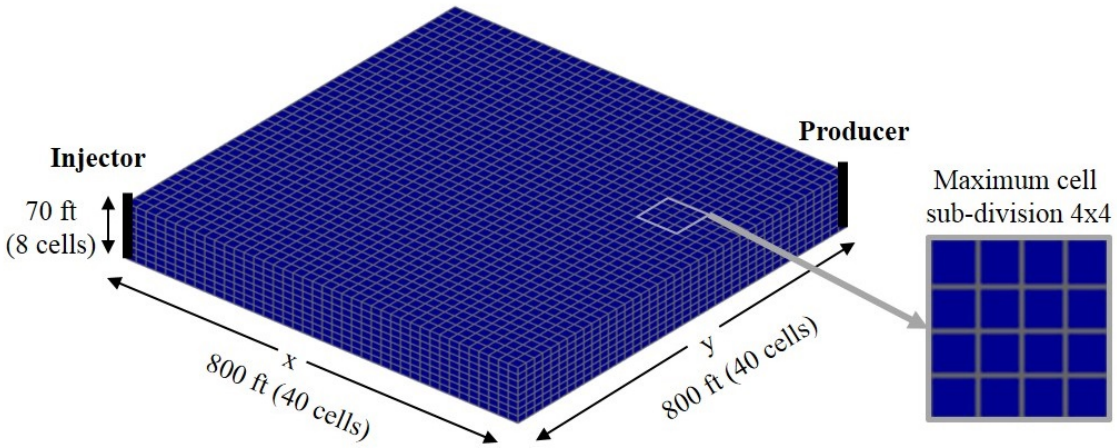

Fig. 5.19—3D model used to evaluate the single-phase homogeneous reservoir with an areal extension of 15 acres and thickness of 70 ft. Fine cells can be grouped into coarser cells up to a maximum of $4 \times 4 \times 4$.

Table 5.12—Input grid parameters used in the 3D single-phase and homogeneous simulation model

Property	Value
Length, ft	800
Width, ft	800
Thickness, ft	70
Grid size in x-direction (finest), ft	20
Grid size in y-direction (finest), ft	20
Grid size in z-direction (finest), ft	8.75
Grid size in x-direction (coarsest), ft	80
Grid size in y-direction (coarsest), ft	80
Grid size in z-direction (coarsest), ft	35

The reservoir was initialized with a constant pressure of 6,500 psia and initial temperature of 200 °F. The producer well was set at a constant bottomhole flowing pressure of 6,000 psia, maintaining the entire system above the minimum miscibility pressure. The injector well was set at constant bottomhole flowing pressure of 7,000 psia. **Table 5.13** lists the initial and operating conditions of the case.

Table 5.13—Initial and operating conditions in the 3D single-phase homogeneous model

Property	Value
Initial pressure, psia	6,500
Producer bottomhole flowing pressure, psia	6,000
Injector bottomhole flowing pressure, psia	7,000

Performance comparison

Figs. 5.20 and **5.21** show the spatial discretization at different times in the simulation study (60, 120, 400, 600, 800 and 1,200 days). Cells are refined in the three dimensions based on the distribution of compositions at a given time, resulting in fine gridding along the injection front but coarser cells anywhere else in the model. The total number of cells was significantly reduced, from 12,800 cells required for a static fine grid to 18 different grids varying from 746 to 6,318 cells. As a result, the adaptive grid was 2.74 times faster than the static grid, representing 63.4% reduction in CPU. **Table 5.14** presents a summary of the CPU ratio and reduction percentage for this case.

Table 5.14—Comparison of computational performance for a 3D single-phase homogeneous model

Grid	Number of cells	CPU execution ratio (fine/ adaptive)	% CPU reduction
Fine	12,800	–	–
Adaptive	746-6,318	2.74	63.4

Figs. 5.22 and **5.23** display the results from oil production and gas injection rate. Plots illustrate three cases: 1) fine grid ($40\times40\times8$ with 12,800 cells), coarse grid ($20\times40\times4$ with 1,600 cells), and an adaptive grid (variable number of cells ranging from 746 to 6,318). Results show only a 3.6% difference in cumulative oil production between the fine and the adaptive grid after 1,200 days of production and injection modeling (breakthrough time). On the other hand, using a coarser grid resulted in 10.7% difference in the cumulative oil production. Similarly, the gas injection rate using the adaptive model showed 3.71% error compared to the fine model, while the coarse grid resulted in 13.09% difference.

The over-prediction of oil rate and gas injection rate resulted in an early forecast for gas breakthrough time in the coarse grid. This is observed in the produced gas-oil ratio in **Fig. 5.24**, where it is possible to see that the coarse grid starts to increments at approximately 800 days while the fine and adaptive continue relatively constant until 1,200 days. Pressure response showed less sensitivity to grid-size before breakthrough, but it shows large deviations after that point as shown in **Fig. 5.45**. **Table 5.15** summarizes the production and pressure errors.

Table 5.15—Errors at breakthrough time (1,200 days) of adaptive and coarse grids compared to a fine 3D single-phase homogeneous model

Grid	**% Error in cumulative oil production (STB)**	**% Error in cumulative gas injection (Mscf)**	**% Error in pressure (psia)**
Coarse	10.69	13.09	0.68
Adaptive	3.64	3.71	0.07

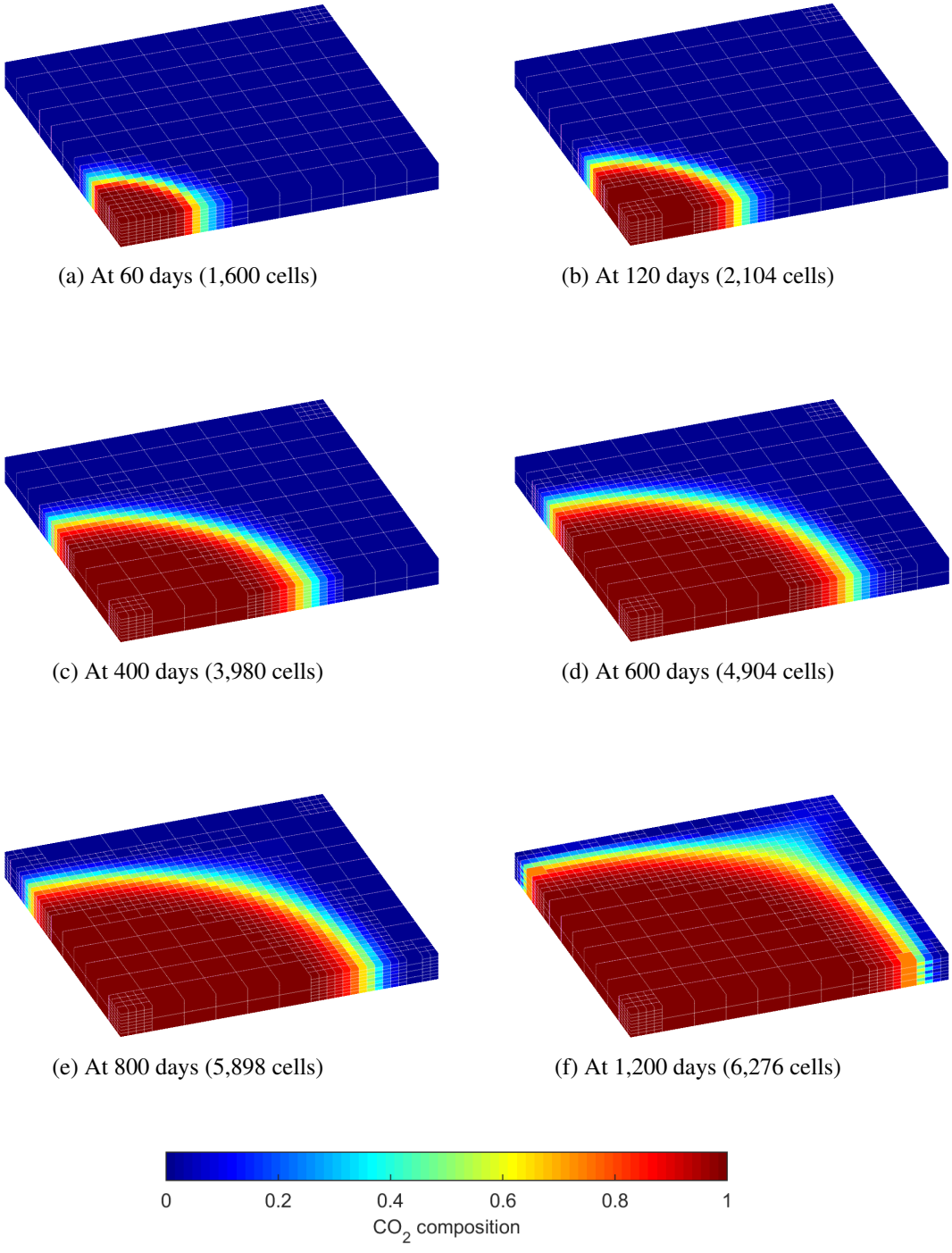

(a) At 60 days (1,600 cells)

(b) At 120 days (2,104 cells)

(c) At 400 days (3,980 cells)

(d) At 600 days (4,904 cells)

(e) At 800 days (5,898 cells)

(f) At 1,200 days (6,276 cells)

Fig. 5.20—Composition distribution at 60, 120, 400, 600, 800, and 1,200 days of simulation using an adaptive grid for 3D single-phase homogeneous model.

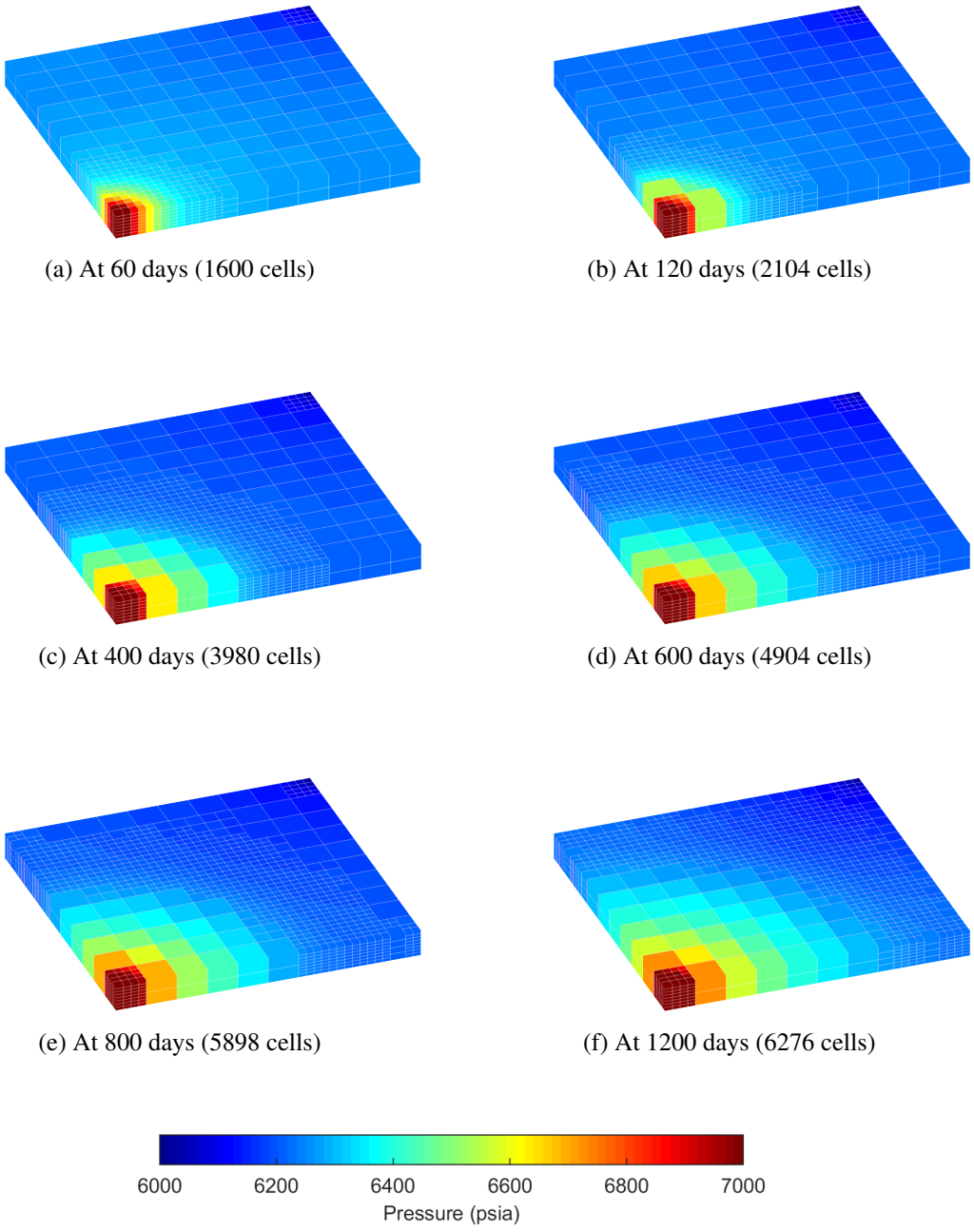

(a) At 60 days (1600 cells)

(b) At 120 days (2104 cells)

(c) At 400 days (3980 cells)

(d) At 600 days (4904 cells)

(e) At 800 days (5898 cells)

(f) At 1200 days (6276 cells)

Fig. 5.21—Pressure distribution at 60, 120, 400, 600, 800, and 1,200 days using an adaptive grid for the 3D single-phase homogeneous model.

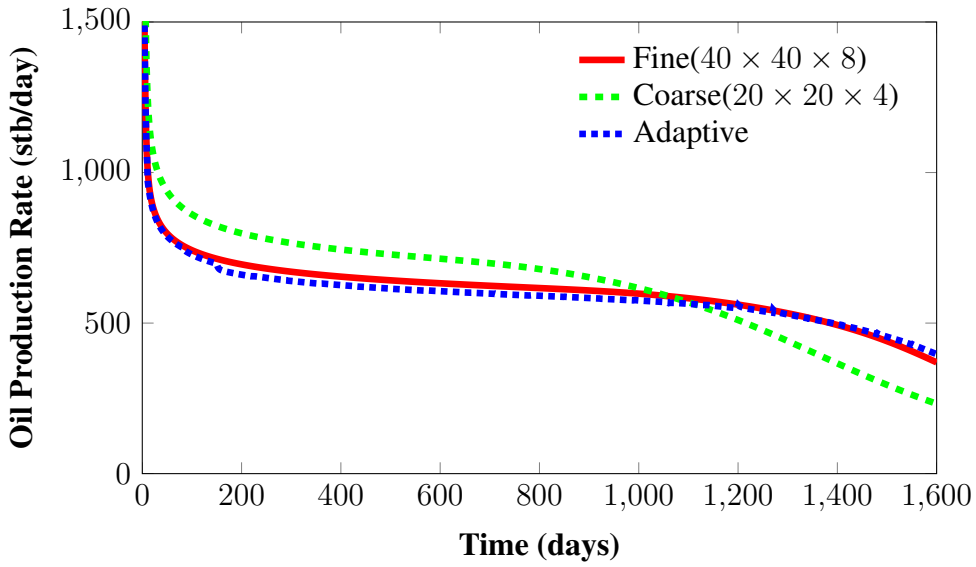

Fig. 5.22—Oil production rate after 1,600 days for a 3D single-phase homogeneous reservoir modeled using three grid descriptions: fine ($40 \times 40 \times 8$), coarse ($20 \times 20 \times 4$), and adaptive.

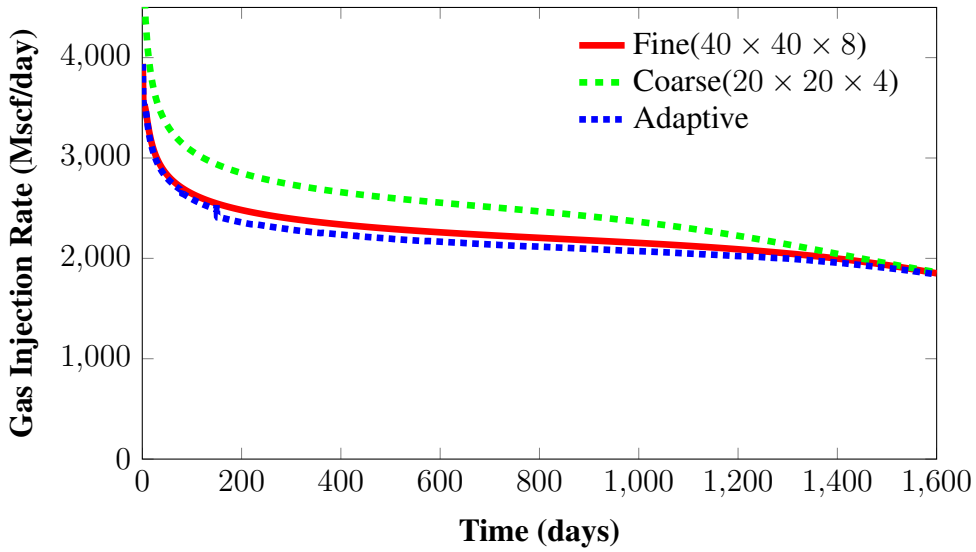

Fig. 5.23—Gas injection rate after 1,600 days for a 3D single-phase homogeneous reservoir modeled using three grid descriptions: fine ($40 \times 40 \times 8$), coarse ($20 \times 20 \times 4$), and adaptive.

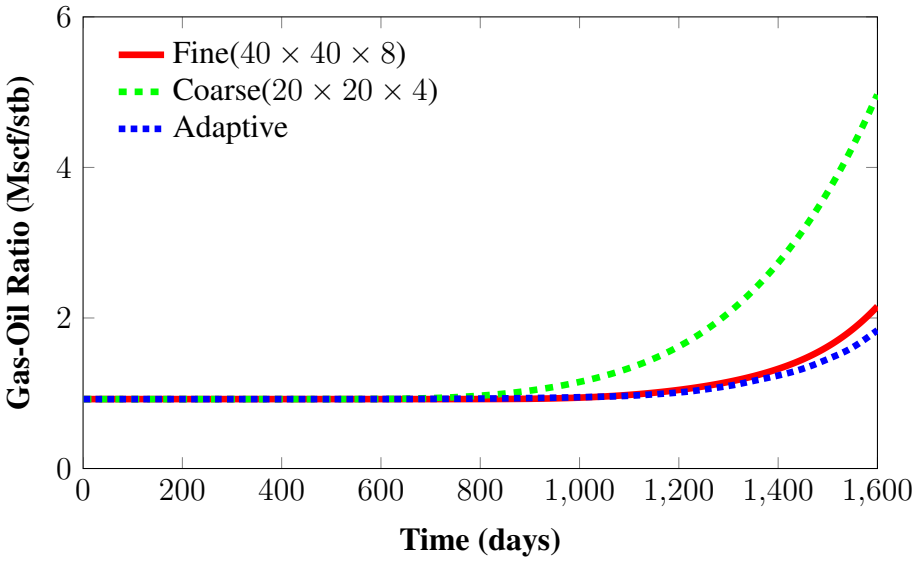

Fig. 5.24—Produced gas-oil ratio after 1,600 days for a 3D single-phase homogeneous reservoir modeled using three grid descriptions: fine ($40 \times 40 \times 8$), coarse ($20 \times 20 \times 4$), and adaptive.

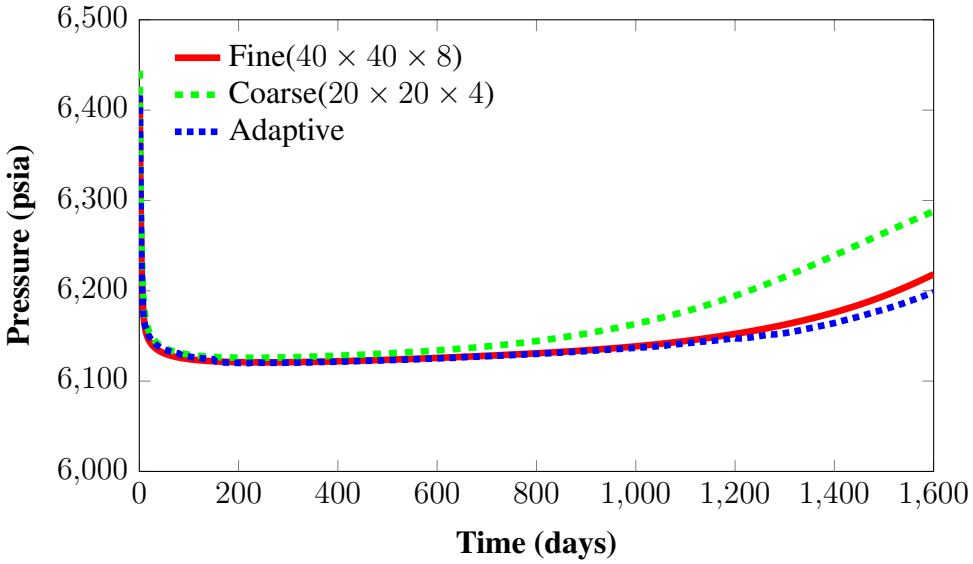

Fig. 5.25—Average reservoir pressure after 1,600 days for a 3D single-phase homogeneous reservoir modeled using three grid descriptions: fine ($40 \times 40 \times 8$), coarse ($20 \times 20 \times 4$), and adaptive.

5.2.2 Two-phase homogeneous model

The reservoir model is represented by a 3D simulation grid discretized with a maximum of 4,608 cells ($n_{x,max}$=24, $n_{y,max}$=24, and $n_{z,max}$=8), where each gridcell measures 33.3 ft by 33.3 ft by 8.75 ft. Cells can be grouped using two hierarchical levels for a maximum cell dimension of 133.3 ft by 133.3 ft by 35 ft as shown in **Fig. 5.26**. **Table 5.12** summarizes the grid input parameters.

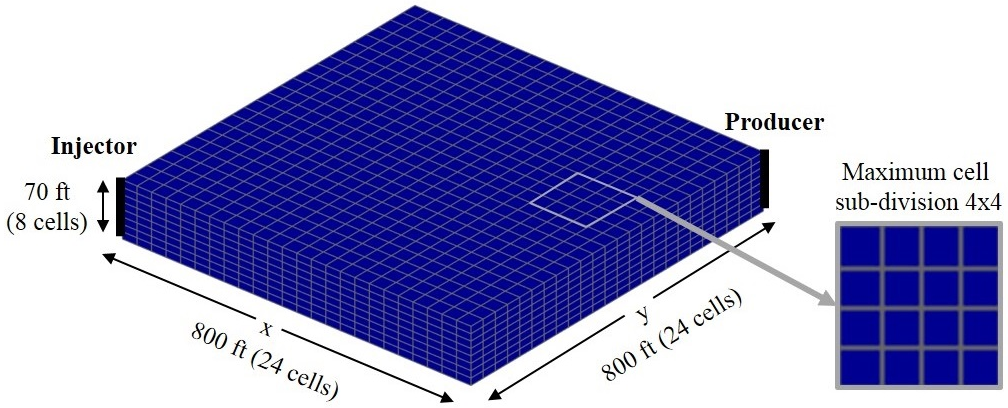

Fig. 5.26—3D model used to evaluate the two-phase homogeneous reservoir with an areal extension of 15 acres and thickness of 70 ft. Fine cells can be grouped into coarser cells up to a maximum of $4 \times 4 \times 4$.

Table 5.16—Input grid parameters used in the 3D two-phase and homogeneous simulation model

Property	Value
Length, ft	800
Width, ft	800
Thickness, ft	70
Grid size in x-direction (finest), ft	33.3
Grid size in y-direction (finest), ft	33.3
Grid size in z-direction (finest), ft	8.75
Grid size in x-direction (coarsest), ft	133.3
Grid size in y-direction (coarsest), ft	133.3
Grid size in z-direction (coarsest), ft	35

Two cases are evaluated considering two-phase flow. In Case 1, the reservoir is initialized in single-phase with a constant pressure of 5,600 psia and no gas saturation. The producer well was set to produce at a constant bottomhole flowing pressure of 5,000 psia, below the bubble point pressure, while the injector well was set at 6,000 psia. In Case 2, the reservoir was initialized in two-phases with a constant pressure of 5,000 psia and a gas saturation of 7.5%. The producer bottomhole flowing pressure was set at 4,500 psia while the injector was set at 5,500 psia. A summary of the initial and operating conditions is listed in **Table 5.17**.

Table 5.17—Initial and operating conditions in the 3D two-phase and homogeneous simulation model

Property	**Value (Case 1)**	**Value (Case 2)**
Initial pressure, psia	5,600	5,000
Initial gas saturation, fraction	0.0	0.075
Producer bottomhole flowing pressure, psia	5,000	4,500
Injector bottomhole flowing pressure, psia	6,000	5,500

Performance comparison of Case 1: Initial pressure above bubble point

This case show the appearance and disappearance of the gas phase throughout the simulation study. The reservoir is found initially in single-phase, but as we begin producing from the well, the region near the wellbore falls below the bubble point pressure causing the gas to break out of solution. Continuing production results in the two-phase region progressively expanding towards the injector well. On the opposite side of the model, CO_2 injections creates a liquid single-phase front moving towards the low pressure region (i.e. producer well). As CO_2 continuously interact with the in-situ oil, the system reaches a single-phase state as shown in **5.27**.

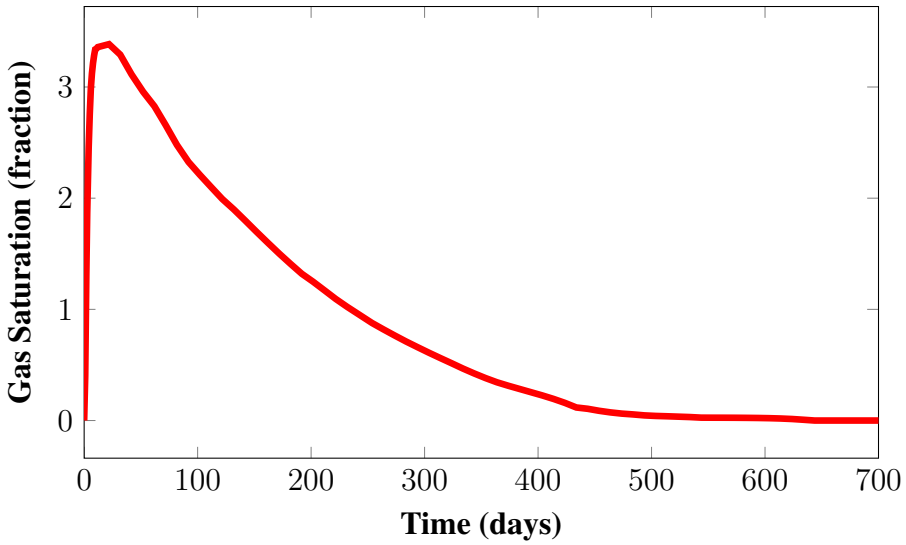

Fig. 5.27—Average field gas saturation showing the reservoir initialized in liquid single-phase. Gas saturation increases as pressure falls below the bubble point near the producer well, but re-dissolves as CO_2 contacts and mixes with the in-situ oil.

Figs. 5.28 and **5.29** show the grid discretization in the adaptive model as the injection front advances towards the producers for 100, 160, 200, 250, 340, and 440 days. The algorithm required 20 different grid realizations with number of cells varying from 520 to 3,194. The reduction in cells in the model resulted in executing the adaptive model 2.57 times faster compared to a static fine grid (modeled with 4,608 cells). This represents a reduction in CPU time of 61.1% (**Table 5.18**).

Table 5.18—Comparison of computational performance for a 3D two-phase homogeneous model initialized above the bubble point

Grid	**Number of cells**	**CPU execution ratio (fine/ adaptive)**	**% CPU reduction**
Fine	4,608	–	–
Adaptive	520 - 3,194	2.57	61.1

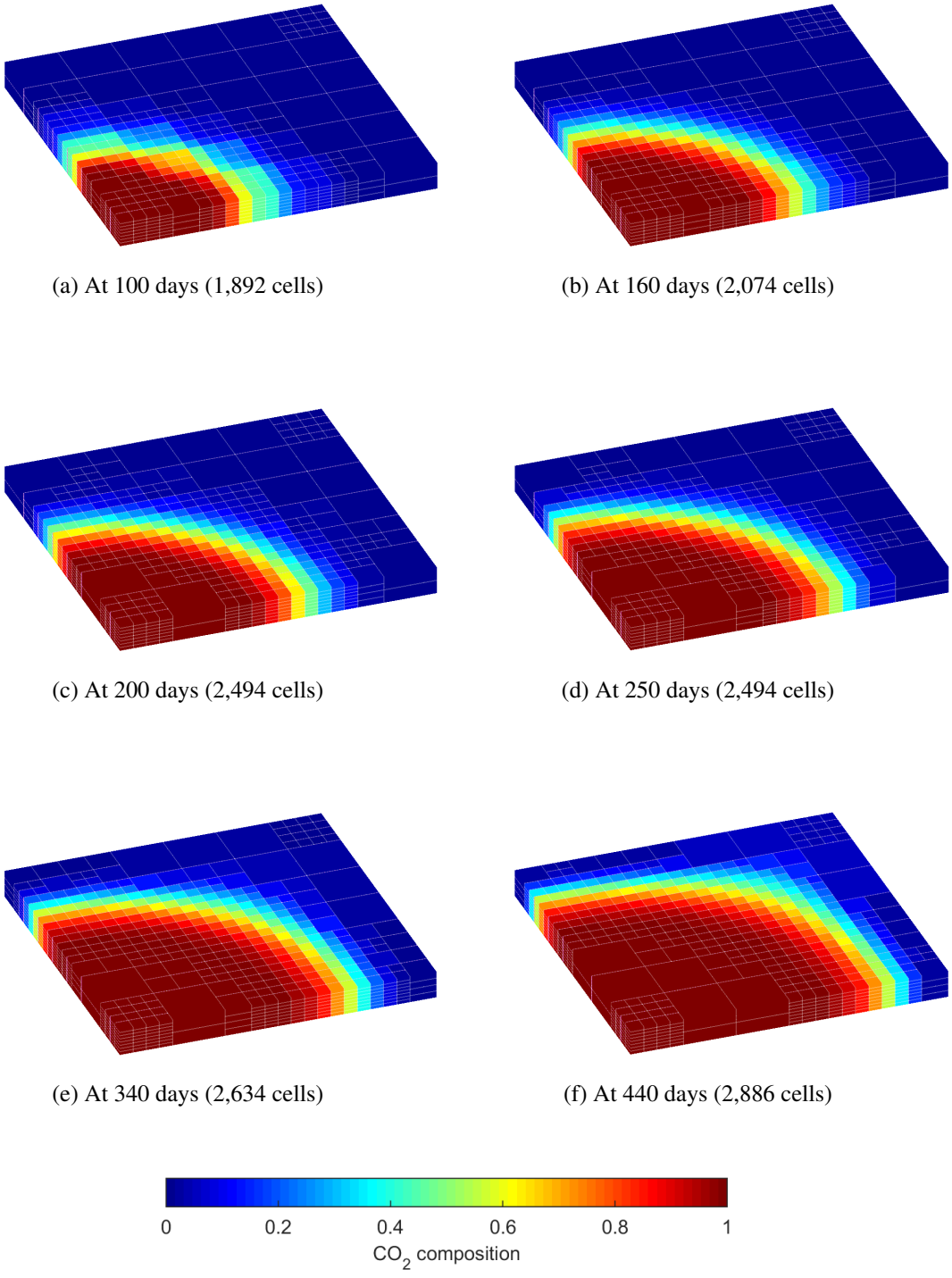

(a) At 100 days (1,892 cells)

(b) At 160 days (2,074 cells)

(c) At 200 days (2,494 cells)

(d) At 250 days (2,494 cells)

(e) At 340 days (2,634 cells)

(f) At 440 days (2,886 cells)

Fig. 5.28—Composition distribution at 100, 160, 200, 250, 340, and 440 days of simulation using an adaptive grid for 3D two-phase homogeneous model initialized above the bubble point.

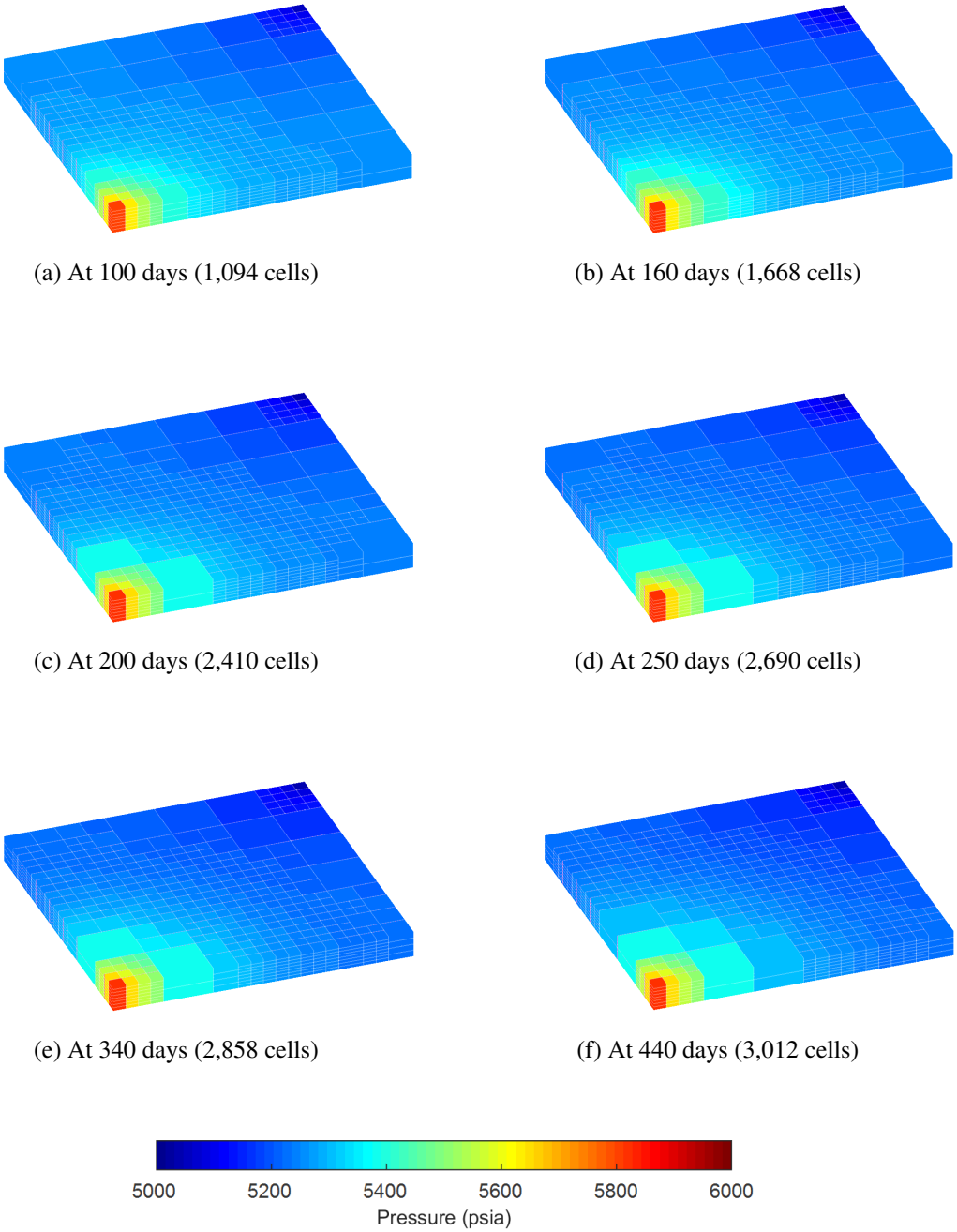

(a) At 100 days (1,094 cells)

(b) At 160 days (1,668 cells)

(c) At 200 days (2,410 cells)

(d) At 250 days (2,690 cells)

(e) At 340 days (2,858 cells)

(f) At 440 days (3,012 cells)

Fig. 5.29—Pressure distribution at 100, 160, 200, 250, 340, and 440 days of simulation using an adaptive grid for 3D two-phase homogeneous model initialized above the bubble point.

Fig. 5.21 to **Fig. 5.21** display the results from oil production, gas injection rate, average pressure, and produced gas-oil ratio. Plots illustrate three cases: 1) fine grid ($24 \times 24 \times 8$ with 4,608 cells), coarse grid ($12 \times 12 \times 4$ with 576 cells), and an adaptive grid (variable number of cells ranging from 520 to 3,194). Results show a 2.70% difference in cumulative oil production between the fine and the adaptive grid after 550 days of production and injection modeling (breakthrough time). On the other hand, using a coarser grid ($12 \times 12 \times 4$) resulted in 12.42% difference in the cumulative oil production. **Table 5.19** shows a summary of the production and pressure errors.

Table 5.19—Errors at breakthrough time (550 days) of the adaptive and coarse grid compared to the fine model in a 3D two-phase homogeneous model initialized above the bubble point

Grid	**% Error in cumulative oil production (STB)**	**% Error in cumulative gas injection (Mscf)**	**% Error in pressure (psia)**
Coarse	12.42	15.03	0.87
Adaptive	2.70	2.95	0.20

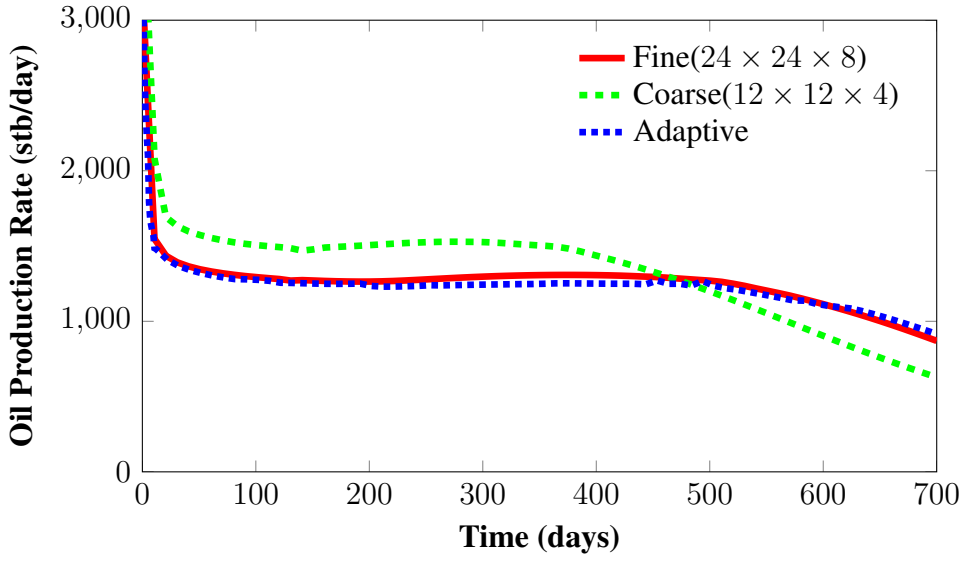

Fig. 5.30—Oil production rate after 700 days for a 3D two-phase homogeneous reservoir initialized above the bubble point and modeled using three grid descriptions: fine ($24 \times 24 \times 8$), coarse ($12 \times 12 \times 4$), and adaptive.

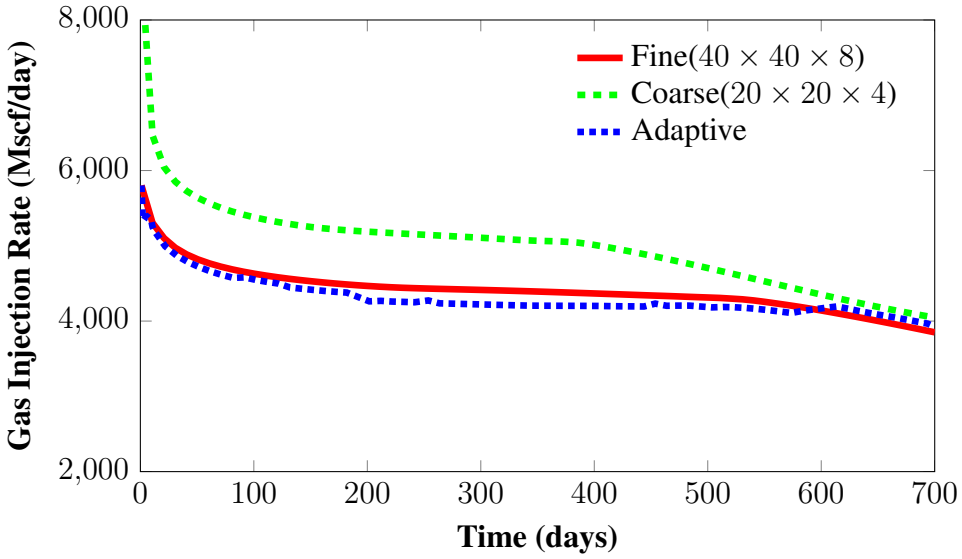

Fig. 5.31—Gas injection rate after 700 days for a 3D two-phase homogeneous reservoir initialized above the bubble point and modeled using three grid descriptions: fine ($24 \times 24 \times 8$), coarse ($12 \times 12 \times 4$), and adaptive.

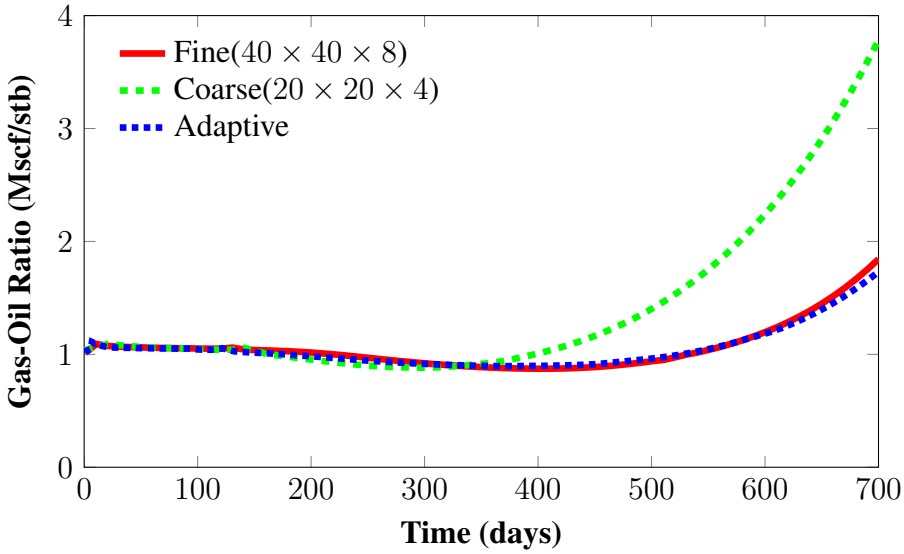

Fig. 5.32—Produced gas-oil ratio (GOR) after 700 days for a 3D two-phase homogeneous reservoir initialized above the bubble point and modeled using three grid descriptions: fine ($24 \times 24 \times 8$), coarse ($12 \times 12 \times 4$), and adaptive.

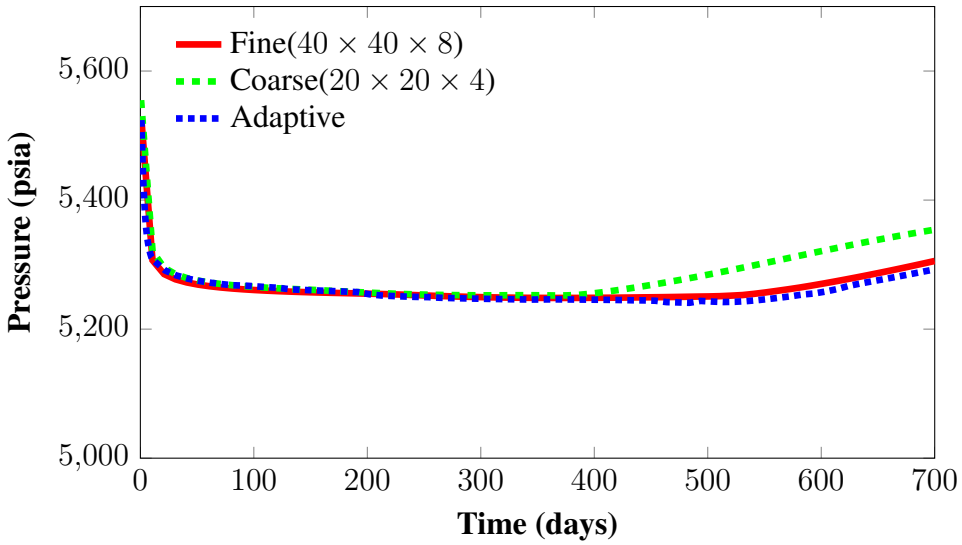

Fig. 5.33—Average reservoir pressure after 700 days for a 3D two-phase homogeneous reservoir initialized above the bubble point and modeled using three grid descriptions: fine ($24 \times 24 \times 8$), coarse ($12 \times 12 \times 4$), and adaptive.

Large changes in phase composition creates additional challenges for the methodology, where the streamline and analytical calculation of compositions need to consider appearance and disappearance of phases. For this case, it is required to calculate the streamlines in each phase. This is illustrated in **Figs. 5.34** and **5.35** corresponding to the gas phase velocity for the longest and shortest streamline in the model. As the gas re-dissolves, the gas-phase streamline only cover the section of the model closest to the producer well, where pressure is the lowest and there is no CO_2 yet. **Fig. 5.36** displays the CO_2 composition in the gas phase showing the volatilized CO_2 region.

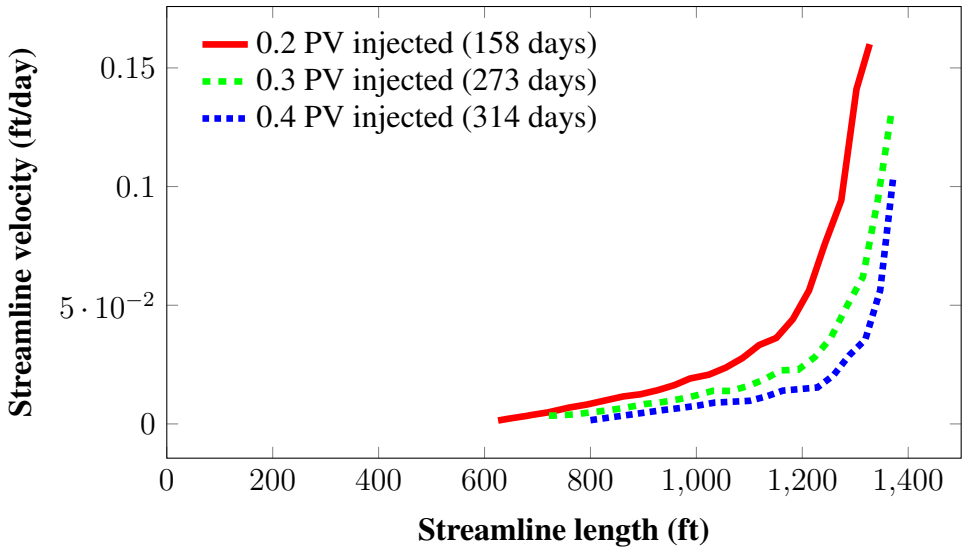

Fig. 5.34—Velocity in the gas phase for the longest streamline in the model at three different times, after 0.2, 0.3, and 0.4 pore volumes injected.

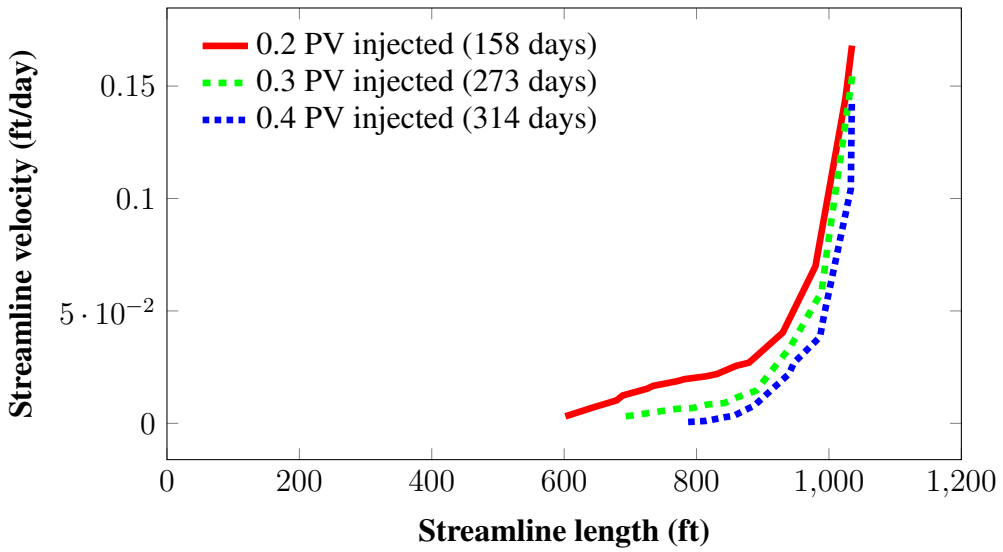

Fig. 5.35—Velocity in the gas phase for the shortest streamline in the model at three different times, after 0.2, 0.3, and 0.4 pore volumes injected.

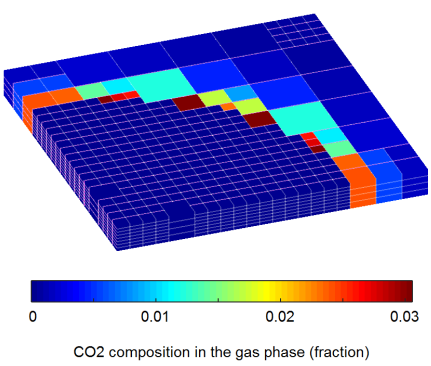

(a) At 0.2 PV injected (158 days)

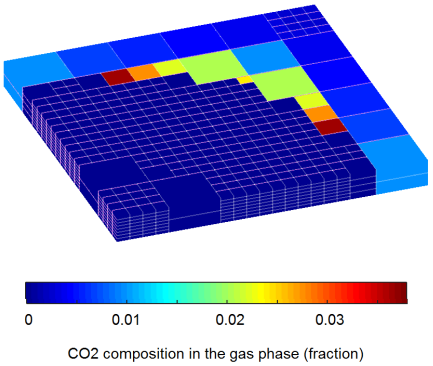

(b) At 0.3 PV injected (273 days)

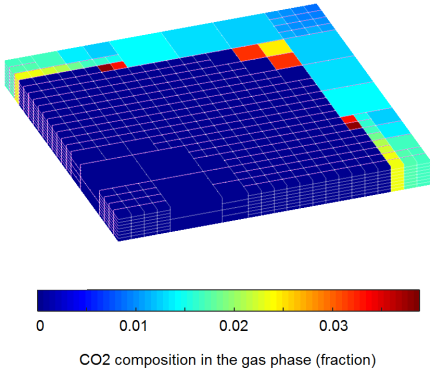

(c) At 0.4 PV injected (314 days)

Fig. 5.36—CO_2 composition in the gas phase showing the re-dissolution of the gas phase at three different times (158, 273, and 314 days).

On the other hand, the velocity of streamlines for the oil phase remains relatively constant throughout the injection period, exhibiting the highest speed near the injector and producer well as shown in **Figs. 5.37** and **5.38** . **Fig. 5.39** displays the CO_2 composition in the oil phase at 0.3 pore volume injected, at breakthrough, and after breakthrough.

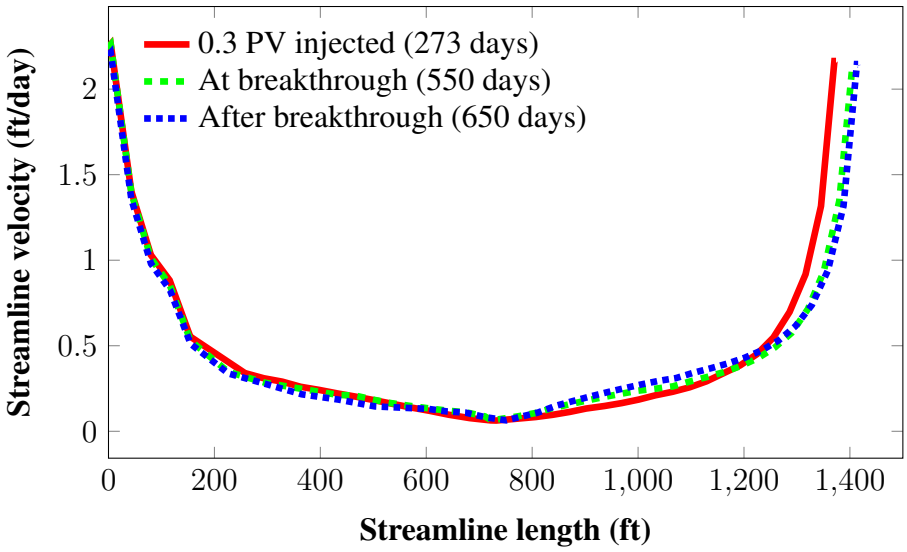

Fig. 5.37—Velocity in the oil phase for the longest streamline in the model at three different times, after 0.3 pore volumes injected, at breakthrough, and after breakthrough.

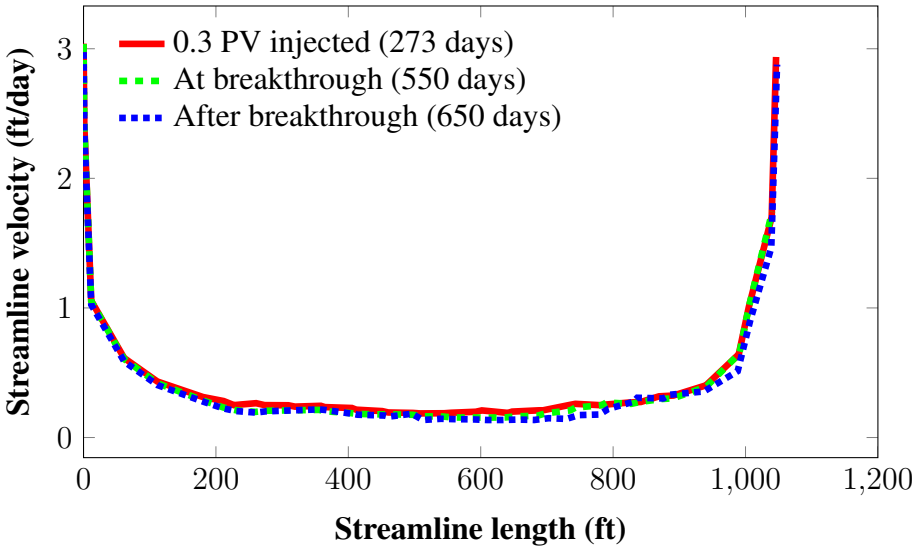

Fig. 5.38—Velocity in the oil phase for the shortest streamline in the model at three different times, after 0.3 pore volumes injected, at breakthrough, and after breakthrough.

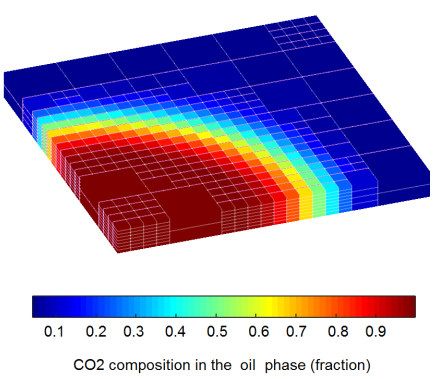

(a) At 0.3 PV injected (273 days)

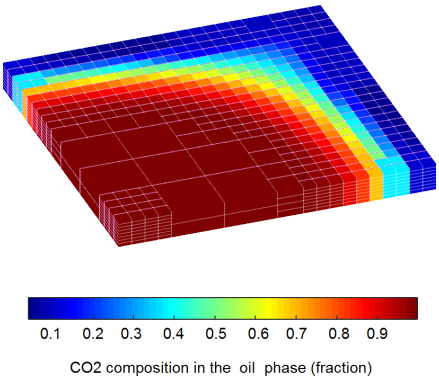

(b) At breakthrough (550 days)

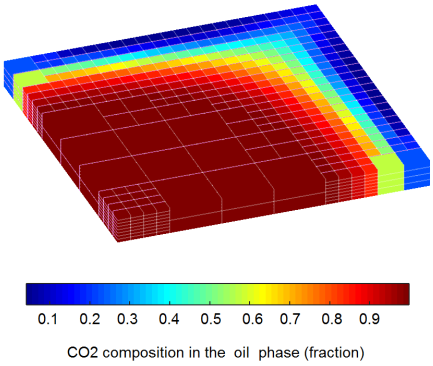

(c) After breakthrough (650 days)

Fig. 5.39—CO_2 composition in the oil phase showing the re-dissolution of the gas phase.

The overall CO_2 composition along the streamline can be observed in **Figs. 5.40** for different times of the simulation: 0.2 and 0.3 pore volume injected, at breakthrough, and after the breakthrough. The illustration shows the progression of streamline trajectories and the corresponding overall composition of the injected component.

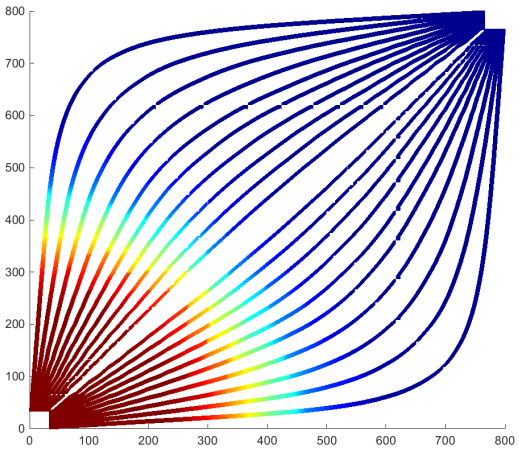

(a) At 158 days (at 0.2 PV injected)

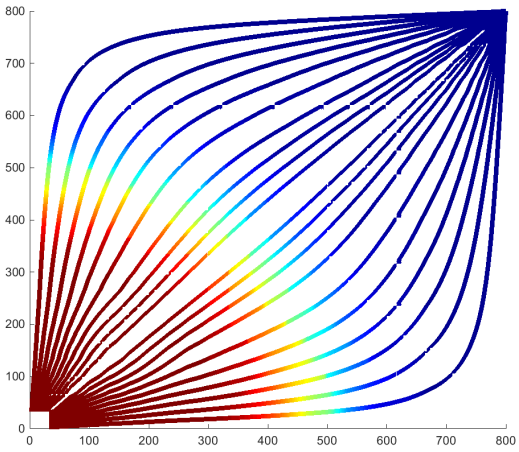

(b) At 273 days (at 0.3 PV injected)

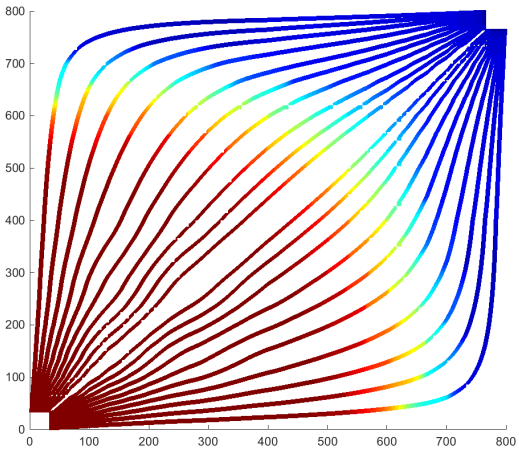

(c) At 550 days (at breakthrough)

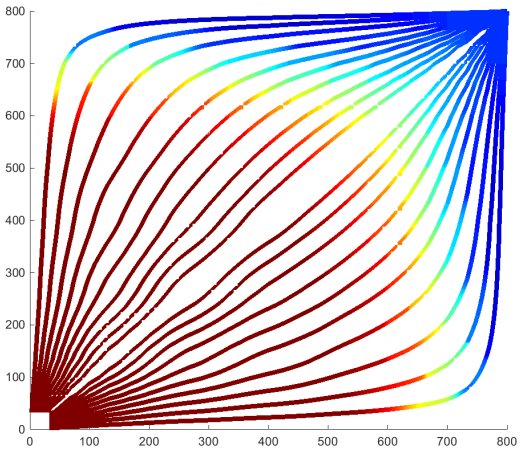

(d) At 650 days (after breakthrough)

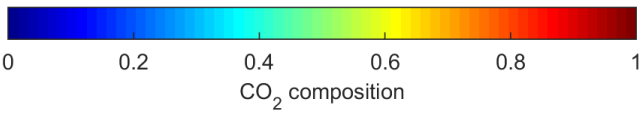

Fig. 5.40—Overall CO_2 composition distribution along the streamlines at 158, 273, 550, and 650 days of simulation.

Performance comparison of Case 2: Initial pressure below bubble point

In this case, the reservoir is initialized in two-phases, exhibiting an initial gas saturation in the model. As CO_2 is injected above the minimum miscibility pressure (single-phase), the displacement front results in re-dissolution of the gas phase at approximately 500 days. Similar to the previous case, we require to trace the streamlines and the solute transport equation in both the liquid and the gas phase. This is an important consideration to test the methodology as the relative movement of the gas-to-oil phase results in CO_2 being transported at different rates. For this case, the Peclet number varies from to 50-100 in the middle of the model to approximately 10,000 near the wells where the velocity is the highest. The calculated dispersivity coefficient ranges between 0.001 and 0.0001 during the simulation.

Results of adaptive grid refinement are illustrated in **Figs. 5.41** and **5.42** for 50, 100, 180, 250, 340, and 440 days. Cells are refined on time based on the distribution of compositions, resulting in fine cells along the injection front but coarser cells anywhere else in the model. The total number of cells was significantly reduced, from 12,800 cells required for a fixed-fine grid, to having 17 different grids varying from 520 to 3,222 cells. Reduction in the number of cells in the model resulted in the adaptive grid being 2.3 times faster than the fine grid, representing a reduction in CPU time of 56.57%.

Table 5.20—Comparison of computational performance for a 3D two-phase homogeneous model initialized below the bubble point

Grid	**Number of cells**	**CPU execution ratio (fine/ adaptive)**	**% CPU reduction**
Fine	4,608	–	–
Adaptive	520 - 3,222	2.3	56.57

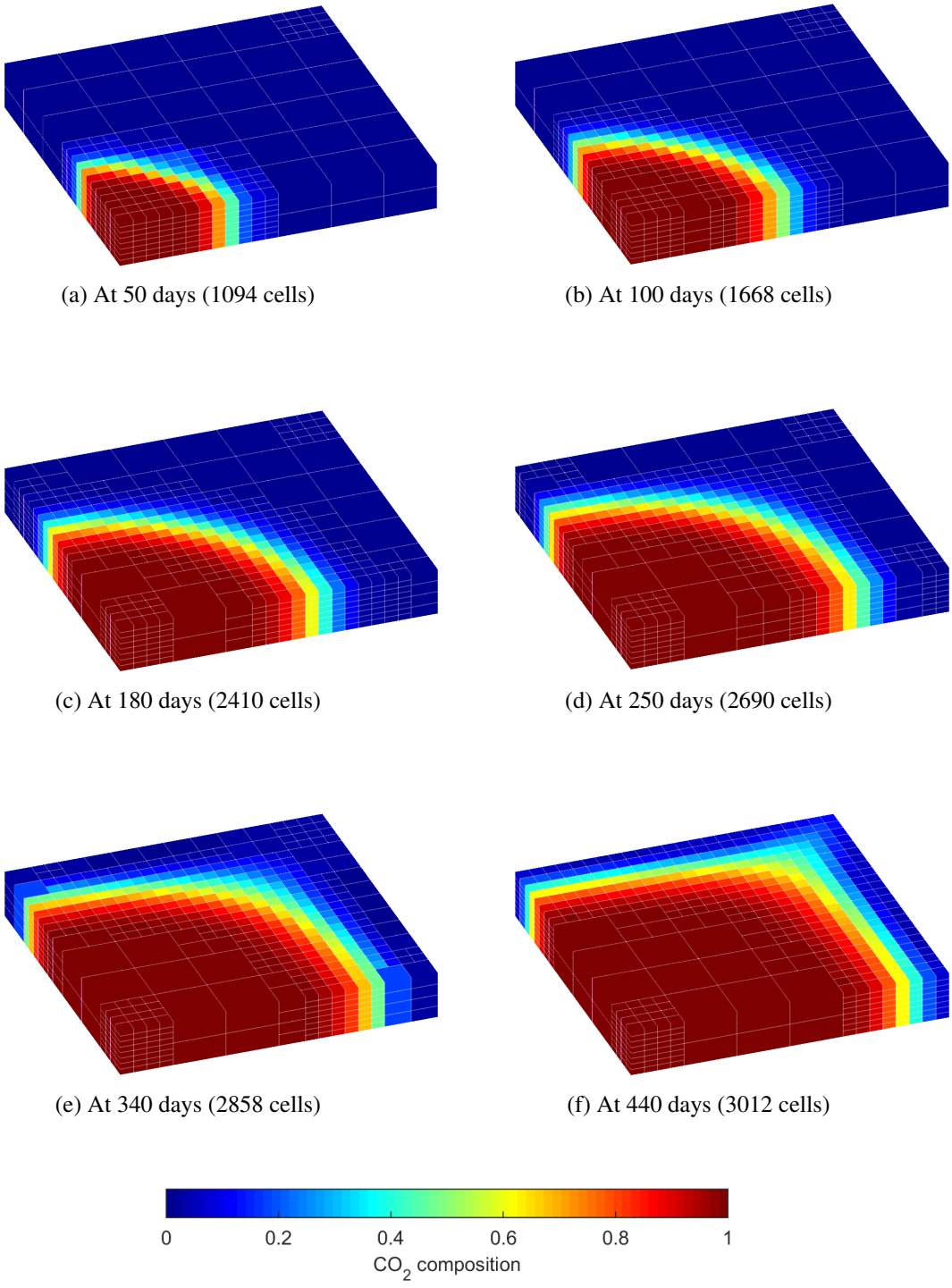

(a) At 50 days (1094 cells)

(b) At 100 days (1668 cells)

(c) At 180 days (2410 cells)

(d) At 250 days (2690 cells)

(e) At 340 days (2858 cells)

(f) At 440 days (3012 cells)

Fig. 5.41—Composition distribution at 50, 100, 180, 250, 340, and 440 days of simulation using an adaptive grid for 3D two-phase homogeneous model initialized below the bubble point.

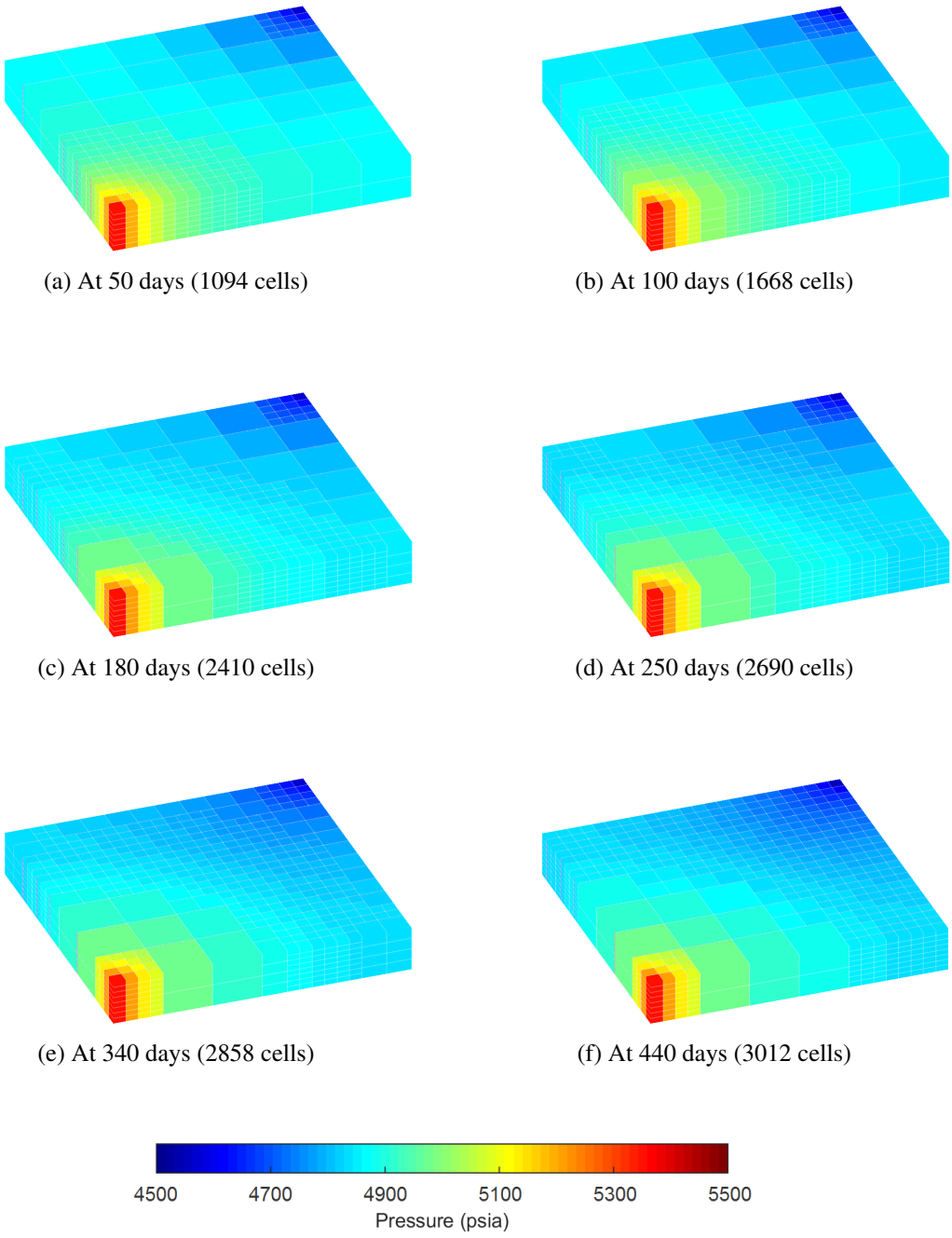

(a) At 50 days (1094 cells)

(b) At 100 days (1668 cells)

(c) At 180 days (2410 cells)

(d) At 250 days (2690 cells)

(e) At 340 days (2858 cells)

(f) At 440 days (3012 cells)

Fig. 5.42—Pressure distribution at 50, 100, 180, 250, 340, and 440 days of simulation using an adaptive grid for 3D two-phase homogeneous model initialized below the bubble point.

Fig. 5.43 to **Fig. 5.21** display the results from oil production, gas injection rate, average pressure, and produced gas-oil ratio. Plots illustrate three cases: 1) fine grid ($24 \times 24 \times 8$ with 4,608 cells), coarse grid ($12 \times 12 \times 4$ with 576 cells), and an adaptive grid (variable number of cells ranging from 520 to 3,222). Results show a 2.59% difference in cumulative oil production between the fine and the adaptive grid after 550 days of production and injection modeling (breakthrough time). On the other hand, using a coarser grid ($12 \times 12 \times 4$) resulted in 6.48% difference in the cumulative oil production. **Table 5.21** shows a summary of the production and pressure errors.

Table 5.21—Errors at breakthrough time (550 days) of the adaptive and coarse grid compared to the fine model in a 3D two-phase homogeneous model initialized below the bubble point

Grid	**% Error in cumulative oil production (STB)**	**% Error in cumulative gas injection (Mscf)**	**% Error in pressure (psia)**
Coarse	6.48	12.71	0.53
Adaptive	2.59	2.87	0.49

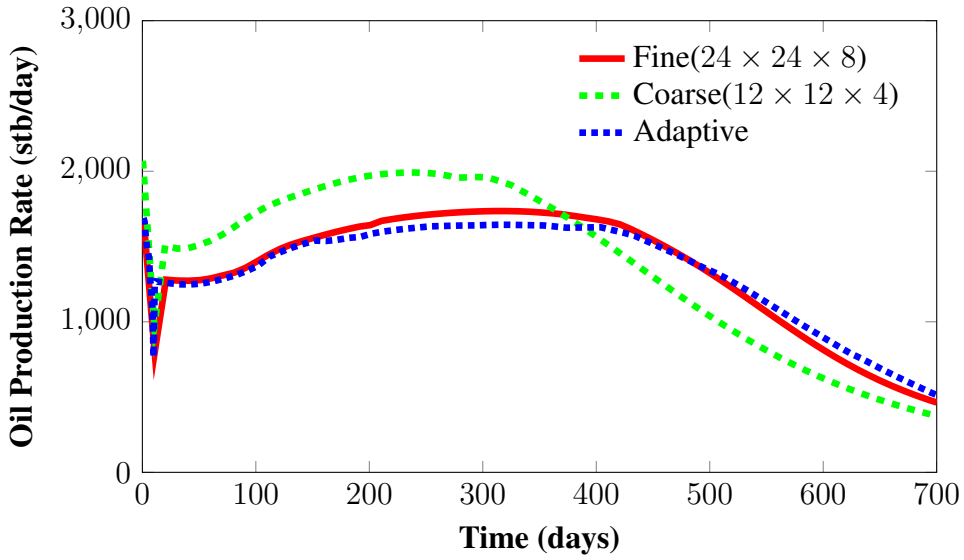

Fig. 5.43—Oil production rate after 700 days of simulation for a 3D two-phase homogeneous reservoir initialized below the bubble point and modeled using three grid descriptions: fine ($24 \times 24 \times 8$), coarse ($12 \times 12 \times 4$), and adaptive.

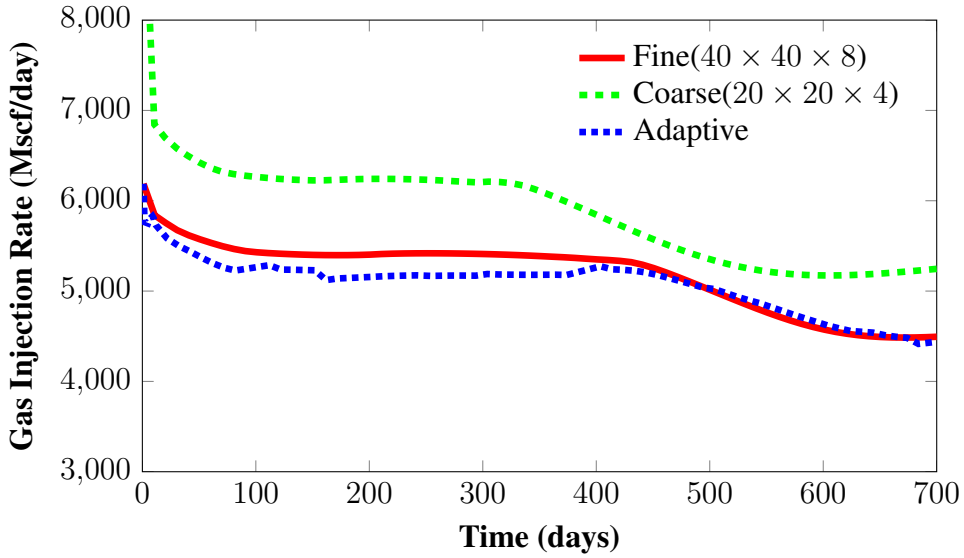

Fig. 5.44—Gas injection rate after 700 days for a 3D two-phase homogeneous reservoir initialized below the bubble point and modeled using three grid descriptions: fine ($24 \times 24 \times 8$), coarse ($12 \times 12 \times 4$), and adaptive.

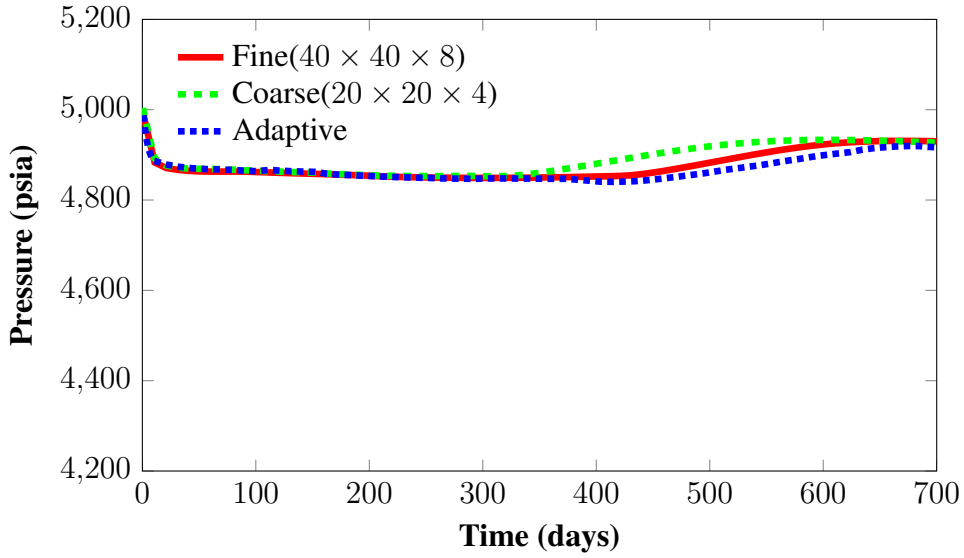

Fig. 5.45—Average reservoir pressure after 700 days for a 3D two-phase homogeneous reservoir initialized below the bubble point and modeled using three grid descriptions: fine ($24 \times 24 \times 8$), coarse ($12 \times 12 \times 4$), and adaptive.

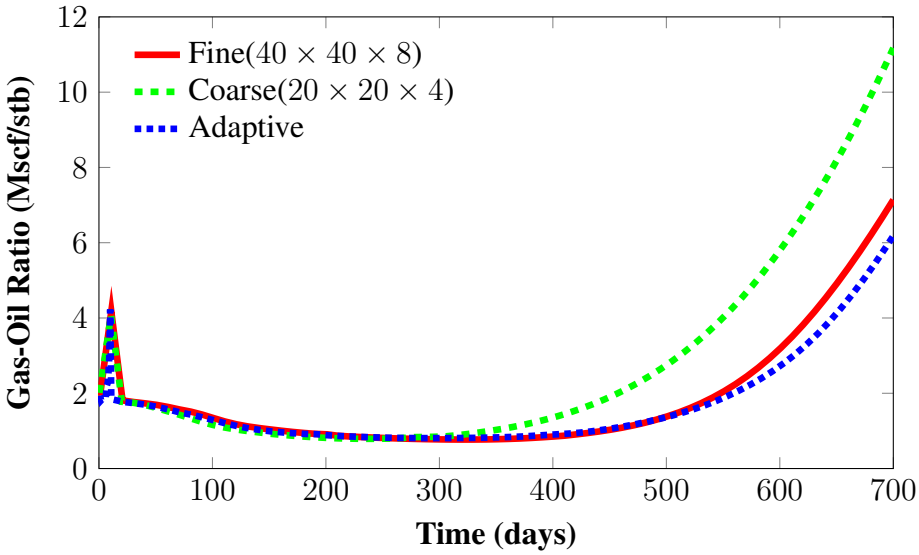

Fig. 5.46—Produced gas-oil ratio (GOR) after 700 days for a 3D two-phase homogeneous reservoir initialized below the bubble point and modeled using three grid descriptions: fine ($24 \times 24 \times 8$), coarse ($12 \times 12 \times 4$), and adaptive.

CHAPTER VI
CONCLUSIONS AND RECOMMENDATIONS

The proposed methodology shows that combining reservoir simulation, streamline, and the solute transport equation provides an improved method for adaptive mesh refinement, accurately forecasting the location of the injection front. Results from this study also allow drawing the following conclusions:

1. Using the convective-dispersive equation enables forecasting the injection front location, shape, and width in single- and two-phase reservoirs. This allows identifying and anticipating the refinement region and times where: fine spatial discretization is needed to reduce numerical dispersion effects or, coarsening can be implemented solution without sacrificing accuracy with substantial execution time reductions.

2. Merging and splitting cells is dynamically implemented by designing multiple homogeneity tests with Quadtree decomposition. These physics based rules allow great flexibility for problem-specific solutions, combining static (e.g., permeabilities, facies) and dynamic reservoir properties (e.g., fluid composition, phase stability tests) as required, improving the accuracy of reservoir performance in adaptive grid refinement cases.

3. Benchmark comparisons of reservoir performance indicators such as: rates, saturations, and pressures, and relative CPU indicate that the adaptive mesh refinement and coarsening method developed in this work can be successfully applied to multiphase, compositional, heterogeneous, and 3-dimensional models.

4. The methodology implemented reduced the computational cost in the cases evaluated up to 63% with respect to a refined base grid. Oil and gas production rates differed by a maximum of 3.71% compared to the bench mark fine grid.

The proposed recommendations and future work related to this project are:

1. Generate and run scenarios that will result in more complex injection fronts by specifying one or more of the following cases:

   - Use of multiple injection and production wells.
   - Run cases where diffusion controls the process (N_{Pe} < 10).
   - Establish larger pressure differentials from injector to producer wells.
   - Use production schedules requiring sudden injection/production pressures or rates.
   - Use different solvent (gas injection)/oil characteristic such that numerical dispersion is more pronounced. This would require higher API oils and CO_2 or N_2 injection streams.

2. Develop dimensionless refinement/coarsening functions to establish a systematic methodology for determining the tolerance criteria. These functions may involve compositional gradients combined with time of flight and velocity gradients.

3. Use smaller and larger reservoir test cases with different base grids to generalize / determine the relative improvement in CPU time.

4. Explore the implementation of advanced permeability upscaling techniques and multiscale simulation to properly incorporate multiple levels of geologic description into a single reservoir model. This approach would allow maintaining key flow features that impact the overall reservoir response.

5. Investigate the impact of cell re-ordering scheme and matrix solvers in the computational performance of the adaptive mesh refinement. The current work did not evaluate the computational performance of solvers or preconditioning techniques specific for unstructured grids. Some techniques that may be applicable are Reverse Cuthill-McKee (RCMK) and Minimum Degree Fill (MDF).

6. Evaluate the use of higher-order finite difference methods to reduce numerical dispersion and grid orientation effects. The use of higher-order solutions is particularly important when using unstructured grids as first-order approximation result in additional numerical dispersion. A suggested method was proposed by Datta-Gupta et al. (1991) in their work named "High-resolution monotonic schemes for reservoir fluid flow simulation" and published in In Situ, Journal Volume: 15:3. The authors focused on reservoir fluid flow problems for convection-dominated flow. This methodology can be implemented by introducing a limited antidiffusive flux that remains third-order accuracy in space and time, proving advantageous to improve accuracy of IMPES problems where pressure is solved implicitly but compositions and saturations are calculated explicitly.

REFERENCES

Acs, G., Doleschall, S., and Farkas, E. 1985. General purpose compositional model. *Society of Petroleum Engineers Journal* **25**(04):543–553.

Babson, E. C. 1989. A review of gas injection projects in california. SPE 18769 presented at the SPE California Regional Meeting, 5-7 April, Bakersfield, California.

van Batenburg, D. W., Bosch, M., Boerrigter, P. M., De Zwart, A., and Vink, J. C. 2011. Application of dynamic gridding techniques to IOR/EOR-processes. SPE 141711 presented at SPE Reservoir Simulation Symposium, 21-23 February, The Woodlands, Texas,.

Batycky, R., Blunt, M., and Thiele, M. 1997. A 3D field-scale streamline-based reservoir simulator. *SPE Reservoir Engineering* **12**(04):246–254.

Biterge, M. B., and Ertekin, T. 1992. Development and testing of a static/dynamic local grid-refinement technique. *Journal of Petroleum Technology* **44**(04):487–495.

Brandt, A. 1977. Multi-level adaptive solutions to boundary-value problems. *Mathematics of Computation* **31**(138):333–390.

Camy, J. P., and Emanuel, A. S. 1977. Effect of grid size in the compositional simulation of CO_2 injection. SPE 6894 presented at the SPE Annual Fall Technical Conference and Exhibition, 9-12 October, Denver, Colorado.

Chien, M., Lee, S., and Chen, W. 1985. A new fully implicit compositional simulator. SPE 13385 presented at the SPE Reservoir Simulation Symposium, 10-13 February, Dallas, Texas.

Christensen, J., Darche, G., Dechelette, B., Ma, H., and Sammon, P. 2004. Applications of dynamic gridding to thermal simulations. SPE 86969 presented at the SPE International Thermal Operations and Heavy Oil Symposium and Western Regional Meeting, 16-18 March, Bakersfield, California.

Christie, M., and Blunt, M. 2001. Tenth SPE comparative solution project: A comparison of upscaling techniques. SPE Reservoir Simulation Symposium, 11-14 February, Houston, Texas.

Coats, K. H. 1980. An equation of state compositional model. *Society of Petroleum Engineers Journal* **20**(05):363–376.

Coats, K. H. 2003a. IMPES stability: Selection of stable timesteps. *Society of Petroleum Engineers Journal* **8**(02):181 – 187.

Coats, K. H. 2003b. IMPES stability: The CFL limit. *Society of Petroleum Engineers Journal* **8**(03):291–297.

Datta-Gupta, A., and King, M. 2007. *Streamline simulation: theory and practice*. Textbook Series, Society of Petroleum Engineers. Richardson, Texas.

Durlofsky, L. J. 2003. Upscaling of geocellular models for reservoir flow simulation: a review of recent progress. Paper presented at 7th International Forum on Reservoir Simulation, June 23-27, Buhl/Baden-Baden, Germany.

Edwards, M. 1996. A higher-order godunov scheme coupled with dynamic local grid refinement for flow in a porous medium. *Computer Methods in Applied Mechanics and Engineering* **131**(3-4):287–308.

Edwards, M., and Christie, M. A. 1993. Dynamically adaptive godunov schemes with renormalization in reservoir simulation. SPE 25268 presented at the SPE Symposium on Reservoir Simulation, 28 February-3 March, New Orleans, Louisiana.

Fanchi, J. R. 1983. Multidimensional numerical dispersion. *Society of Petroleum Engineers Journal* **23**(01):143–151.

Firoozabadi, A. 1988. Reservoir-fluid phase behavior and volumetric prediction with equations of state. *Journal of Petroleum Technology* **40**(04):397 – 406.

Firoozabadi, A. 1999. *Thermodynamics of hydrocarbon reservoirs*. McGraw-Hill Education.

Fleming, P., and Mansoori, J. 1987. An accurate numerical technique for solution of convection-diffusion equations without numerical dispersion. *SPE Reservoir Engineering* **2**(03):373–386.

Fletcher, P. E. 1953. *A Review of gas-injection projects in West Texas*. American Petroleum Institute. New York, New York.

Fussell, L., and Fussell, D. 1979. An iterative technique for compositional reservoir models. *Society of Petroleum Engineers Journal* **19**(04):211–220.

van Genuchten, M., and Alves, W. J. 1982. *Analytical Solutions of the One-Dimensional Convective-Dispersive Solute Transport Equation*. U.S. Department of Agriculture, Technical Bulletin. Number 1661.

Gerald, C., and Wheatley, P. 1984. *Applied numerical analysis*. World student series. Addison-Wesley Pub. Co.

Gonzalez, R. C., Woods, R. E., and Eddins, S. L. 2003. *Digital Image Processing Using MATLAB*. Pearson Prentice Hall.

Hall, H. N., Merliss, F. E., and Ewing, S. P. 1957. *A review of improved gas-drive processes*. American Petroleum Institute. New York, New York.

Han, D. K., Han, D., Yan, C. Z., and Peng, L. T. 1987. A more flexible approach of dynamic local grid refinement for reservoir modeling. SPE Symposium on Reservoir Simulation, 1-4 February, San Antonio, Texas.

Heinemann, Z. E., Gerken, G., and von Hantelmann, G. 1983. Using local grid refinement in a multiple-application reservoir simulator. SPE 12255 presented at SPE Reservoir Simulation Symposium, 15-18 November, San Francisco, California.

Hornung, R. D., and Trangenstein, J. A. 1997. Adaptive mesh refinement and multilevel iteration for flow in porous media. *Journal of Computational Physics* **136**(02):522–545.

Jhaveri, B. S., Brodie, J. A., Zhang, P., and Daae, V. 2014. Review of BP's global gas injection projects. SPE 171780 presented at the Abu Dhabi International Petroleum Exhibition and Conference, 10-13 November, Abu Dhabi, UAE.

Khan, S. A., Trangenstein, J. A., Horning, R. D., Holing, K., and Schilling, B. E. R. 1995. Application of adaptive mesh-refinement with a new higher-order method in simulation of a North Sea micellar/polymer flood. SPE 29145 presented at SPE Reservoir Simulation Symposium, 12-15 February, San Antonio, Texas.

King, M., and Mansfield, M. 1999. Flow simulation of geologic models. *SPE Reservoir Evaluation Engineering* **2**(04):351 – 367.

Kumar, S., Datta-Gupta, A., and Jimenez, E. 2009. Understanding reservoir mechanisms using phase and component streamline tracing and visualization. SPE 124252 presented at SPE Annual Technical Conference and Exhibition, 4-7 October, New Orleans, Louisiana.

Lake, L. W. 1989. *Enhanced oil recovery*. Prentice Hall; 1st edition. Englewood Cliffs, New Jersey.

Lantz, R. B. 1971. Quantitative evaluation of numerical diffusion (truncation error). *Society of Petroleum Engineers Journal* **11**(03):315–320.

Laumbach, D. D. 1975. A high-accuracy finite-difference technique for treating the convection-diffusion equation. *Society of Petroleum Engineers Journal* **15**(06):517–531.

Liang, Q., and Borthwick, A. 2009. Adaptive quadtree simulation of shallow flows with wet–dry fronts over complex topography. *Computers Fluids* **38**(2):221–234.

Liang, Q., Zang, J., Borthwick, A., and Taylor, P. H. 2007. Shallow flow simulation on dynamically adaptive cut cell quadtree grids. *Computers Fluids* **53**(12):1777–1799.

Lohrenz, J., Bray, B. G., and Clark, C. R. 1964. Calculating viscosities of reservoir fluids from their compositions. *Journal of Petroleum Science and Engineering* **16**(10):1171–1176.

Michelsen, M. L., and Mollerup, J. M. 2007. *Thermodynamic models: fundamentals & computational aspects*. Tie-Line Publications. Holte, Denmark.

Moog, G. 2013. Advanced discretization methods for flow simulation using unstructured grids. Ph.D. dissertation; Stanford University. Palo Alto, California.

Nghiem, L., Fong, D., and Aziz, K. 1981. Compositional modeling with an equation of state. *Society of Petroleum Engineers Journal* **21**(06):687–698.

Nguyen, Q. M. R. 2009.; Performance of EOR-CO_2 miscible process using a conceptual model. Master's thesis; Texas A&M University. College Station, Texas.

Nilsson, J., Gerritsen, M. G., and Younis, R. 2005a. An adaptive, high-resolution simulation for steam-injection processes. SPE 93881 presented at SPE Western Regional Meeting, 30 March-1 April, Irvine, California.

Nilsson, J., Gerritsen, M. G., and Younis, R. 2005b. A novel adaptive anisotropic grid framework for efficient reservoir simulation. SPE 93243 presented at SPE Reservoir Simulation Symposium, 31 January-2 Feburary, The Woodlands, Texas.

Ogata, A., and Banks, R. 1961. *A solution of the differential equation of longitudinal dispersion in porous media*. United States Geological Surbey Professional Paper 411-A. Washington, D.C.

Peaceman, D. W. 1978. Interpretation of well-block pressures in numerical reservoir simulation. *Society of Petroleum Engineers Journal* **18**(03):183–194.

Peaceman, D. W. 1983. Interpretation of well-block pressures in numerical reservoir simulation with nonsquare grid blocks and anisotropic permeability. *Society of Petroleum Engineers Journal* **23**(03):531–543.

Pedersen, K. S., and Christensen, P. L. 2006. *Phase behavior of petroleum reservoir fluids*. CRC/Taylor & Francis. Boca Raton, Florida.

Peneloux, A., Rauzy, E., and Fréze, R. 1982. A consistent correction for Redlich-Kwong-Soave volumes. *Fluid Phase Equilibria* **8**(01):7–23.

Peng, D. Y., and Robinson, D. B. 1976. A new two-constant equation of state. *Industrial Engineering Chemistry Fundamentals* **15**(01):59–64.

Pollock, D. W. 1988. Semianalytical computation of path lines for finite-difference models. *Ground Water* **26**(06):743.

Prevost, M., Edwards, M. G., and Blunt, M. J. 2001. Streamline tracing on curvilinear structured and unstructured grids. SPE 66347 presented at the SPE Reservoir Simulation Symposium, 11-14 February, Houston, Texas.

Quandalle, P. 1983. The use of flexible gridding for improved reservoir modeling. SPE 12239 presented at the SPE Reservoir Simulation Symposium, 15-18 November, San Francisco, California.

Quandalle, P., and Besset, P. 1985. Reduction of grid effects due to local sub-gridding in simulations using a composite grid. SPE 13527 presented at the SPE Reservoir Simulation Symposium, 10-13 February, Dallas, Texas.

Rachford, H. H., and Rice, J. D. 1952. Procedure for use of electronic digital computers in calculating flash vaporization hydrocarbon equilibrium. *Journal of Petroleum Technology* **04**(10):19–3.

Redlich, O., and Kwong, J. N. S. 1949. On the thermodynamics of solutions. V. An equation of state. Fugacities of gaseous solutions. *Chemical Reviews* **44**(01):233–244.

von Rosenberg, D. U. 1982. Local mesh refinement for finite difference methods. SPE 10974 presented at SPE Annual Technical Conference and Exhibition, 26-29 September, New Orleans, Louisiana,.

Samet, H. 1989. *Applications of spatial data structures: computer graphics, image processing and gis*. Addison-Wesley Pub. Boston, Massachusetts.

Sammon, P. H. 2003. Dynamic grid refinement and amalgamation for compositional simulation. SPE 79683 presented at SPE Reservoir Simulation Symposium, 3-5 February, Houston, Texas.

Schlumberger 2014. *ECLIPSE Technical description and reference manual*. Schlumberger. Abingdon, United Kingdom.

Shusterman, E., and Feder, M. 1994. Image compression via improved quadtree decomposition algorithms. *IEEE Transactions on Image Processing* **3**(02):207–215.

Soave, G. 1972. Equilibrium constants from a modified Redlich-Kwong equation of state. *Chemical Engineering Science* **27**(06):1197–1203.

Spillette, A. G., Hillestad, J. G., and Stone, H. L. 1973. A high-stability sequential solution approach to reservoir simulation. SPE 4542 presented at SPE Annual Fall Meeting, Sept. 30-Oct. 3, Las Vegas, Nevada.

Stone, H. 1970. Probability model for estimating three-phase relative permeability. *Journal of Petroleum Technology* **22**(02):214 – 218.

Stone, H. 1973. Estimation of three-phase relative permeability and residual oil data. *Journal of Canadian Petroleum Technology* **12**(04):53–61.

Suicmez, V. S., van Batenburg, D. W., Matsuura, T., Bosch, M., and Boersma, D. M. 2011. Dynamic local grid refinement for multiple contact miscible gas injection. SPE 15017 presented at International Petroleum Technology Conference, 15-17 November, Bangkok, Thailand.

Sullivan, G., and Baker, R. L. 1994. Efficient quadtree coding of images and videos. *IEEE Transactions on Image Processing* **3**(03):327–331.

van der Waals, J. D. 1873. Over de continuiteit van den gas - en vloeistoftoestand (on the continuity of the gas and liquid state). Ph.D. dissertation; Leiden University. Leiden, The Netherlands.

Watts, J. W. 1986. A compositional formulation of the pressure and saturation equations. *SPE Reservoir Engineering* (03):243–252.

Wilson, G. M. 1969. A modified Redlich-Kwong equation of state, application to general physical data calculation. Paper No. 15C presented at the 1969 AIChE 65th National Meeting, Cleveland, Ohio, March 4-7, 1969.

Wong, T. W., Firoozabadi, A., and Aziz, K. 1990. Relationship of the volume-balance method of compositional simulation to the Newton-Raphson method. *SPE Reservoir Engineering* **5**(03):415–422.

Young, L. C., and Stephenson, R. E. 1983. A generalized compositional approach for reservoir simulation. *Society of Petroleum Engineers Journal* **23**(05):727–742.

APPENDIX A
DERIVATION OF PARTIAL MOLAR VOLUME

This appendix describes the derivation of the partial molar volume ($\overline{V}_i$) for component i in the hydrocarbon phase and for water. This property is used for calculating the flow terms and the final pressure solution as described in Chapter III .

The partial molar volume is the the change of total volume V_t with respect to the change of moles of component i at constant pressure and temperature (Eq. A.1). It represents the contribution of component i to the overall volume of the mixture.

$$\overline{V}_i = \left(\frac{\partial V_t}{\partial n_i}\right)_{p,T,n_j} \tag{A.1}$$

A.1 Hydrocarbon partial molar volume

The derivation begins with the variables from Eq. A.1, that is pressure (p), total volume (V_t), temperature (T), and total number of moles (n).

$$F(p, V_t, T, n) = 0 \tag{A.2}$$

The derivation assumes temperature to be constant in the reservoir. Then, if two of the remaining three variables are related, then one of the variables may be selected as the independent variable and the other two as dependent variables (Michelsen and Mollerup, 2007). If T is kept constant, we can work the partial derivative expressions, we can apply the "minus one rule" as follows:

$$\left(\frac{\partial p}{\partial V_t}\right)_{T,n}\left(\frac{\partial V_t}{\partial n_i}\right)_{p,T,n_j}\left(\frac{\partial n_i}{\partial p}\right)_{V_t,T,n_j} = -1 \tag{A.3}$$

From Eq. A.3 we can define the partial molar volume as shown in Eq. A.4.

$$\overline{V}_i = \left(\frac{\partial V_t}{\partial n_i}\right)_{p,T,n_j} = -\frac{\left(\frac{\partial p}{\partial n_i}\right)_{V_t,T,n_j}}{\left(\frac{\partial p}{\partial V_t}\right)_{T,n}} \tag{A.4}$$

The two pressure derivatives required for calculating Eq. A.4 will be derived using Peng-Robinson equation of state with volume translation. Re-writing Eq. 2.7 as a function of total fluid volume V_t and Peneloux et al.'s volume shift results in Eq. A.5 which will be used throughout this appendix. For the purpose of this derivation, the total volume V_t is the one corrected with volume shift after completing the phase equilibrium analysis outlined in III, section 3.2.

$$p = \frac{RTn}{V_t + nc - nb} - \frac{n^2 a}{(V_t + nc)^2 + 2nb(V_t + nc) - n^2 b^2} \tag{A.5}$$

The following subsections present the basic thermodynamic principles required for the derivation, the linear and quadratic mixing rules for calculating parameters a, b, and c of the mixture, and the partial derivatives of Peng-Robinson equation with respect to n_i and total volume V_t.

Basic thermodynamic properties

Let n be the total number of moles and n_i the number of moles $i = 1, 2, ...N_c$ (Eq. A.6). The derivative of n with respect to n_i is then shown in Eq. A.7.

$$n = n_1 + n_2 + ... + n_{N_c} \tag{A.6}$$

$$\frac{\partial n}{n_i} = 1 \tag{A.7}$$

The mole fraction of component i can be expressed as a molar fraction:

$$x_i = \frac{n_i}{n} \tag{A.8}$$

The molar volume V_m is an intensive property representing the volume occupied by one mole of hydrocarbon mixture.

$$V_m = \frac{V_t}{n} \tag{A.9}$$

Mixing rules and derivatives

The following mixing rules are employed for calculating the parameters a, b, and c of a mixture. Each parameter will be derived with respect to moles n_i as required for the derivation of the partial molar volume.

Linear mixing rule: parameters b ***and*** c

For a mixture of 3 components, we define the b parameter as:

$$b = \sum_{i=1}^{Nc} x_i b_i = x_1 b_1 + x_2 b_2 + x_3 b_3 \tag{A.10}$$

We can express Eq. A.10 in terms of moles:

$$b = \sum_{i=1}^{Nc} \frac{n_i}{n} b_i = \frac{n_1}{n} b_1 + \frac{n_2}{n} b_2 + \frac{n_3}{n} b_3 \tag{A.11}$$

Differentiating with respect to n_i, we have:

$$\frac{\partial b}{\partial n_i} = \sum_{i=1}^{Nc} \frac{b_i}{n^2} \left(n \frac{\partial n_i}{\partial n} - n_i \frac{\partial n}{\partial n_i} \right) = \frac{1}{n} \left(b_i - b \right) \tag{A.12}$$

Similarly, the mixing rule of the c parameters is:

$$c = \sum_{i=1}^{Nc} x_i c_i = \sum_{i=1}^{Nc} \frac{n_i}{n} c_i \tag{A.13}$$

Where $c_i = x_i b_i s_i$. Differentiating Eq. A.15 with respect to n_i, we have:

$$\frac{\partial c}{\partial n_i} = \sum_{i=1}^{Nc} \frac{c_i}{n^2} \left(n \frac{\partial n_i}{\partial n} - n_i \frac{\partial n}{\partial n_i} \right) = \frac{1}{n} \left(c_i - c \right) \tag{A.14}$$

Quadratic mixing rule: parameter a

For a 3-component mixture, the parameter a is represented by the following quadratic rule:

$$a \;\; = \;\; 2x_1x_2(\alpha_{1,2}) + 2x_2x_3(\alpha_{2,3}) + 2x_1x_3(\alpha_{1,3}) + x_1^2a_1 + x_2^2a_2 + x_3^2a_3 \tag{A.15}$$

Where $a_{i,j}$ is a function of parameters a_i for component i and j respectively and $k_{i,j}$ is the binary interaction coefficient between the two components.

$$\alpha_{i,j} = \sqrt{a_i a_j} \left(1 - k_{i,j} \right) \tag{A.16}$$

Expressing Eq. A.15 as a function of number of moles, we have:

$$a = \frac{1}{n^2} \left[2n_1n_2(\alpha_{1,2}) + 2n_2n_3(\alpha_{2,3}) + 2n_1n_3(\alpha_{1,3}) + n_1^2a_1 + n_2^2a_2 + n_3^2a_3 \right] \tag{A.17}$$

Differentiating Eq. A.17 with respect to the number of moles, we have:

$$\frac{\partial a}{\partial n_1} = -\frac{2}{n^3}\Lambda + \frac{1}{n^2} \left[2n_2(\alpha_{1,2}) + 2n_3\alpha_{1,3} + 2n_1a_1 \right] \tag{A.18}$$

Where Λ is:

$$\Lambda = 2n_1n_2(\alpha_{1,2}) + 2n_2n_3(\alpha_{2,3}) + 2n_1n_3(\alpha_{1,3}) + n_1^2a_1 + n_2^2a_2 + n_3^2a_3 \tag{A.19}$$

Generalizing the partial derivative of Eq. A.18 for N_c components, we have:

$$\frac{\partial a}{\partial n_i} = \frac{2}{n}\left(\Psi - a\right) \tag{A.20}$$

Where:

$$\Psi = \sum_{j\neq i=1}^{Nc} \left[x_j\left(\alpha_{ij}\right)\right] + x_ia_i \tag{A.21}$$

Partial derivative of p with respect to V_t

After differentiating Eq. A.5 with respect to total volume, we obtained Eq. A.22, where the parameters a and b are independent from the total volume of the mixture.

$$\left(\frac{\partial p}{\partial V_t}\right)_{T,\vec{N}} = -\frac{RTn}{(V_t + nc - nb)^2} + \frac{2n^2a(V_t + nc + nb)}{[(V_t + nc)^2 + 2nb(V_t + nc) - n^2b^2]^2} \tag{A.22}$$

Partial derivative of p with respect to n_i

Derivation of Eq. A.5 will be split in two terms: repulsion and attraction.

$$p = \underbrace{\frac{RTn}{V_t + nc - nb}}_{Repulsion} - \underbrace{\frac{n^2a}{(V_t + nc)^2 + 2nb(V_t + nc) - n^2b^2}}_{Attraction} \tag{A.23}$$

Repulsion term derivative

$$\frac{\partial}{\partial n_i}\left(\frac{RTn}{V_t+nc-nb}\right)_{V_t,T,n_j}=\frac{RT}{(V_t+nc-nb)^2}\left[(V_t+nc-nb)-\frac{\partial}{\partial n_i}(V_t+nc-nb)\right] \tag{A.24}$$

Applying linear mixing rules for parameters b and c, we have:

$$\begin{aligned}\frac{\partial}{\partial n_i}\left(\frac{RTn}{V_t+nc-nb}\right)_{V_t,T,n_j} &= \frac{RT}{(V_t+nc-nb)^2}\left[(V_t+nc-nb)+nb_i-nc_i\right]\\ &= \frac{RT}{V_t+nc-nb}+\frac{RTn(b_i-c_i)}{(V_t+nc-nb)^2}\end{aligned} \tag{A.25}$$

Attraction term derivative

$$\begin{aligned}\frac{\partial}{\partial n_i}\left(\frac{n^2a}{X}\right)_{V_t,T,n_j} &= \frac{1}{X^2}\left\{X\left[n^2\frac{\partial a}{\partial n_i}+2na\right]-n^2a\left[2(V_t+nc)\left(n\frac{\partial c}{\partial n_i}+c\frac{\partial n}{\partial n_i}\right)\right.\right.\\ &+ 2nb\left(n\frac{\partial c}{\partial n_i}+c\frac{\partial n}{\partial n_i}\right)+2(V_t+nc)\left(n\frac{\partial b}{\partial n_i}+b\frac{\partial n}{\partial n_i}\right)\\ &- \left.\left.\left(n^2\frac{\partial b^2}{\partial n_i}+b^2\frac{\partial n^2}{\partial n_i}\right)\right]\right\}\end{aligned} \tag{A.26}$$

Where X is given by Eq. A.27

$$X=(V_t+nc)^2+2nb(V_t+nc)-n^2b^2 \tag{A.27}$$

Incorporating the derivatives of linear and quadratic mixing rules for a, b, and c and manipulating the terms, we have:

$$\frac{\partial}{\partial n_i}\left(\frac{n^2a}{X}\right)_{V_t,T,n_j}=\frac{2}{X^2}\left\{nX\Psi-n^2a\left[(V_t+nc)c_i+nbc_i+(V_t+nc)b_i-nbb_i\right]\right\} \tag{A.28}$$

Final partial molar volume form

Combining the partial derivative of p with respect to V_t and the partial derivative of p with respect to n_i, we obtain the final form for partial molar volume (Eq. A.29) as a function of molar volume V_m.

$$\overline{V}_i = -\frac{A+B}{C+D+E} \tag{A.29}$$

Where:

$$A = -\frac{RT}{(V_m + c - b)^2} \tag{A.30}$$

$$B = \frac{2a(V_m + c + b)}{[(V_m + c)^2 + 2b(V_m + c) - b^2]^2} \tag{A.31}$$

$$C = \frac{RT}{V_m + c - b} + \frac{RT(b_i - c_i)}{(V_m + c - b)^2} \tag{A.32}$$

$$D = -\frac{2\Psi}{X_2} + a\frac{(V_m + c)c_i}{X_2^2} \tag{A.33}$$

$$E = \frac{2a}{X_2^2}(bc_i - bb_i) - \frac{2ab_i}{X_2^2}(V_m + c) \tag{A.34}$$

$$X_2 = (V_m + c)^2 + 2b(V_m + c) - b^2 \tag{A.35}$$

A.2 Water partial molar volume

Water is assumed to be a pure component immiscible in the oil and gas, then the partial derivative of total fluid volume with respect to water is defined as Eq. A.36, where V_{m_w} is the molar volume of the water phase.

$$\overline{V}_w = \left(\frac{\partial V_t}{\partial n_w}\right)_{p,T,n_i} = V_{m_w} \tag{A.36}$$

APPENDIX B
DERIVATION OF VOID TERM

This appendix presents the calculation of the term Void as described in Chapter III, where c_f is the rock compressibility, and V_p^{ref} is the pore volume at reference pressure p^{ref}.

$$V_{oid} = \frac{\partial V_p}{\partial p} - \left(\frac{\partial V_t}{\partial p}\right)_{T,\vec{N}} \tag{B.1}$$

Derivative of pore volume with respect to pressure

The pore volume is defined as the ratio of porous space to the total volume of the system (V_b). This is expressed as shown in Eq. B.2, where ϕ is the porosity.

$$V_p = \phi V_b \tag{B.2}$$

For a slightly compressible rock formation, we assume the following relation for variation of pore volume with respect to pressure, where V_p^{ref} is the pore volume at reference pressure and c_f is the constant rock compressibility.

$$\frac{dV_p}{dp} = V_p^{ref} c_f \tag{B.3}$$

Derivative of total volume with respect to pressure

The total fluid mixture (V_t) is a function of volumes of each phase: water (w), oil (o), and gas (g). n is the number of moles and v the molar volume of each phase.

$$V_t = n_w V_{m_w} + V_o + V_g \tag{B.4}$$

The derivative of total fluid V_t with respective to pressure can be expressed as:

$$\left(\frac{\partial V_t}{\partial p}\right)_{T,\vec{N}} = n_w \left(\frac{\partial V_{m_w}}{\partial p}\right)_{T,\vec{N}} + \left(\frac{\partial V_o}{\partial p}\right)_{T,\vec{N}} + \left(\frac{\partial V_g}{\partial p}\right)_{T,\vec{N}} \tag{B.5}$$

Derivative of water volume with respect to pressure

Assuming water as slightly compressible, we can approximate the water molar density as shown in Eq. B.7, where where $\rho_{m_w}^{ref}$ is the water molar volume at reference pressure p^{ref}, and c_w is the water compressibility.

$$\rho_{m_w} = \frac{\rho_{m_w}^{ref}}{1 + c_w(p - 2p^{ref})} \tag{B.6}$$

The derivative of water molar volume with respect to pressure, is then:

$$\frac{\partial v_w}{\partial p} = \frac{\partial(1/\rho_{m_w})}{\partial p} = -\frac{c_w(\rho_{m_w}^{ref} + 2p - p^{ref})}{\rho_{m_w}^2} \tag{B.7}$$

Derivative of hydrocarbon volume with respect to pressure

Appendix A described the derivative of pressure with respect to volume for the hydrocarbon phase. Therefore, we can express the derivative of hydrocarbon volume with respect to pressure as:

$$\left(\frac{\partial V_t}{\partial p}\right)_{T,\vec{N}} = \frac{1}{\left(\frac{\partial p}{\partial V_t}\right)_{T,\vec{N}}} \tag{B.8}$$

$$\left(\frac{\partial V_t}{\partial p}\right)_{T,\vec{N}} = \frac{1}{-\frac{RTn}{(V_t + nc - nb)^2} + \frac{2n^2a(V_t + nc + nb)}{[(V_t + nc)^2 + 2nb(V_t + nc) - n^2b^2]^2}} \tag{B.9}$$